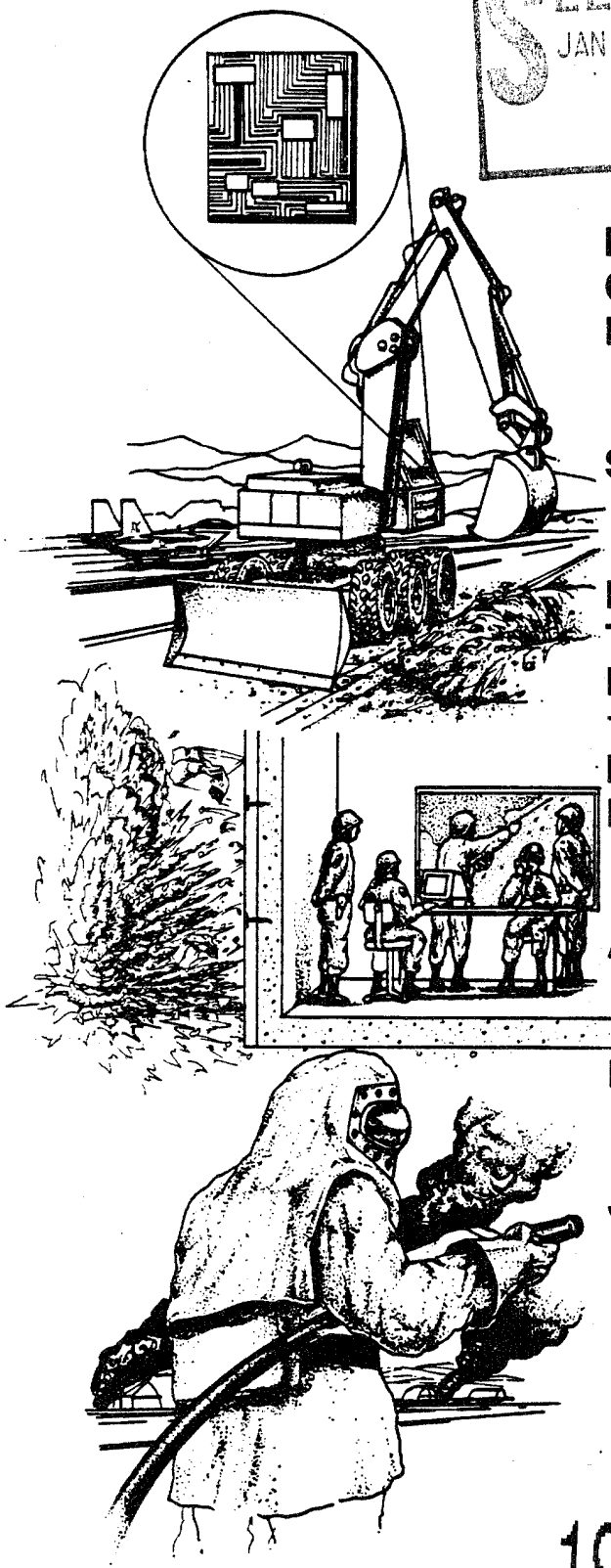

ESL-TR-91-45

MIXED-MODE FRACTURE OF CONCRETE AT HIGH STRAIN RATES

S.P. SHAH

NSF CENTER FOR SCIENCE AND TECHNOLOGY OF ADVANCED CEMENT-BASED MATERIALS (ACBM)
1800 RIDGE AVENUE
NORTHWESTERN UNIVERSITY
EVANSTON, ILLINOIS 60208-4400

APRIL 1995

FINAL REPORT

JANUARY 1989 - JULY 1991

**APPROVED FOR PUBLIC RELEASE:
DISTRIBUTION UNLIMITED**

ENGINEERING RESEARCH DIVISION
Air Force Civil Engineering Support Agency
Civil Engineering Laboratory
Tyndall Air Force Base, Florida 32403

NOTICE

PLEASE DO NOT REQUEST COPIES OF THIS REPORT FROM HQ AFCESA/RA (AIR FORCE CIVIL ENGINEERING SUPPORT AGENCY). ADDITIONAL COPIES MAY BE PURCHASED FROM:

NATIONAL TECHNICAL INFORMATION SERVICE
5285 PORT ROYAL ROAD
SPRINGFIELD, VIRGINIA 22161

FEDERAL GOVERNMENT AGENCIES AND THEIR CONTRACTORS REGISTERED WITH DEFENSE TECHNICAL INFORMATION CENTER SHOULD DIRECT REQUESTS FOR COPIES OF THIS REPORT TO:

DEFENSE TECHNICAL INFORMATION CENTER
CAMERON STATION
ALEXANDRIA, VIRGINIA 22314

REPORT DOCUMENTATION PAGE

Form Approved
OMB No. 0704-0188

1. AGENCY USE ONLY (Leave blank)	2. REPORT DATE	3. REPORT TYPE AND DATES COVERED
	April 1995	Final Report, JAN 89 - JUL 91

4. TITLE AND SUBTITLE

Mixed-Mode Fracture of Concrete at High Strain Rates

5. FUNDING NUMBERS

C F08635-89-C-0182

6. AUTHOR(S)

Surendra P. Shah

7. PERFORMING ORGANIZATION NAME(S) AND ADDRESS(ES)

NSF Center for Science and Technology of Advanced
Cement-Based Materials (ACBM)
1800 Ridge Avenue, Northwestern University
Evanston, Illinois 60208-4400

8. PERFORMING ORGANIZATION REPORT NUMBER

9. SPONSORING/MONITORING AGENCY NAME(S) AND ADDRESS(ES)

Department of the Air Force
Headquarters Air Force Civil Engineering Support Agency
Tyndall Air Force Base, Florida 32403-6001

10. SPONSORING/MONITORING AGENCY REPORT NUMBER

ESL-TR-91-45

11. SUPPLEMENTARY NOTES

12a. DISTRIBUTION/AVAILABILITY STATEMENT

Availability of this report is specified on reverse of front cover.

12b. DISTRIBUTION CODE

13. ABSTRACT *(Maximum 200 words)*

Mixed-mode fracture specimens were tested at quasi-static and impact rate of loading. Laser holographic interferometry, reflection photoelasticity, image processing and high speed photography were used for recording, measurement and analysis of data. Strain fields and crack growth were measured for center notched disk specimens. By rotating the notch angle with respect to the loading direction, it was possible to change the failure mode from mode I to mixed mode. Holographic observations were correlated with measurements obtained using reflection photoelasticity at quasi-static loading. Center notched disk specimens subjected to impact loading were studied with reflection photoelasticity and high speed photography (10,000 fps). The increase in fracture toughness at crack initiation for high rates of loading is affected by the failure mode. The increase in apparent fracture toughness for tensile cracking is approximately double the corresponding value for shear cracking. Failure of both quasi-static and impact rate of loading was characterized by crack initiation and stable crack growth. After initial crack growth, the crack continues to propagate in mode I regardless of the notch angle.

14. SUBJECT TERMS

Concrete Fracture Mechanics, Mixed-Mode Fracture, Strain Rate, Quasi-Static Loading, Impact Loading, Holographic Interferometry, Photoelasticity, High-Speed Photography, Digital Image Processing.

15. NUMBER OF PAGES

138

16. PRICE CODE

17. SECURITY CLASSIFICATION OF REPORT	18. SECURITY CLASSIFICATION OF THIS PAGE	19. SECURITY CLASSIFICATION OF ABSTRACT	20. LIMITATION OF ABSTRACT
Unclassified	Unclassified	Unclassified	

EXECUTIVE SUMMARY

MIXED MODE FRACTURE OF CONCRETE AT HIGH STRAIN RATE

Mixed-mode fracture specimens were tested at quasi-static and impact rate of loading. Laser holographic interferometry, reflection photoelasticity, image processing and high speed photography were used for recording, measurement and analysis of data.

Center notched plate specimens were loaded in tension. Two dimensional displacement fields were measured during stable crack propagation using holographic interferometry. Image processing was used to evaluate the fringe patterns. The existence of forces transmitted through the crack faces was associated with tensile strain behind the crack tip. The fracture process zone (FPZ) was defined based on the difference between measured and LEFM strain fields. A cohesive crack type model for Mode I fracture was used to predict experimental observations.

Holographic interferometry was generalized to measure three dimensional displacement fields. Strain fields and crack growth were measured for a diametral disk specimen (Brazilian Test). Tensile strain levels before cracking in the Brazilian configuration are significantly higher than those observed in the center notched plates. Crack initiation occurs at approximately 70% of the ultimate load. Cracks do not initiate in the region of uniform tensile stress as is commonly assumed in calculating tensile strength. Collapse of the specimen is due to the reported 'wedge' formation and occurs after a single crack has propagated through the specimen and a significant loss of strength has taken place.

Center notched disk specimens were tested under diametral loading. By rotating the notch angle with respect to the loading direction, it was possible to change the failure mode from mode I to mixed mode. The size of the FPZ defined as a function of the

tensile strain distribution depends on the fracture mode. The apparent stress intensity factor showed a R-curve type of behavior.

Holographic observations were correlated with measurements obtained using reflection photoelasticity at quasi-static loading for the center notched disk specimen. To study the influence of rate of loading, an instrumented Charpy type of test system was modified. Center notched disk specimens subjected to impact loading were studied with reflection photoelasticity and high speed photography (10,000 fps). The increase in fracture toughness at crack initiation for high rates of loading is affected by the failure mode. The increase in apparent fracture toughness for tensile cracking is approximately double the corresponding value for shear cracking. Failure of both quasi-static and impact rate of loading was characterized by crack initiation and stable crack growth. After initial crack growth, the crack continues to propagate in mode I regardless of the notch angle.

Reflection photoelasticity can be used to determine crack initiation and crack growth at both quasi-static and impact rate of loading. However it is not sensitive enough to provide information regarding the state of deformation away from the crack tip. Holographic interferometry with multiple sensitivity vectors and digital image analysis can provide a three dimensional displacement field with an accuracy of a 1/4 micron.

To design reinforced concrete structures subjected to impact loading, one must consider the observation that the influence of rate of loading is different for flexural failure and shear failure.

PREFACE

This final report was prepared by the NSF Center for Science and Technology of Advanced Cement-Based Materials (ACBM) at Northwestern University under contract No.F08635-89-C-0182 for the Department of the Air Force, Headquarters Air Force Civil Engineering Support Agency, Tyndall Air Force Base, Florida 32403-6001.

This report summarizes the results of experiments conducted to analyze mixed-mode fracture of concrete under quasi-static and impact rate of loading. The work was initiated in January 1989 and completed in July 1991. Professor Surendra P. Shah served as principal investigator at Northwestern University. Mr. Paul Sheppard served as Project Officer for HQ-AFCESA/RACS.

This report has been reviewed by the Public Affairs Office and is releasible to the National Information Service (NTIS). At NTIS it will be available to the general public, including foreign nationals.

This report has been reviewed and is approved for publication.

Paul E. Sheppard
Project Officer

Felix T. Uhlik III, Lt Col, USAF
Chief, Air Base Systems Branch

W. S. Strickland, GM-14
Chief
Air Base Survivability Section

(The reverse of this page is blank.)

TABLE OF CONTENTS

TABLE OF CONTENTS
(CONTINUED)

TABLE OF CONTENTS
(CONTINUED)

LIST OF FIGURES

TABLE OF FIGURE
(CONTINUED)

TABLE OF FIGURE (CONTINUED)

TABLE OF FIGURE
(CONTINUED)

TABLE OF FIGURE (CONTINUED)

TABLE OF FIGURE
(CONTINUED)

TABLE OF FIGURE (CONTINUED)

LIST OF TABLES

(The reverse of this page is blank.)

SECTION I

INTRODUCTION

A. OBJECTIVES

The purpose of the investigations reported in this document is to obtain fracture parameters for concrete subjected to mixed mode type loading at varying strain rates (10^{-6} to 1 per sec). Center-notched disk specimens (CNDS) were tested at slow rates in a closed-loop, servo-controlled test machine and at intermediate rate of loading (strain rate 1 to 10 per sec) in an instrumented Charpy machine. This investigation will be complemented by high rates of loading (strain rate $> 10^3$ per sec) obtained using a SHPB setup at the Air Force Engineering Service Center at the Tyndall Air Force Base (Figure Figure 1). The studies at slow rates were conducted to investigate the development of fracture process zone in Mode I and mixed mode using laser holographic interferometry. Additionally, laser holographic interferometry was used to calibrate reflection photoelasticity recordings on similar specimens at comparable rate of loading. The experimental techniques developed at slow rates were then extended to impact rates of loading. For impact loading, crack paths were traced by reflection photoelasticity.

B. BACKGROUND

Experimental results indicate that the tensile and compressive strengths of concrete increase with increase in rate of loading (References 1 and 2). There is an observed dependence between the failure mechanism and the rate of loading (Reference 3). A structure may fail in a ductile bending mode at slow rates of loadings and in shear at

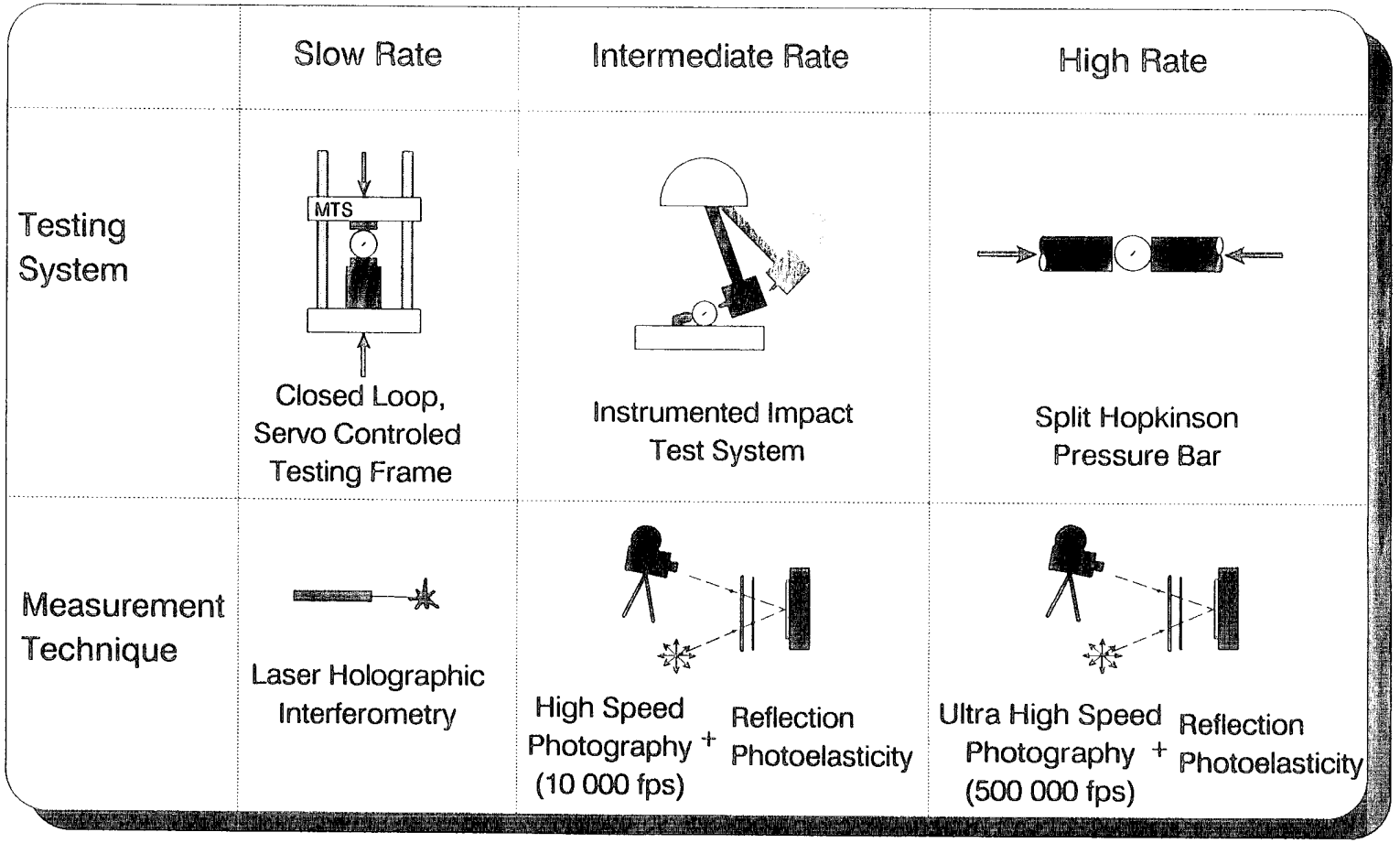

Figure 1 Strain Rate Effects on Mixed-Mode Fracture of Concrete. Project Summary.

higher rates of loading. To predict the rate dependent failure mechanisms in reinforced concrete structures, the knowledge of the effect of impact loading on fracture of concrete is essential. In the most general case, the fracture of concrete occurs under combined fracture modes. However, little information is available on the effects of rates of loading on fracture properties of concrete subjected to combined tensile and shear loading.

Recently, strain rate effects on compressive and tensile strength of concrete were conducted by Ross, et.al., Malvern, et. al. and Reinhardt, et. al. (References 4, 5 and 6) using Split Hopkinson Pressure Bar (SHPB) tests. Ross (Reference 4) used concrete cylinders loaded in uniaxial compression and in diametral compression (Brazilian Test) to study compression and tension at high strain rates. By introducing a central notch on the disk specimen, mixed mode fracture conditions can be obtained with a wide range of proportions between the tensile and shear components (Figure 2).

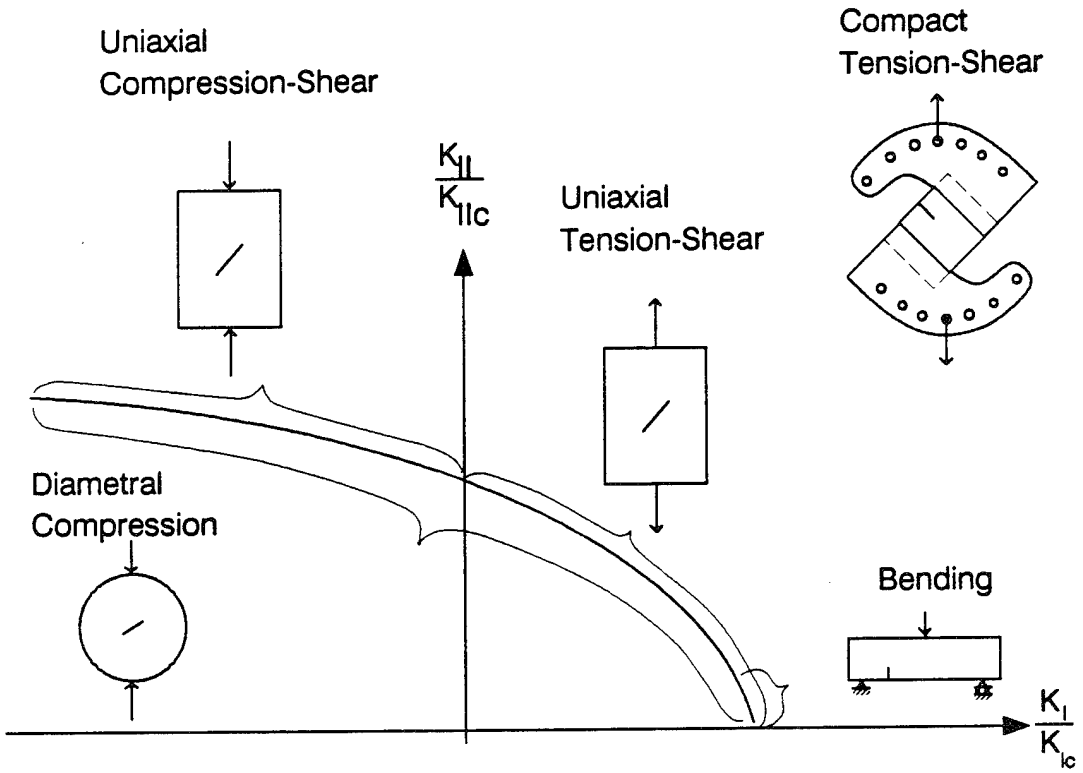

Figure 2 K_I/K_{IC} vs. K_{II}/K_{IIc} Curve for Different Load Configurations

C. SCOPE

Section II describes basic principles of laser holographic interferometry and image analysis and how they can be used to evaluate two-dimensional strain fields and how full filed displacement measurements can be used to characterize the fracture process. In Section III, an extrapolation of the techniques described in Section II for three dimensional displacement field evaluation under closed loop loading conditions are described. Using this techniques, crack initiation and propagation was evaluated in diametrically loaded cylinder specimens. Section IV presents the results of the strain field evaluation on CNDS at different notch inclination angles. Experimental observations were associated with the mode of fracture. In Section V photoelasticity recordings at slow rate of loading are compared with the holographic recordings at slow rates of loadings. An experimental arrangement for high-speed photoelasticity to be used for impact loading is presented and the results are compared with the slow rate of loading evaluations.

SECTION II

STRAIN FIELDS IN MODE I FRACTURE PROCESS ZONE

A. INTRODUCTION

The fracture of concrete is characterized by formation and propagation of fracture process zone. Several phenomena have been associated with fracture process zone including microcracking around the crack tip, localization and strain softening and crack bridging (often also termed aggregate interlock). A key to a better understanding of fracture mechanics of concrete is the accurate observation of fracture process zone on a microscopic scale. The research in this study has been directed to better understanding of the role of fracture process zone.

The first observation of this kind was made by Cedolin, Dei Poli and Iori (Reference 7). They used laser Moiré interferometry for wide field measurements in a specimen under tension. Such measurements allowed an indirect determination of the local stress-strain and stress-crack opening displacement (COD) relationships. White light Moiré interferometry was also used by Du, Kobayashi and Hawkins (Reference 8) to measure crack opening displacement along the fracture process zone (FPZ) for concrete specimens under three point bending. Regnault and Bruhwiler (Reference 9) used Moiré holographic interferometry to measure strain field on wedge-splitting test specimens and concluded that the model based on the exact knowledge of traction free crack tip location does not describe the material behavior in a realistic way. Raiss, Dougill and Newman

(Reference 10) also used laser Moiré interferometry to measure strain field on direct-tension specimens.

The accuracy of displacement observation with laser Moiré interferometry is limited by spacing of grating and possible debonding of grating. Miller, Shah and Bjelkhagen (Reference 11) used laser sandwich hologram interferometry to obtain crack opening displacements with an accuracy of 1/4 of a micrometer. With their technique it was not possible to measure wide-field two-dimensional displacement fields (only crack opening displacements were able to be measured) since the loaded specimen was illuminated by a laser beam from only one direction. In the technique described in this report, three simultaneous holograms were taken by illuminating the specimen from three different directions. In addition, digital image analysis techniques were developed to accurately evaluate wide field in plane deformation. The results of the strain field calculation obtained using this newly developed technique for mortar center-notched plate specimens are discussed in this investigation.

B. EXPERIMENTAL PROGRAM

Center-notched mortar plate specimens were used (Figure 3). One-inch (25 mm) diameter holes with 3/8 inches (9 mm) notches were cast into the center of 12 x 12 x 1 inches (305 x 305 x 25 mm) plates. The mortar used to cast the specimens had a cement/sand/water ratio by weight of 1.0/2.6/0.65. This specimen and loading type were selected because they provide a range of stable crack growth (i.e., K_I decreases as the crack length increases). This enables the making of holograms for several crack lengths without the use of a closed-loop system. This is important because the servo-control unit would introduce vibrations beyond the holographic limitations.

Three by six inch (76 x 152 mm) cylinders were also cast to determine the compressive strength and initial modulus of elasticity. Two cylinders with 1/2 inch (13 mm) strain gages were tested in a closed-loop testing system under strain control the day after the center-notched specimen test was performed.

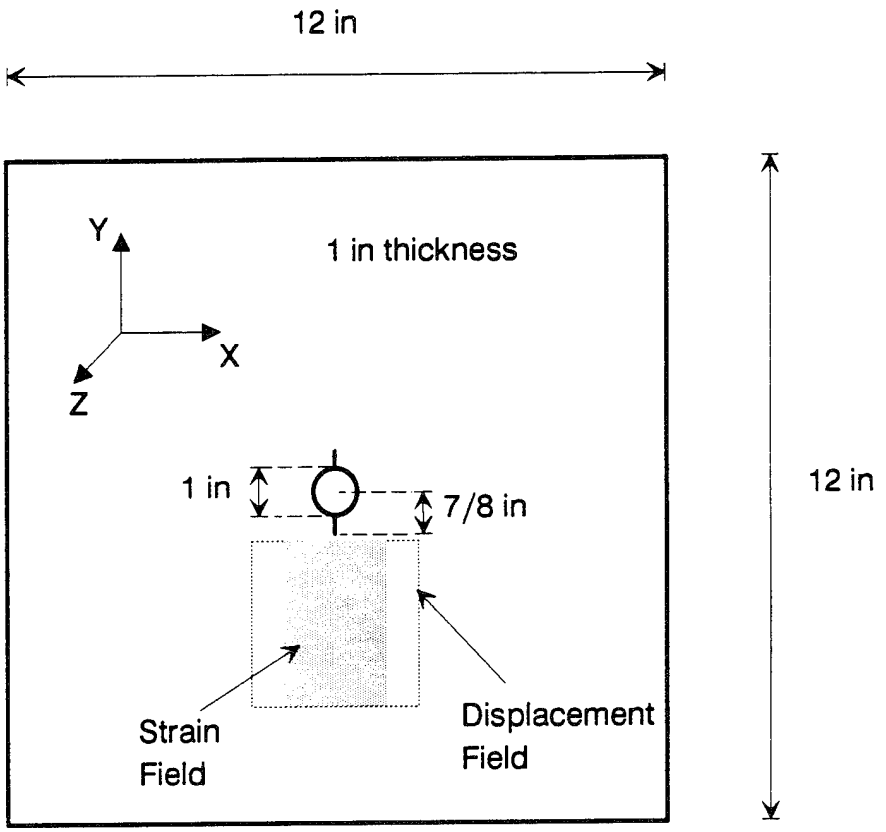

Figure 3 Center Notched Mortar Plate Specimen

The specimens were loaded in a 20-Kip (90 KN) screw-driven loading frame mounted on a vibration isolation table (Figure 4). Two semicylindrical pieces were attached to the loading pieces to apply the load on the one inch diameter loading hole. The specimens were loaded in parallel with four strain-gaged steel bars to provide extra stability to the crack growth.

Holographic interferometry was used to measure crack opening displacements and the strain field on a 2 inch x 3 inch (51 mm x 76 mm) area in front of each notch (that is, top and bottom; Figure 3). It is important to notice that during the experimental program, before any holograms were made, the specimens were placed under a 800 pound (3.6 KN) preload. This preload is necessary to keep the specimen optically stable.

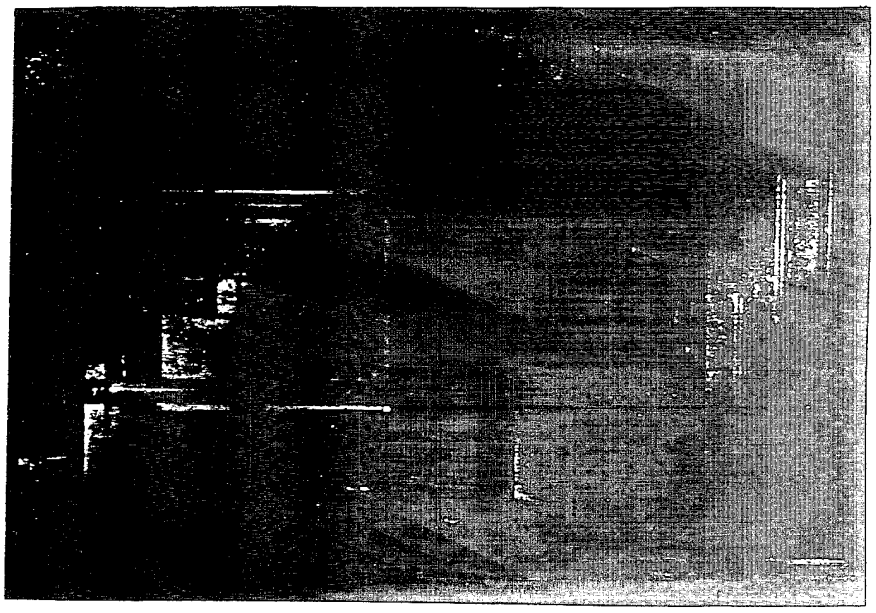

Figure 4 Loading Arrangement

C. HOLOGRAPHIC INTERFEROMETRY TEST

A hologram is a photographic recording that when illuminated by an appropriate reference light reproduces a three dimensional image of an object. If the same object is recorded in two different states of deformation, the combined reconstructed image is covered with dark and bright bands (interference fringes) that represent the displacements between the two states of deformation. Split-beam transmission holograms (Leith-Upatnieks type, Reference 12) were used. A 10 mW He-Ne laser with a wave length of 24.9 μin (633 nm; red) and coherence length (λ) of approximately 3 inches (76 mm) was used as the source of light.

Each interference pattern represents the component of the displacements onto the sensitivity vector k (Reference 13). In the optical setup shown in Figure 5 all the optical paths are on a plane of constant height (y=constant in Figure 3). Therefore, the sensitivity of the optical system to vertical displacements is small. In addition, the loading configuration shown in Figure 4 restrains displacements in the y direction. Thus, two displacement components are sufficient to describe the motion of any point on the

specimen, namely the in plane component (x) and the out of plane component (z). To obtain a two-dimensional displacement field (in plane and out of plane), in principle, two interferograms are required. However, since there is no sign associated to the fringe counts a third interferogram is necessary. These requirements are discussed in more detail in a subsequent section.

The sensitivity vector (**k**), defined as the bisector between the illumination and observation directions, can be changed by either moving the observation or the illumination point. Figure 5 is a schematic view of the optical setup with three illumination directions (R,L and C) used for this study.

For each load step, a different hologram is recorded from each illumination direction (holograms R,L and C). The holograms are developed and real-time interferometry is used to apply an adequate incremental displacement. One of the holograms is positioned on the plate holder and illuminated with the reference beam while the object is illuminated with the corresponding object beam (for example, R object beam for hologram R). When the observer looks at the object through the holographic plate the interference between the real object and the holographic image is viewed. Load is then applied to the specimen until the fringe pattern reaches the desired density (approximately 25 fringes across the specimen). A coarse fringe pattern would result in inaccurate displacement calculations as it will be explained later and a fine fringe pattern would make the fringe counting difficult since the fringe spacing would approach the resolution limit. A new set of holograms is then made on different photographic plates. When two holograms corresponding to the same illumination direction and consecutive load steps are mounted together on the plate holder and illuminated with the reference beam a holographic interferogram is reproduced. The above method is called sandwich hologram interferometry (Reference 14).

The incremental nature of the holographic measurements, make it necessary to make a series of sandwich holograms at continuous load levels. If a load increment is not recorded, none of the future deformation states can be computed.

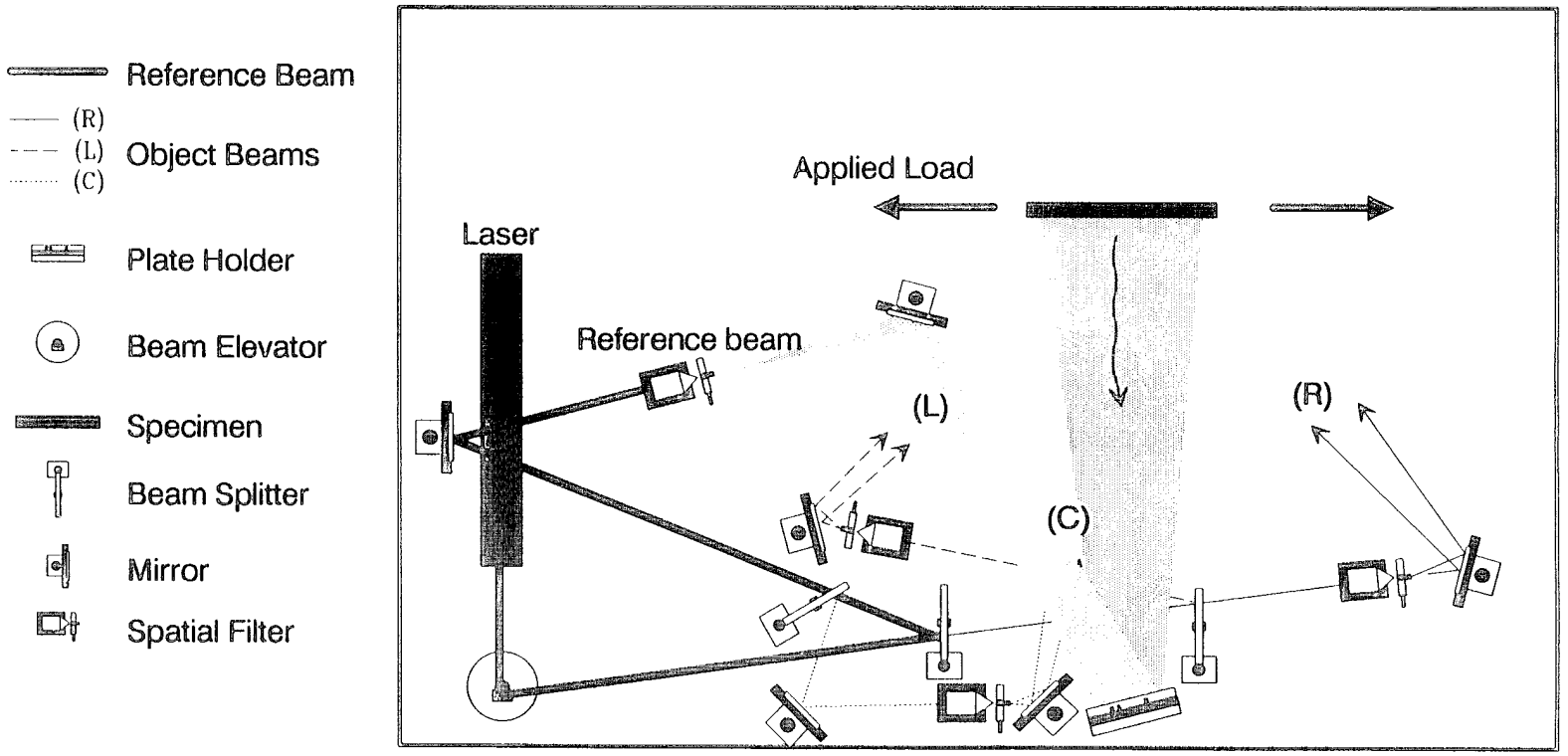

Figure 5 Holographic Arrangement

D. IMAGE PROCESSING

1. Image Enhancement

The holographic interferograms were acquired into an image analysis system using a slow-scan high-resolution camera. A schematic arrangement for reconstruction of the holographic images and acquisition into the image analysis system is shown in Figure 6. The acquired image (grey image) contains a range of intensities (0-255) representing different grey levels. The image is represented by a 512x512 2-d array of integers, each corresponding to the average light intensity across an element area referred to as pixel (Picture Element). The size of a pixel determines the spatial resolution.

The bright and dark bands of the holographic fringes can be represented as a binary image. In a binary image the pixel intensities assume only two values, ON (or 1) for perfect white and OFF (or 0) for perfect black. Variations of intensity of the object beam throughout the surface of the object, make possible that a bright band at a section of the image will have a lower intensity magnitude than the dark bands at other segments of the image. Standard methods of image processing such as thresholding from a certain pixel intensity are thus inapplicable. This situation is represented by the plot in Figure 7a which shows the intensity variations along a cross section of a holographic grey image.

If I_1 and I_2 are the intensities of the individual images in a sandwich hologram, the intensity of the resulting interference pattern is:

$$I = (I_1 + I_2) + 2 (I_1 I_2)^{1/2} \cos \Delta\phi \qquad (1)$$

From this equation it is apparent that the intensity value of any pixel can be separated into two terms. One is the average intensity of the image ($I_1 + I_2$), and the second depends on the phase difference ($\Delta\phi$) between the two wave fronts. The separation of this two terms can be achieved through the use of the image analysis system.

Assume that the grey image of the sandwich holography interferogram is represented as IMAGE_1 where as IMAGE_2 is the average of the independent wave fronts acquired separately (Figure. 7a). Subtraction of IMAGE_2 from IMAGE_1 results

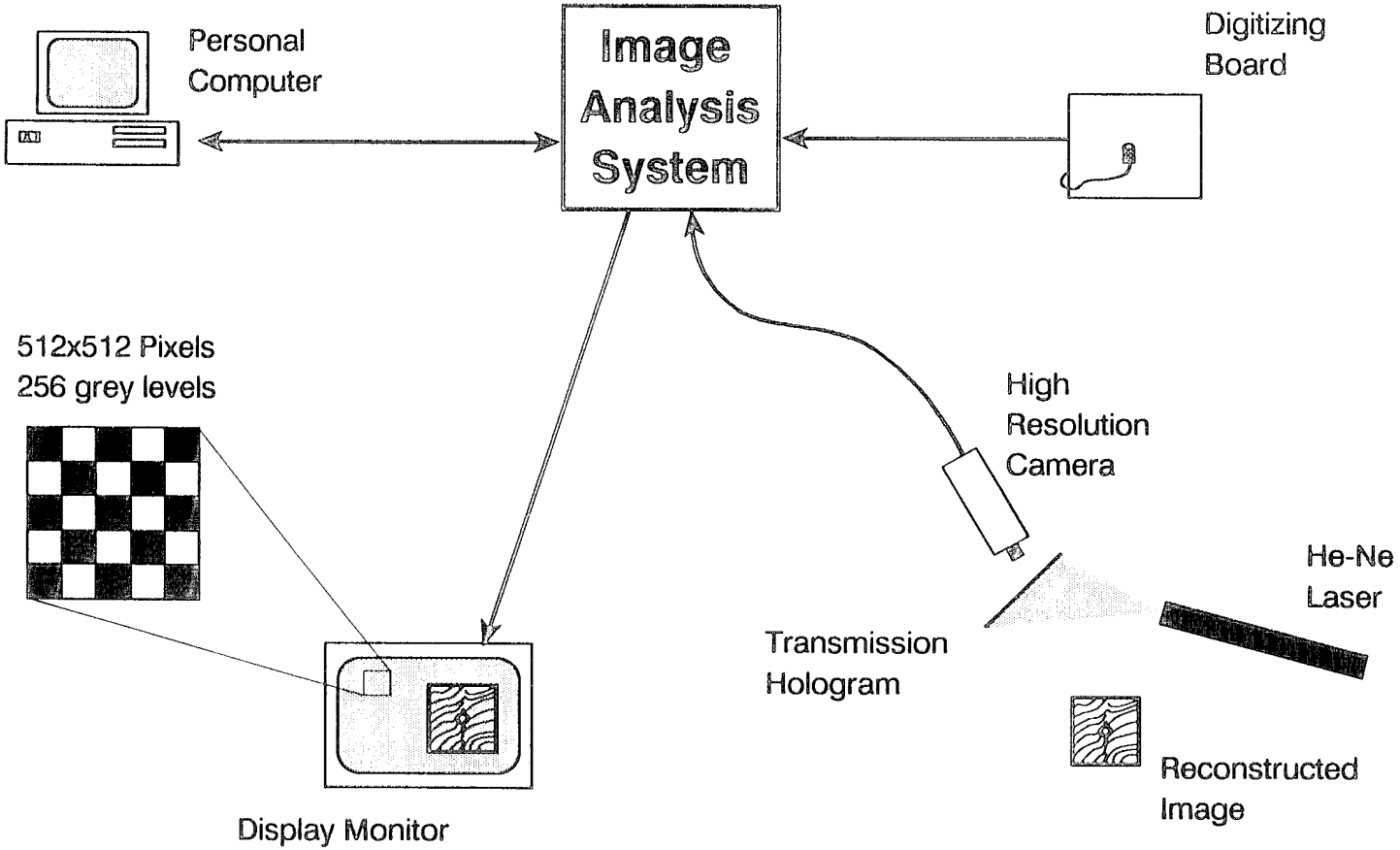

Figure 6 Image Reconstruction and Acquisition Arrangement

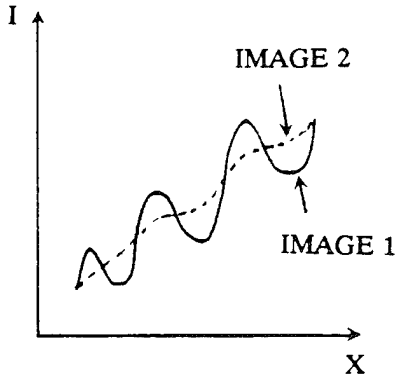

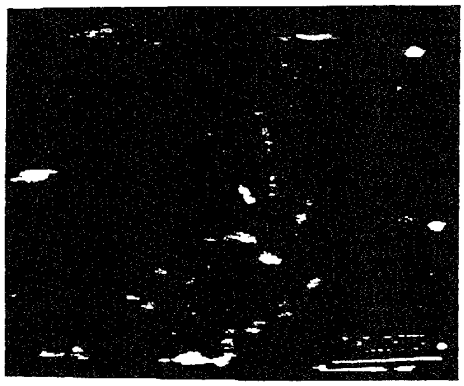

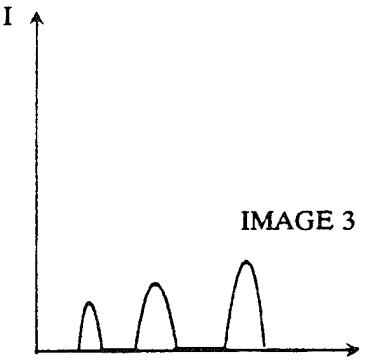

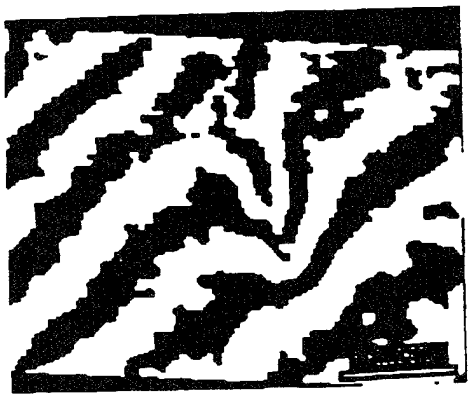

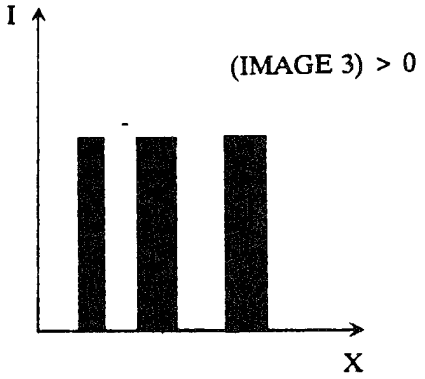

Figure 7 Image Enhancement
a) Intensity Distribution Across Interferogram
b) Isolation of Interferometric Effect
c) Binary Image

in the isolation of the interferometric effect, represented as IMAGE_3 in Figure 7b. Since negative values are not allowed as meaningful intensity values, IMAGE_3 results in zero for all the pixels on dark bands. The bright bands retain a positive magnitude. By selecting all positive values a binary image is created (Figure 7c).

2. Fringe Count

IMAGE_3 is the enhanced interferometric image in which the intensity value is zero for dark bands and one for bright bands. Further image processing allows to assign intensity values to each fringe corresponding to the fringe order.

A pixel P is selected on the binary image (IMAGE_3). A flooding procedure which assigns an arbitrarily selected intensity value (Y) to all the pixels connected to Pixel P is performed. Thus, all the pixels on the band containing P are assigned the intensity value Y. The same procedure is repeated for consecutive bands. The intensity value Y is incremented by one for each band.

Even though this process has been greatly automated, user interaction is necessary for the definition of the fringe count direction. In Figure 7c line A-B indicates the direction of positive fringe count (e.g., the fringe order, or intensity value, increases from A to B). The above flooding process is repeated until the whole area of interest has been included. In Figure 8 flooding trajectories A-B, C-D and E-F have to be followed.

Figure 8 shows a fully processed interferogram in which same intensity values correspond to same fringe orders. Note that there is a different intensity level for each half a fringe (that is, different intensity for dark and bright bands). The fringe count between any two points can now be easily obtained by computing half the difference of the corresponding intensity levels (e.g., fringe count between A and B in Figure 8 is (90 - 65)/2 = 12.5). For further refinement on the fringe count, the fringe order of the point A in Figure 8 is computed according to Equation (2) (see inset of Figure 8).

$$Y = \frac{(Y_0 + Y_{-1})}{2} + \frac{(Y_1 - Y_2)\,NP_0}{2\,NP} \qquad (2)$$

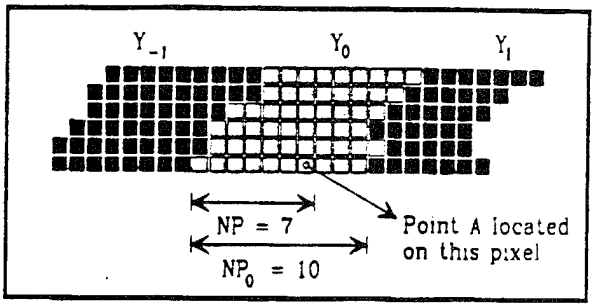

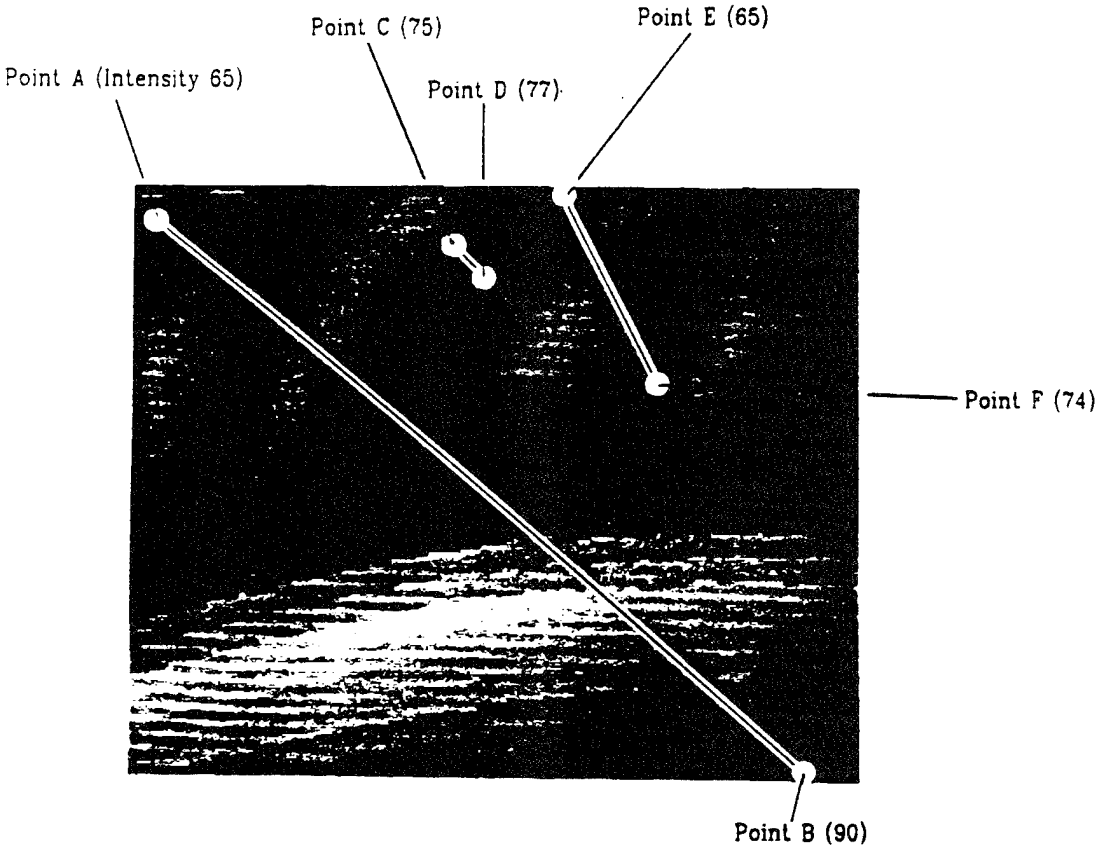

Figure 8 Fringe Count by Difference in Intensity Value

where:

NP_0	total number of pixels across the band containing point A
NP	number of pixels from beginning of band to point A
Y_0	intensity value of the band containing point A
Y_{-1}	intensity value of preceding band
Y_1	intensity value of subsequent band

Even though the use of the image analysis system results in very fast fringe counts, speed is not the main advantage of this technique. The isolation of the interferometric effect on the holographic images and the binarization process result in accurate and objective fringe counts. The gradual change in intensity from a dark to a bright band make it difficult to obtain consistent fringe counts when conventional (by hand) methods are used.

E. EVALUATION OF HOLOGRAMS

The holodiagram (Reference 15) shown in Figure 9a is a simple geometrical tool for computation of displacements based on interferometric readings. In Figure 9a the distance I-P-O from illumination point to object to observation point (usually taken as the position of the holographic plate) remains constant if the object (P) moves along ellipse E_1 (or an ellipsoid in the most general three dimensional case) with foci at illumination and observation points. Now, define ellipse E_2 such that the distance I-P-O increases by $\lambda/2$ (180° phase difference). An interferogram of the object that moved from any point on ellipse E_1 to any point on ellipse E_2 will show a dark band (half a fringe) due to destructive interference of the wave fronts. In general, the number of fringes is proportional to the increase (or decrease) of the distance I-P-O (Equation (3)).

$$\Delta\ (\ I\text{-}P\text{-}O\ ) = n\ \lambda \qquad (3)$$

where:

Δ (I-P-O)	increment of distance I-P-O
n	fringe count (one fringe = one dark band and one bright band)

Figure 9a shows an infinite number of possible displacement vectors which result on the same fringe count.

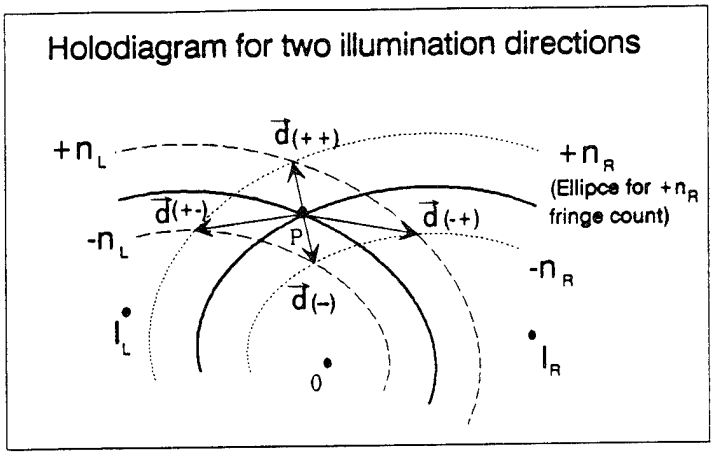

E_1 Ellipce for constant I-P-O
E_2^+ Ellipce for +1/2 fringe (Δ-P-O = $+\lambda/2$)
E_2^- Ellipce for -1/2 fringe (Δ-P-O = $-\lambda/2$)
I Illumination Point
O Observation Point
P Point on the Object

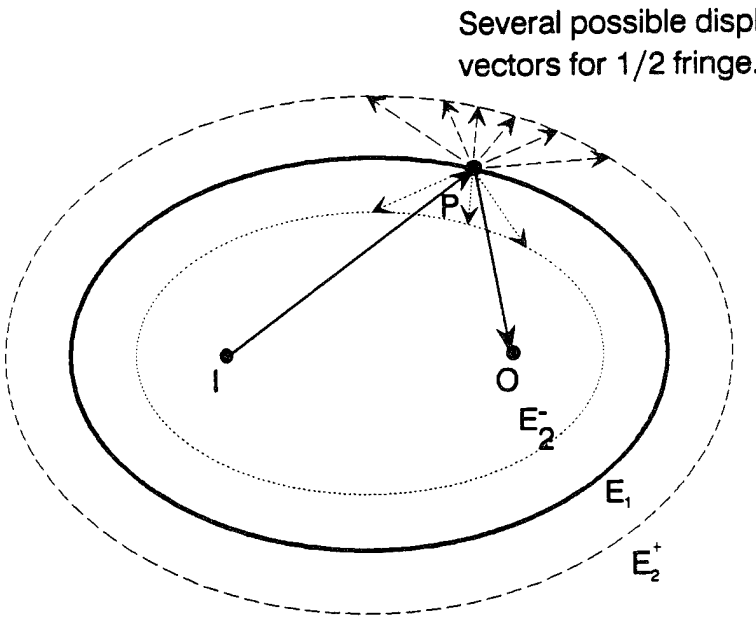

Figure 9 Evaluation of Interferograms
a) Holodiagram
b) Displacement Vector as the Intersection of Two Holodiagrams

Figure 9b shows how the number of possible displacement vectors is reduced to four by using two holograms with different illumination points and fringe counts n_1 and n_2. Using a fringe count from a third hologram, it can be determined if n_1 and n_2 have the same or opposite sign, but it cannot be determined if they are positive or negative. Because of the uncertainty on the sign of the fringe counts, at least two solutions are mathematically possible, one being the negative of the other. However, the distinction can be made by selecting the signs which result in "expected" displacements (for example, for the specimen under tensile load the crack should open).

1. Crack Profiles.

For the computation of the crack opening displacements (COD) the modified Nelson and McCrickerd (References 16 and 11) method was used. This method assumes the out of plane motion to be negligible (that is, COD is the main component of the displacement) and that displacements are small. Since the direction of motion is assumed, one hologram is sufficient. Equation (4) gives the magnitude of the COD in terms the fringe count and the geometry of the optical set-up.

$$COD = \frac{n\,\lambda}{4\,\cos\alpha\,\cos\psi} \qquad (4)$$

where:

COD	Crack Opening Displacement. Displacement of one point on the crack face with respect to the point across the crack.
n	fringe count from a point on the crack face to the point across the cross the crack.
α	angle between illumination direction and sensitivity vector (k)
ψ	angle between direction of motion and sensitivity vector (k)

If the fringe counts are accurate within 1/4 of a fringe, the accuracy in displacement computation is improved for large angles α and ψ. For this reason, only holograms R and L were considered. Also, note that large fringe counts are more accurate percentage wise (for example, 10 ± 1/4 is more accurate than 1 ± 1/4).

Note that in the above formulation (and all holographic interferometry methods), the COD should be taken as an incremental value. The total COD at a given load level

is the cumulative of the CODs for all the previous load levels. Two typical crack profiles included in Figure 10 show that there is a good match in the crack profiles obtained with both holograms.

An alternative solution is to assume a two dimensional displacement solution. The displacement is computed as the difference in position of the intersection of the ellipses from two illumination directions (Figure 9b). The holographic fringe counts can be combined in three possible ways (R and L, R and C, C and L). As mentioned before, the third fringe count is necessary to select the correct value among the four possible displacement solutions for each combination. Figure 10 shows a crack profile computed using all three combinations. There is an improvement in the scatter on the COD calculations with respect to the Nelson and McCrickerd results. Also, note that considering the out of plane contribution to the fringe counts results in smaller CODs, even for an experimental setup designed for Mode I crack propagation. This means that there exists a measurable component of the crack face displacement exists in the out-of-plane direction (Mode III) which can explain the presence of compressive strain behind the crack tip as reported by Bruhwiler. The dotted line in Figure 10 represents the crack sliding displacement (CSD) in the XZ plane.

2. Strain Fields.

Fringe counts relative to the left face of the crack, or the symmetry line for point beyond the crack tip, were taken at every point on a 3 inch x 3 inch (76 mm x 76 mm) grid (1.5 inches on each side of the crack line and 3 inches in front of the notch tip) every 1/8 inches (3 mm) for all three holographic images (R,L and C). A computer program was used to calculate the relative displacement of every point relative to the left face of the crack by locating the intersection point of the holodiagrams corresponding to each illumination direction. A third-order best-fit polynomial was obtained for the displacements along lines perpendicular to the crack line. For the sections crossing the crack a different polynomial was obtained for the left and right side of the crack. The strain field was obtained by differentiation and was evaluated from $x=-1$ in to $x=+1$ in every 1/8 in (3 mm) at every cross section, where x is the distance from the crack line

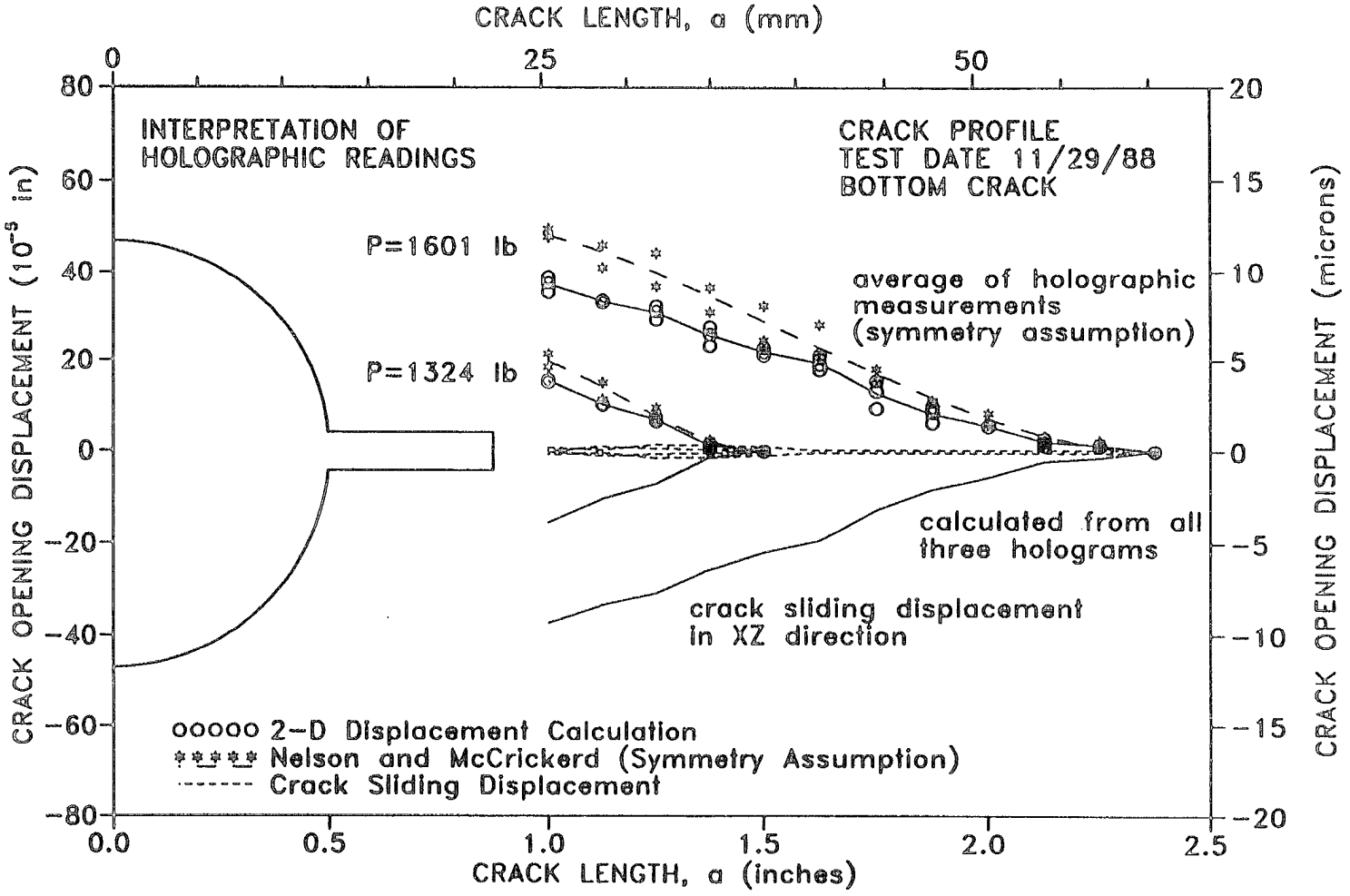

Figure 10 Holographically Measured Crack Profiles

and is positive to the right. For the sake of brevity, results for one of the cracks on one of the specimens are shown. These results can be considered representative of the six cracks examined. Figure 11 shows the strain field (ϵ_{xx}) around the bottom crack for crack lengths of 1.375 in (35 mm), 1.875 in (48 mm) and 2.25 in (57 mm), corresponding to 1324 lb (6.0 KN), 1461 lb (6.6 KN) and 1601 lb (7.2 KN) of applied load. The strain fields shown in Figure 11 include only the measured additional strain after the initial preload state.

In general, a high strain ($>100\mu\epsilon$) region can be found around and in front of the crack tip with a maximum value of approximately 300 $\mu\epsilon$. Behind the crack tip there is a zone of negative strain which suggests relaxation of tensile strain with respect to the initial preload stage.

Figure 12 shows the strain distribution along sections parallel to the crack line for various load levels. In this Figure, a linear elastic component corresponding to the initial preload has been added in an attempt to provide a better picture of the total state of strain. Similar observations as those made by Cedolin, Dei Poli and Iori (Reference 7) can be made. Figure 12 shows that the material on both sides of the crack unloads. The strain concentrations near the crack tip and the unloading are greater on sections closer to the crack line. Although there is unloading behind the crack tip, the strain level does not immediately reach zero; this suggests the existence of tension being transmitted through the crack.

F. DEFINITION OF THE FRACTURE PROCESS ZONE

Cedolin, et al. (Reference 7) suggested the use of isostrain contours to enclose zones of microcracking and he referred that zone as Fracture Process Zone (FPZ). He assumed that the region where the strain value exceeded 150 $\mu\epsilon$ was FPZ. In this study it was assumed that the strain value of 100 $\mu\epsilon$ is a more reasonable limit to define nonlinearity. The zone where the measured strain values exceed 100 $\mu\epsilon$ are shown in Figure 13 for three crack lengths. Also shown in the Figure, the shaded areas are the zones behind the crack tip where tensile strain was detected. The end of these zones

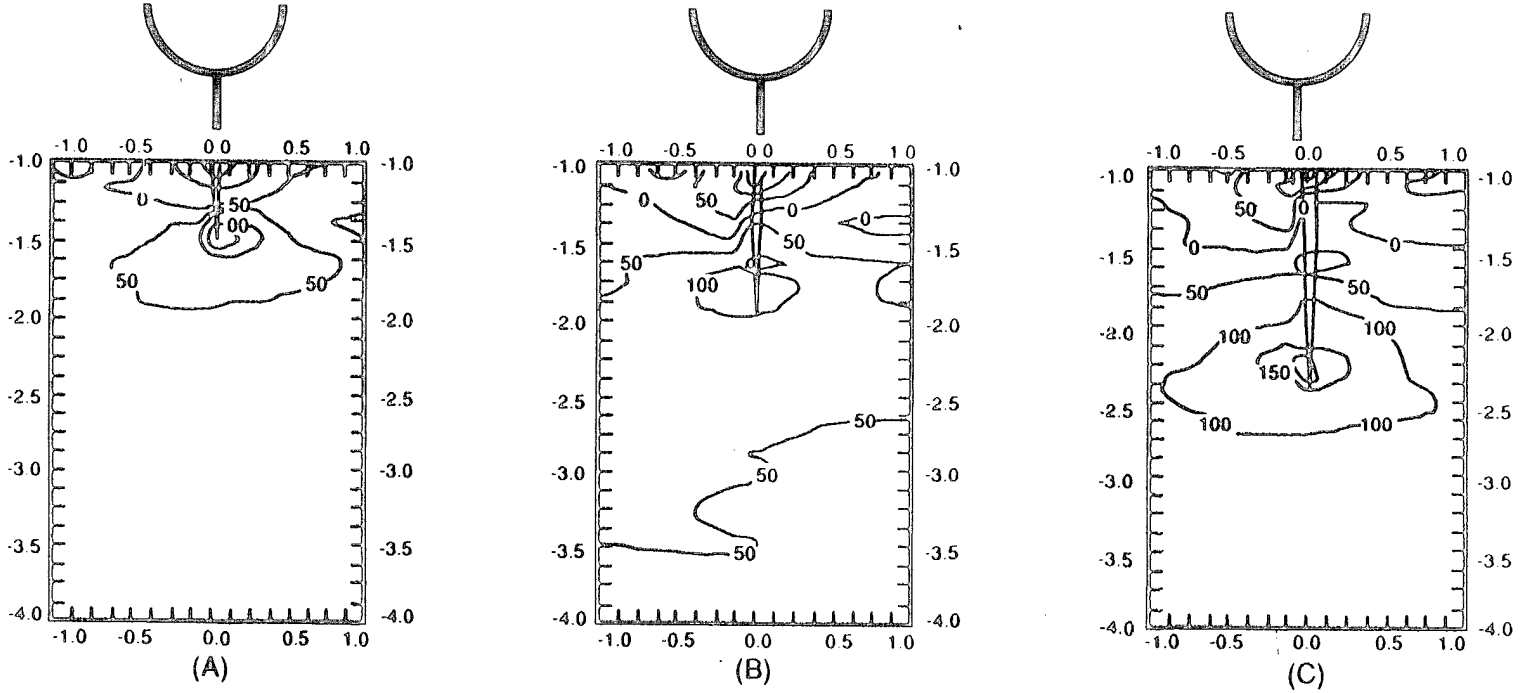

Figure 11 Holographically Measured Strain Fields ($\mu\epsilon$)
(a) Load = 1324 lb. (b) Load = 1461 lb. (c) Load = 1601 lb.

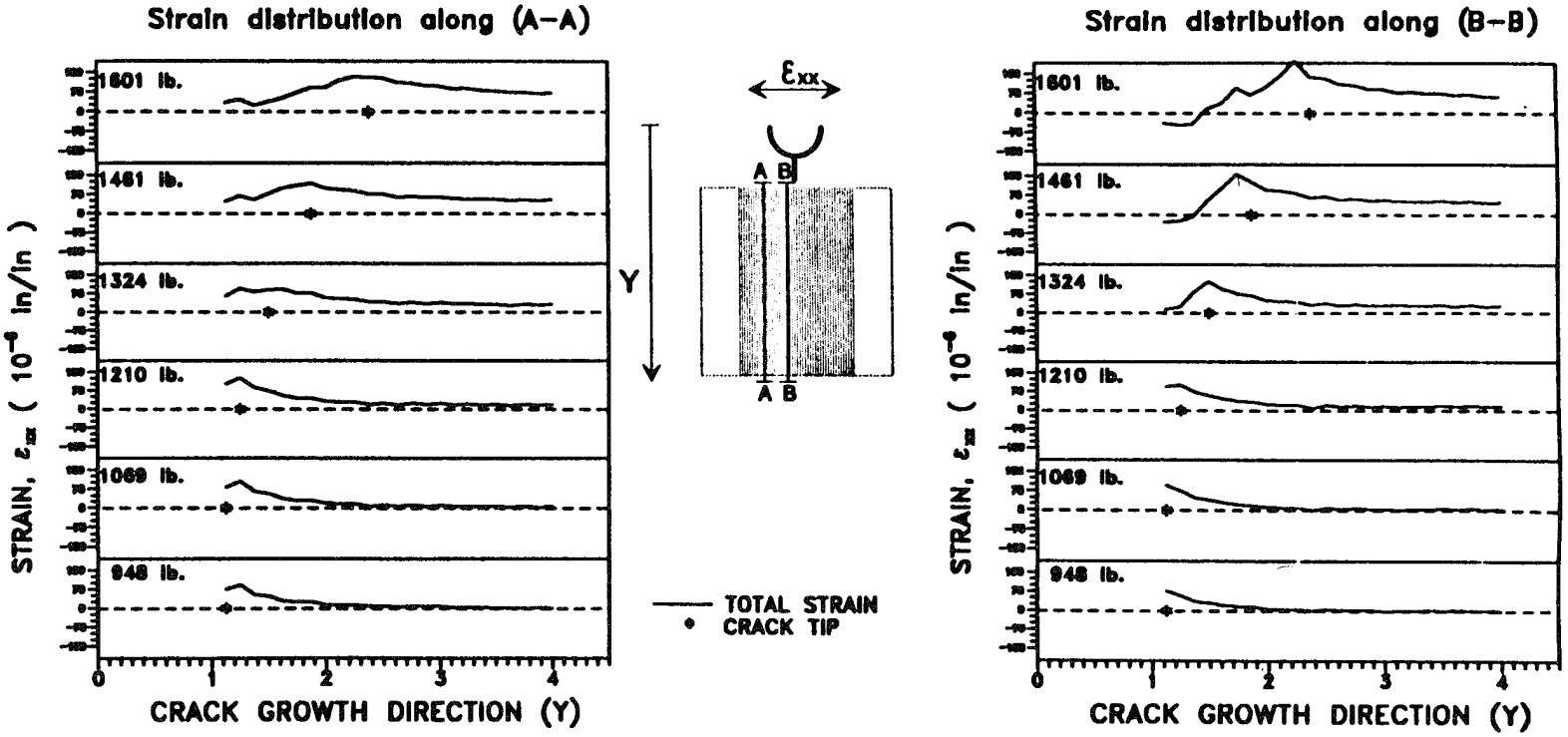

Figure 12 Strain Distribution Along Section Parallel to the Crack Line

correspond to the tensile strain value of zero (see Figure 11). There appears to be a traction free zone of approximately 0.25 inch in front of the original notch tip regardless of the crack length and COD indicated by w_c in Figure 13). This agrees with the model suggested by Cook, et al. (Reference 7) where it is postulated that cohesive forces are activated by disperse particle or ligaments. Unless the crack length is larger than the spacing of the ligaments there is no closing pressure for this initial zone of crack growth.

If isostrain value is used to define FPZ it can be seen that this zone increases with crack length. An alternate approach to define the FPZ is to find the deviations from the linear elastic solution. The specimen was analyzed using a finite-element program. Quarter point triangular elements were used to model the singularity at the crack tip. The analysis was carried out for the initial preload state and every subsequent load level. In order to make a valid comparison with the experimental results, Figure 14 shows the linear elastic fracture mechanics (LEFM) strain distribution corresponding to the difference between the given load level and the initial preload. Note that the strain levels surrounding the crack tip exceed those from the holographic measurements (Figures 11 and 12)

Behind the crack tip the LEFM solution shows sharp unloading. At 1601 lb the strain drops from 500 $\mu\epsilon$ at the crack tip to zero within 1/8 in behind the crack tip. In contrast, the observed strain relaxation shown on Figures 11 and 12 follows a gradual descent.

In Figure 15, the differences in strain fields between the LEFM solution and the experimentally measured values are shown. It is arbitrarily assumed that the differences are significant when they exceed the strain value of 60 $\mu\epsilon$. Positive differences mean that the tensile strain predicted by LEFM was higher while the negative values mean that the LEFM predicted lower tensile strain than the holographically measured values. The zones marked A in Figure 15 are the regions where the LEFM solution predicts tensile strain values of 60 $\mu\epsilon$ or more higher than those measured holographically. Note that Zone A remains essentially constant regardless of crack length. Since this zone is relatively small and does not change with crack length a model based on modified LEFM may be a possible approach. This is discussed in the next section. Zone B, with negative values,

$\omega_o = 20 \times 10^{-5}$ in

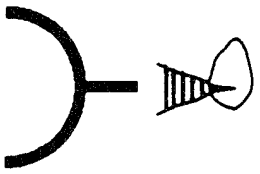

(a) Load = 1324 lb

$\omega_o = 34 \times 10^{-5}$ in

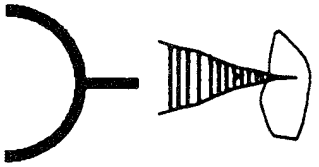

(b) Load = 1461 lb

$\omega_o = 62 \times 10^{-5}$ in

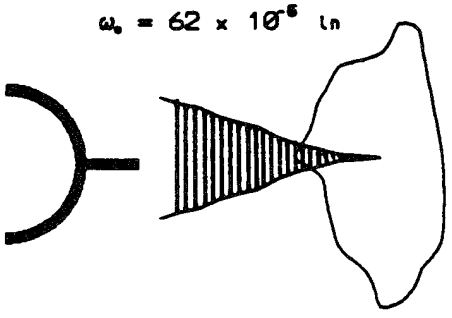

Figure 13 Fracture Process Zone

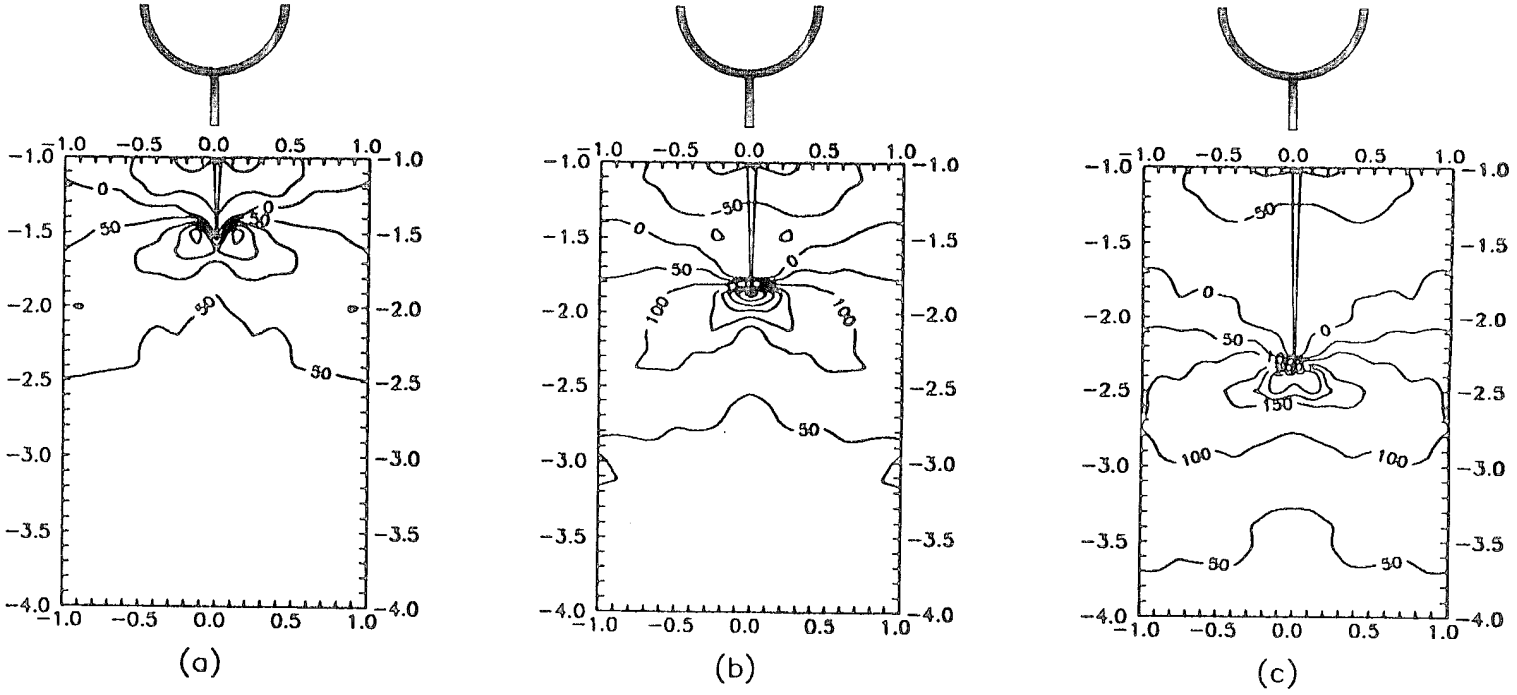

Figure 14 LEFM Strain Fields ($\mu\epsilon$)
(a) Load = 1324 lb. (b) Load = 1461 lb. (c) Load = 1601 lb.

typically found behind the crack tip, shows that the relaxation of the observed strain is 60 $\mu\epsilon$ less than that in the elastic solution. Zone B can be defined as the wake of the fracture process zone (WFPZ) and encloses the area where extensive microcracking has been developed and tensile forces are still transmitted through the crack. Behind this zone, the fracture process approaches a traction-free condition. Similar conclusions regarding the growth and propagation of the FPZ were reached analytically by Bazant and Gettu (Reference 17) if the crack tip is assumed behind the WFPZ.

G. CLOSING PRESSURE ANALYSIS

A cohesive type of model has been used to simulate effect of fracture process zone. A closing pressure is applied to the faces of the crack and it is assumed that the closing pressure is a function only of crack opening displacement. To determine if such a model can accurately predict the measured strain field, the same finite-element program with singular elements was used. A bilinear closing pressure vs. COD relationship was used. This relationship was shown by Miller (Reference 18) to reasonably accurately predict the holographically measured crack profiles for similar specimens made with identical mortar mix proportions. In general, an iteration procedure is necessary to perform the analysis based on a closing pressure vs. COD relation. However, since the CODs are expected to converge close to the holographically obtained values, these can be used to compute the closing pressure. Thus, the iteration process is not necessary.

Figure 16 shows a comparison of the holographically observed crack profiles, the LEFM solution and the predicted crack profiles using the bilinear closing pressure. The predicted crack profiles in Figure 16 show a good correlation with the experimental values.

Figure 17 shows the difference between the strain field predicted using the closing pressure approach and the experimentally observed values. There is a good correlation of the results and the zones with significant deviation from the experimental results are practically eliminated ($\pm$ 60 $\mu\epsilon$). Figure 18 reports the computed values of the resultant

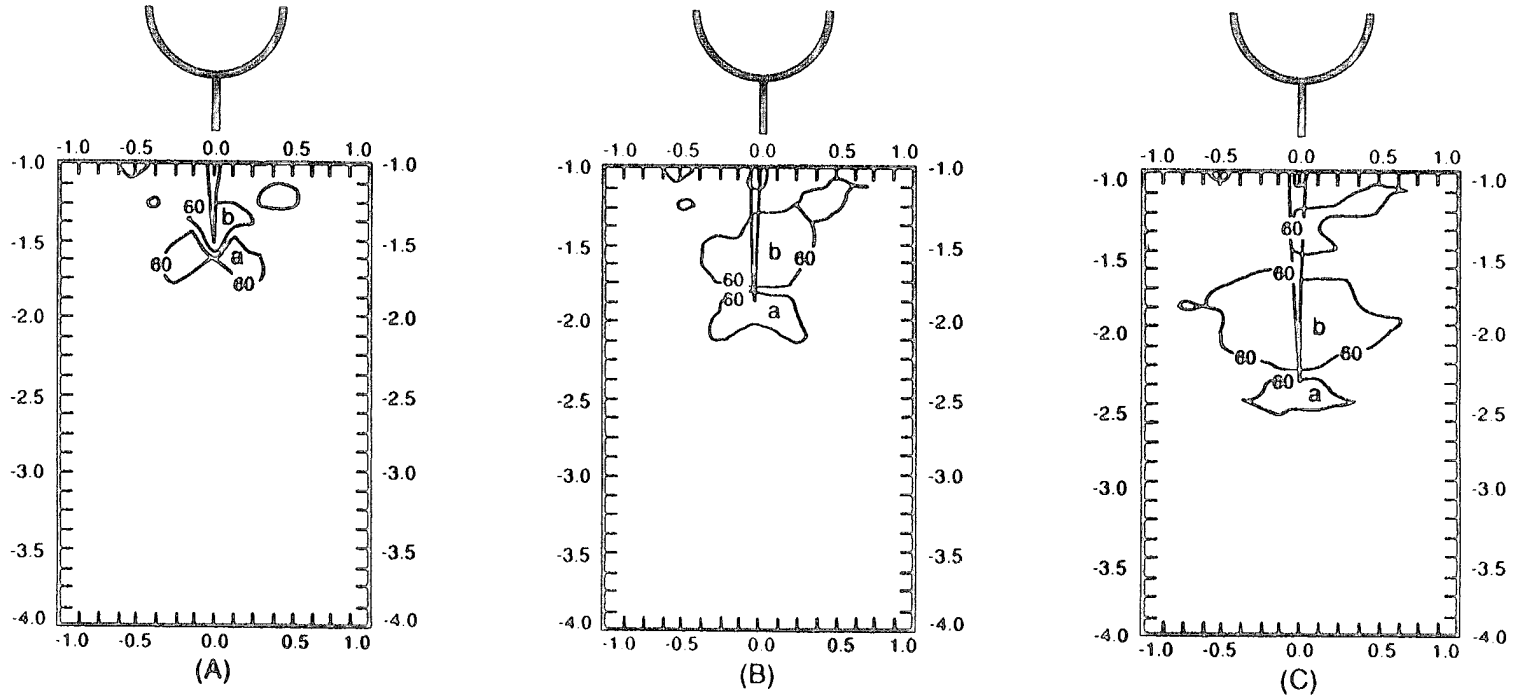

Figure 15 Difference Between Holographic and LEFM Strain Fields ($\mu\epsilon$)
(a) Load = 1324 lb. (b) Load = 1461 lb. (c) Load = 1601 lb.

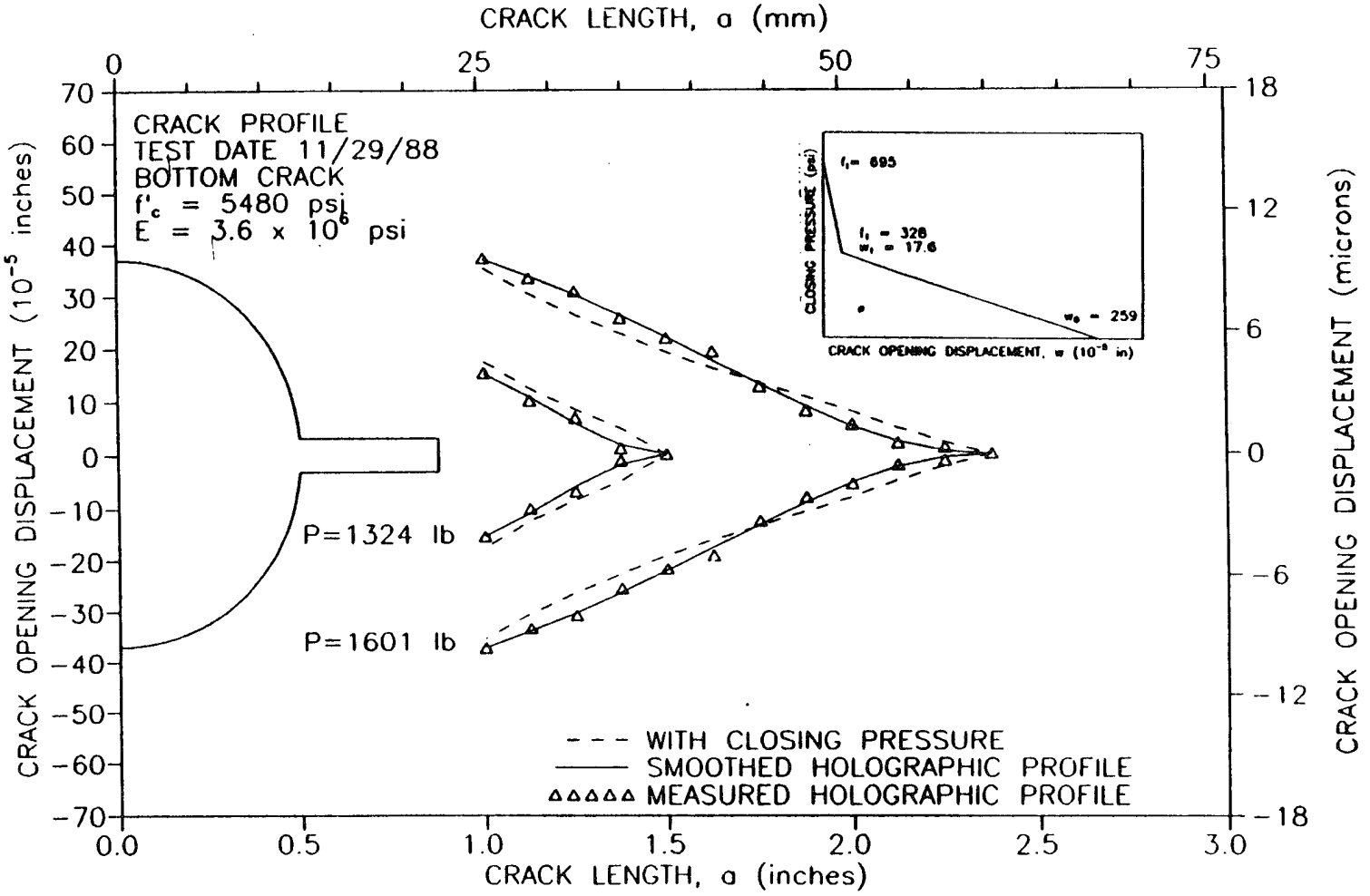

Figure 16 Comparison Between Holographically Obtained and Computed Crack Profiles

stress intensity factors. These values are due to the combined effects of the applied load and the closing pressure. These resultant stress intensity factors are essentially constant through the crack growth. Thus, a constant $K_I = K_{Ic}$ type of criteria can be used to predict crack growth.

H. CONCLUSIONS

1. Sandwich hologram interferometry with multiple sensitivity vectors can be used to measure crack opening displacements and strain fields in mortar specimens under tensile stress. When holographic interferometry is used to measure Mode I crack opening displacements the effect of out of plane motion should be taken into account.
2. Digital image analysis facility provided a faster, more consistent and more accurate method of fringe count than the manual method.
3. There is a region of high tensile strain that moves with the tip of the propagating crack. The material behind the crack tip experiences strain relaxation. However, the gradual nature of the strain relaxation demonstrates the existence of tensile force transmitted through the crack faces.
4. Zones of nonlinear behavior can be located by computing strain field deviations form the linear elastic solution.
5. A bilinear closing pressure vs. COD cohesive crack model has been proposed to predict both crack profiles and strain field, fully characterizing the material behavior.

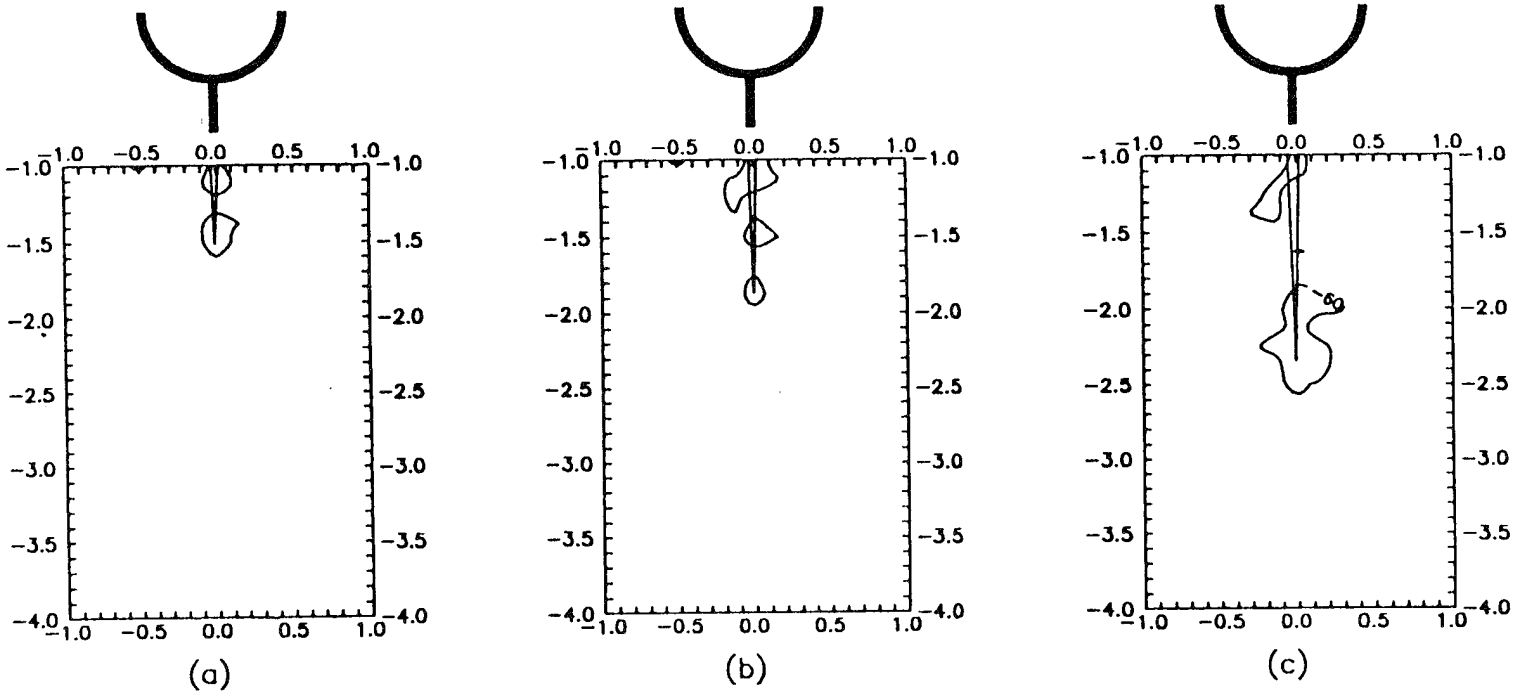

Figure 17 Difference Between Holographic and Bilinear Closing Pressure Strain Fields ($\mu\epsilon$)
(a) Load = 1324 lb. (b) Load = 1461 lb. (c) Load = 1601 lb.

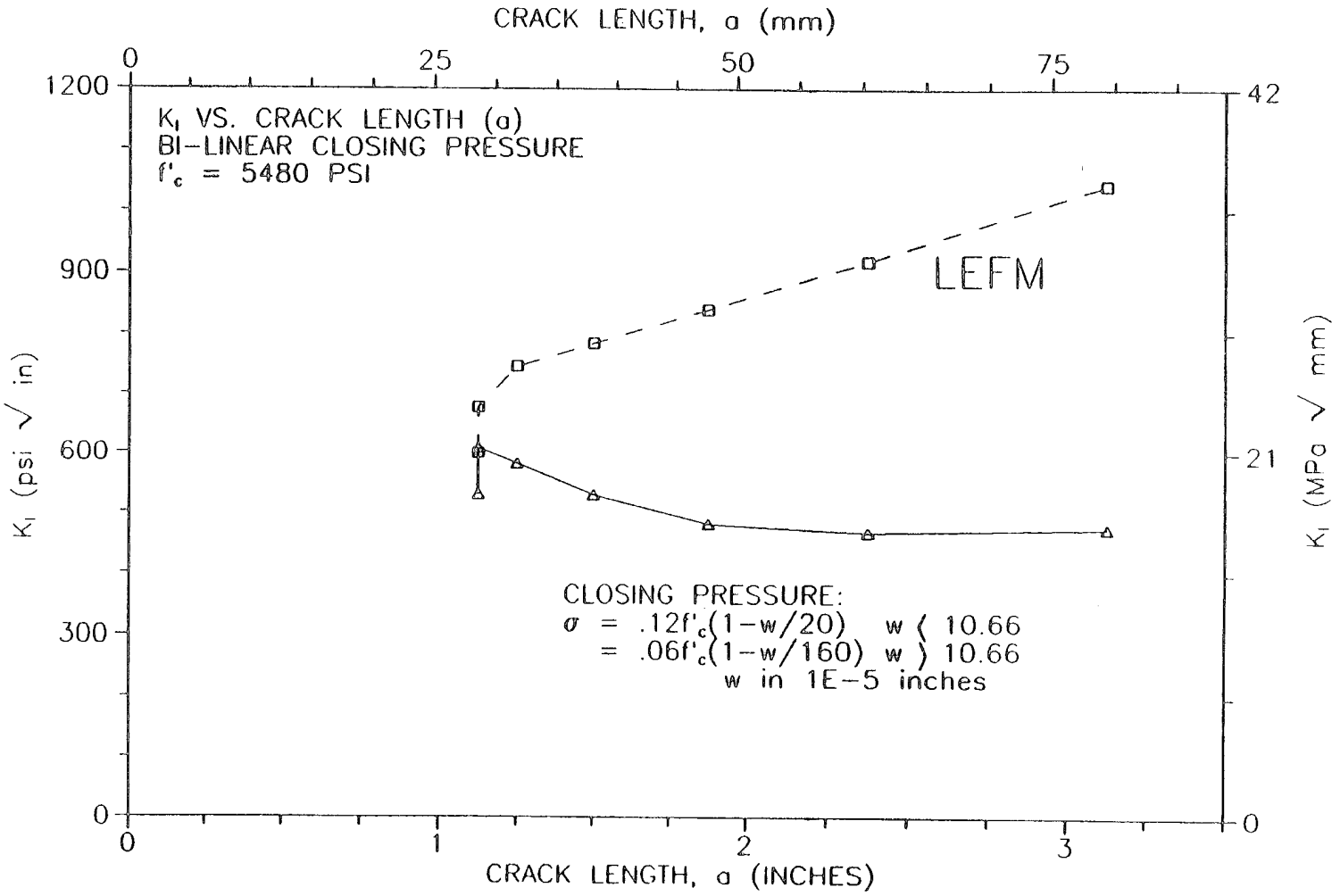

Figure 18 Apparent Mode I Stress Intensity Factor(K_I) vs. Crack Length(a)

SECTION III

CRACK INITIATION AND PROPAGATION IN DISK SPECIMEN (BRAZILIAN TEST)

A. INTRODUCTION

A common method for estimating the tensile strength of concrete is the splitting test. The test is carried out by loading a cylinder on its side in diametral compression. This indirect method to determine tensile strength is attributed to Carneiro (Reference 19) and was adopted the national standard specifications of Brazil, thus the name "Brazilian Test." According to the theory of elasticity, this loading configuration produces a nearly constant stress along approximately 75 percent of the diameter (References 20 and 21). Although the state of stress is not uniaxial (significant compressive stress in the transverse direction) and there is redistribution of stress due to nonlinearity of concrete, the tensile stress value at failure has proven to be a useful measure of the tensile strength. Figure 19 shows the failure sequence in the disk specimen (Reference 22). The purpose of this study is to evaluate the distribution of deformations on the surface of a disk specimen as it is loaded and determine the failure sequence.

B. TESTING PROCEDURE

1. Mechanical Configuration

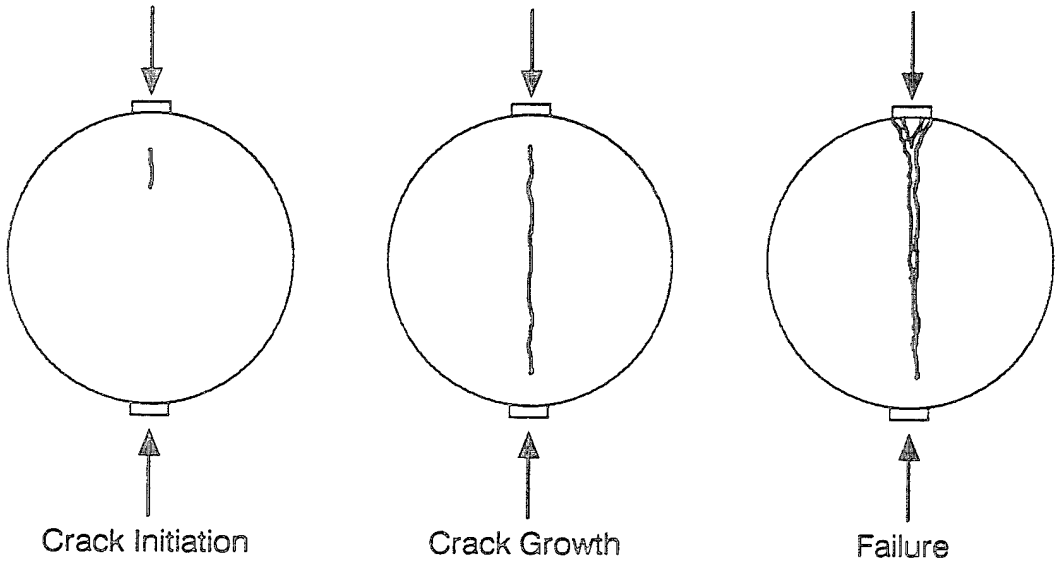

Figure 19 Failure Sequence for the Disk Specimen

The specimens used in this study were mortar cylinders 2 inches x 2 inches (50.8mm x 50.8 mm). The mortar used to cast the specimens had ratios of 1.0/2.0/0.5 (cement/sand/water) by weight. 2-inch x 2.25-inch cylinders were cast and then polished down to 2 inches long to obtain smooth and parallel surfaces. After casting, the specimens were cured in lime saturated water until needed (minimum 90 days). The specimens were loaded diametrically (brazilian test) using the 120 Kip capacity loading frame shown in Figure 20. The use of such a large loading frame was selected because it includes a heavy platform which was used as a vibration free table for the holographic arrangement (see Section III.C). To prevent multiple cracking and crushing at the points of loading, the load was distributed over a finite area, using two loading plates as shown in Figure 21. A filler bonding agent (super glue) was used to provide continuous contact between the loading plates and the specimen. A very thin and stiff filler was used to prevent rigid body displacement of the specimen when the load was applied. Previous

attempts were made using cardboard strips to distribute the load over the desired area, but the deformation of the cardboard during the application of the load was orders of magnitude higher than the deformation of the specimen, resulting in holographic recording reflection the deformation of the loading strip instead of the specimen. The specimens were placed between the loading platens using steel spacers designed to support the instrumentation and keep the specimen 12 inches (309 mm) above the surface of the loading frame platform (Figure 22).

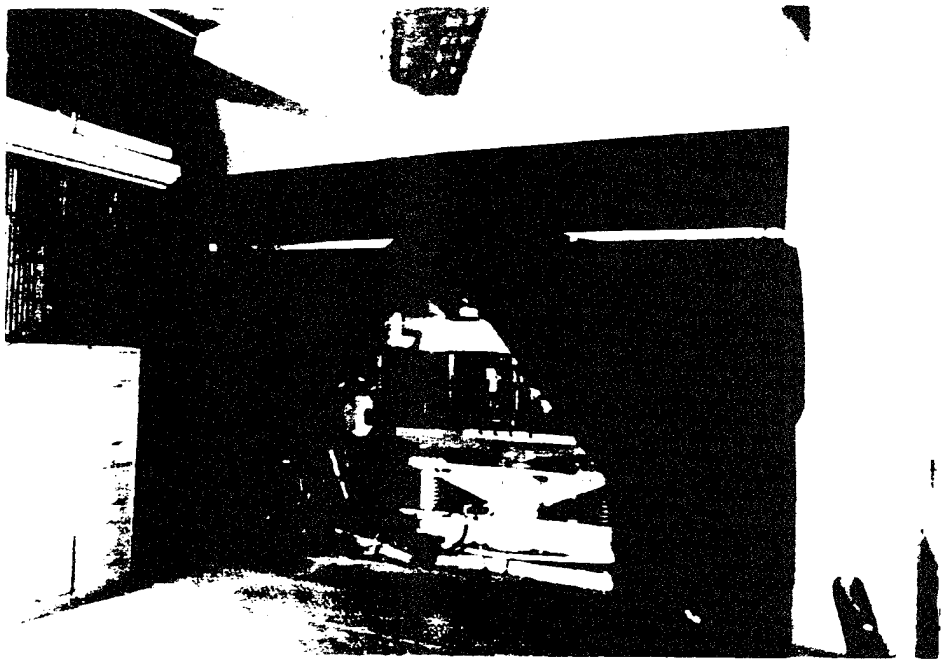

Figure 20 120 Kip Capacity Loading Frame

The compressive strength and modulus of elasticity of each batch of mortar were determined by testing in uniaxial compression 2-inch x 4-inch (50.8mm x 101.6mm) cylinders at comparable age. The same 120-Kip loading frame was used. The dual LVDT transducer shown in Figure 23 was used to measure axial displacement and the applied load was measured using the ΔP transducer of the loading frame. The specimens were tested at constant rate of deformation such that peak load was reached in about 20

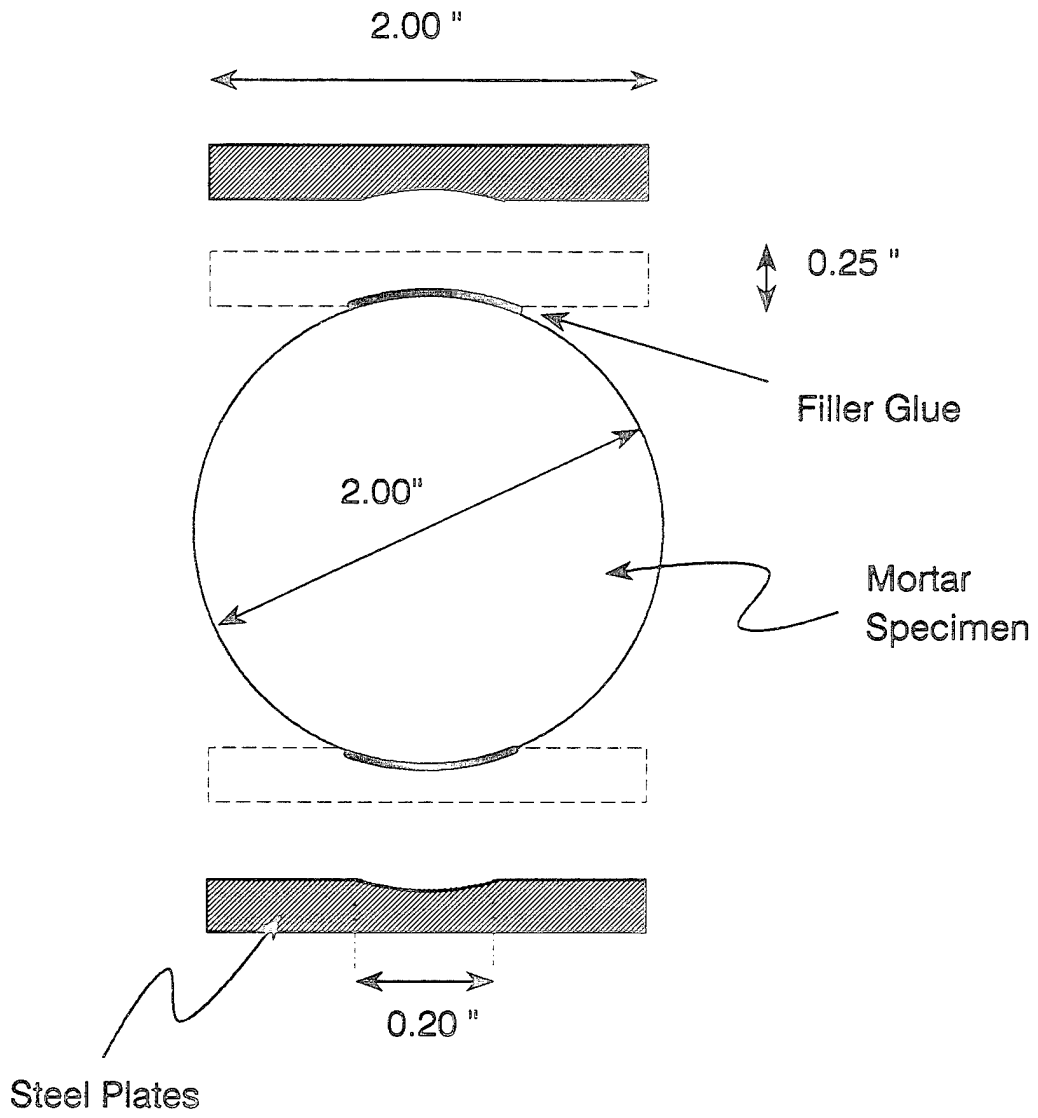

Figure 21 Loading configuration for diametrically loaded cylinder.

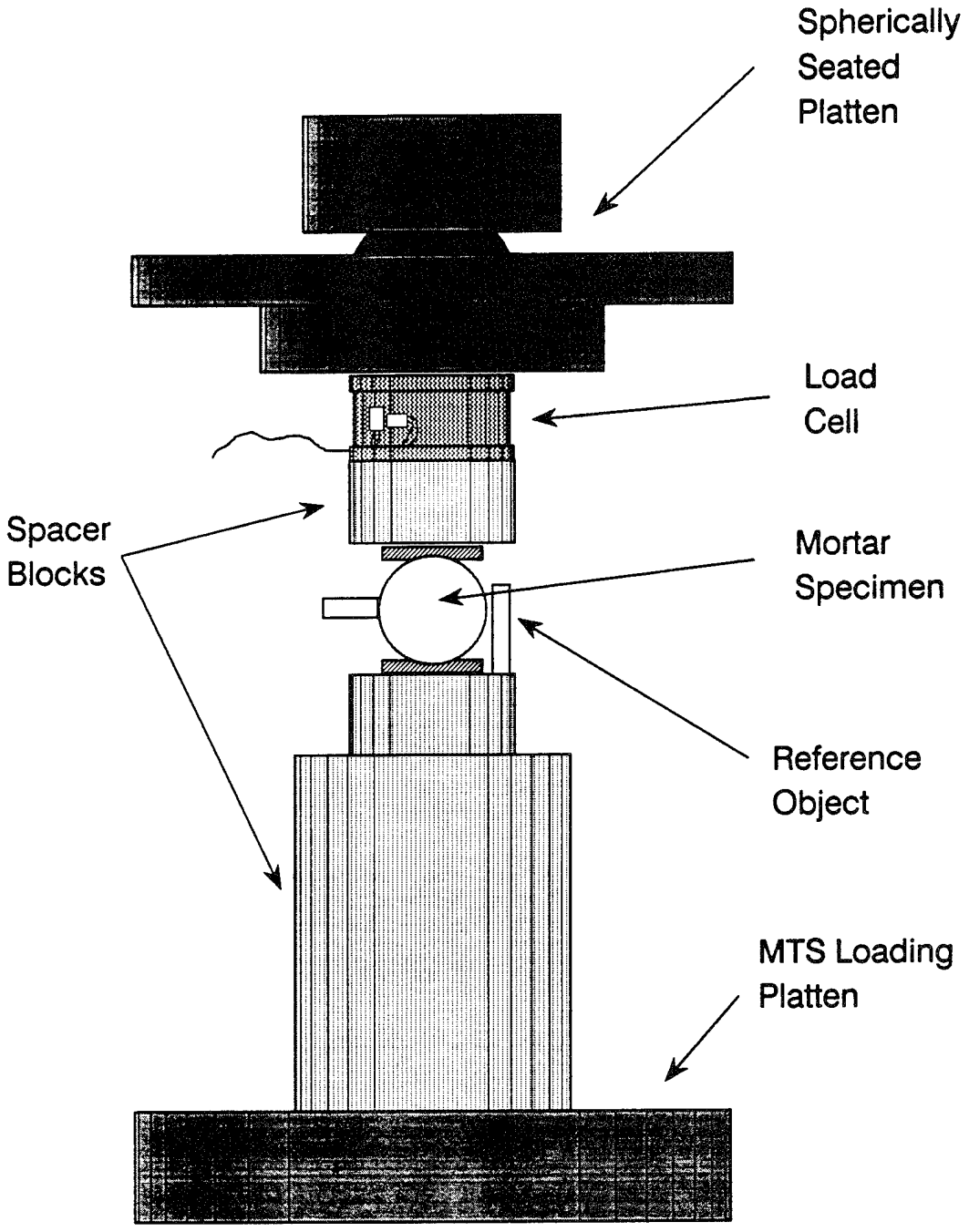

Figure 22 General Loading Arrangement for Disk Specimen (Brazilian Test)

minutes. The results are summarized in Figure 24 and Table 1.

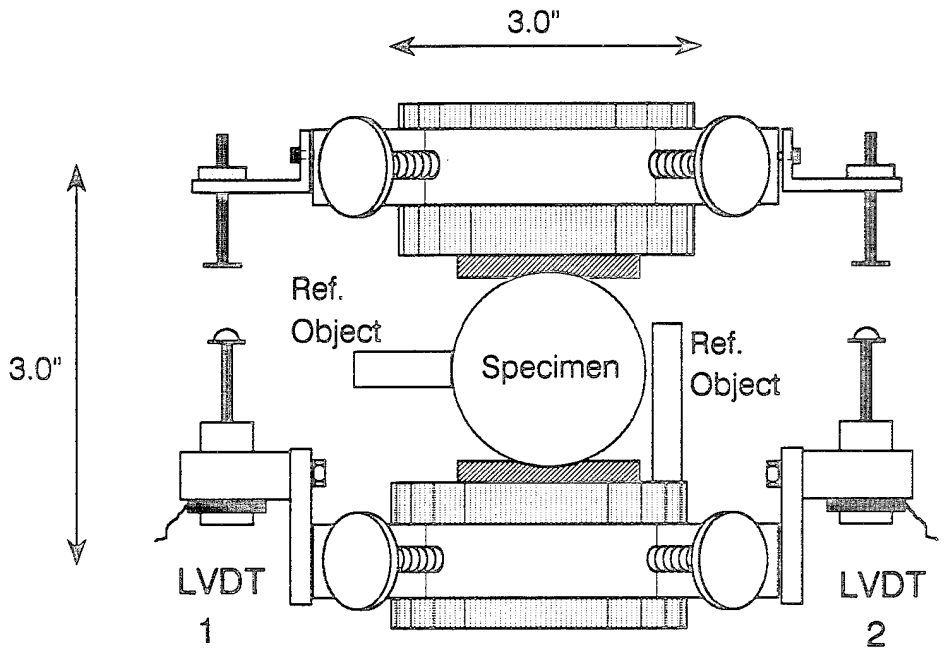

Figure 23 Dual LVDT transducer

2. Instrumentation

Applied load, load-point displacement and diametrical displacement were measured during testing. The ΔP transducer existing in the loading frame was not adequate to measure load levels in the order of 1 to 2 Kips. The cylindrical load cell shown in Figure 22 was designed and fabricated for accurate load measurement and holographic stability. The load cell was designed for a maximum load of 6000 lb in compression. A full

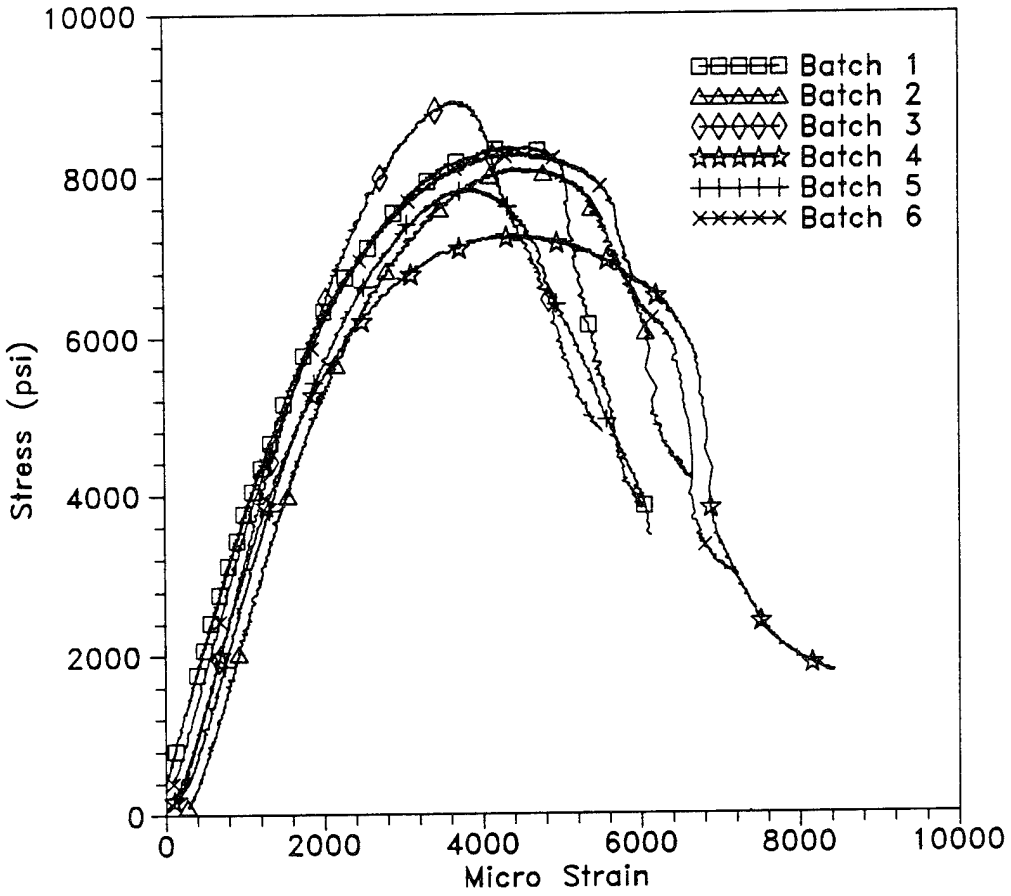

Figure 24 Stress-Strain Curves for Uniaxial Compression Cylinders

Wheatstone bridge was used on the load cell to measure axial load only (eliminate eccentricity effect) and compensate for temperature.

The load point displacement was measured using the same dual LVDT transducer (designed and fabricated during the course of this investigation) used to obtain the modulus of elasticity. As shown in Figure 23, the dual LVDT transducer was attached to the spacer blocks.

TABLE 1 MATERIAL PROPERTIES MEASUREMENT

BATCH	Compressive Strength (f'_c)		Modulus of Elasticity (E)	
	psi	MPa	psi	Mpa
1	8,340	57.6	3.24×10^6	22,400
2	8,090	55.9	3.24×10^6	22,400
3	8,910	61.5	3.61×10^6	24,900
4	7,210	49.8	3.26×10^6	22,500
5	7,840	54.1	3.22×10^6	22,200
6	8,290	57.2	3.36×10^6	23,200

A modified MTS clip gage Model 632.02B.20 transducer was used to measure diametral displacement perpendicular to the loading direction (DD). The clip gage was modified as shown in Figure 25 to allow measurement of the displacement on the center of the specimen (between front and back faces). Target plates were glued to the specimen to provide stable support for the extension legs. The steel spring was necessary to overcome the opening force of the clip gage and insure stable contact between the extension legs and the target plates. The transducer was supported using a second steel spring attached to a magnetic support such that a stable position of the transducer is guaranteed and high frequency vibrations from the loading frame are damped out.

A Zenith personal computer with a Dash-16 I/O Board (Metra Byte Co.) driven by Labtech Notebook (Laboratory Technologies Co.) was used to digitize and record the signals. In addition to the signals from the load cell, dual LVDT and DD transducers, the ΔP and stroke readings were recorded.

3. Control Signal

Preliminary tests were performed in order to determine the most suitable control system. Figure 26 shows a schematic of the results. In the load-load point displacement

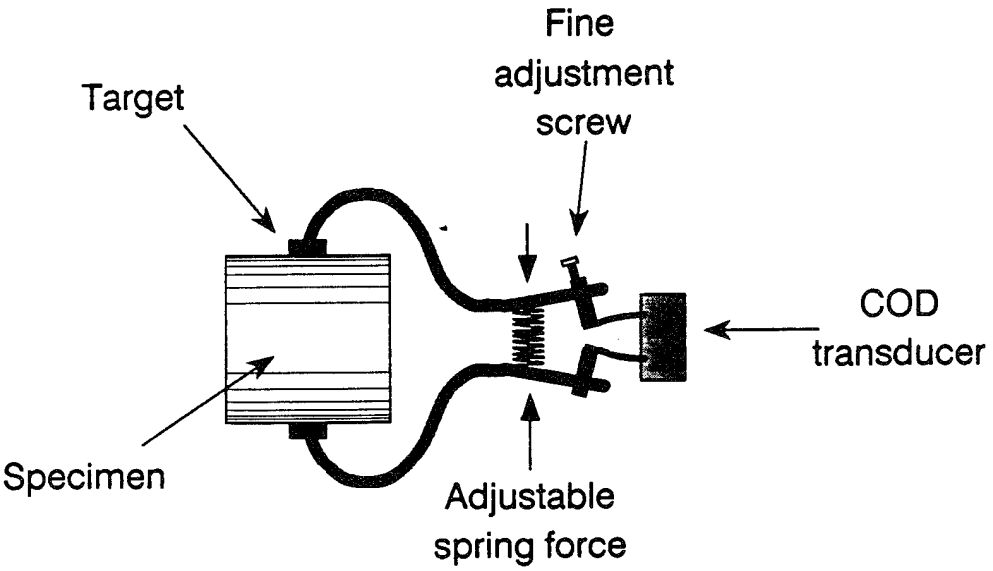

Top View

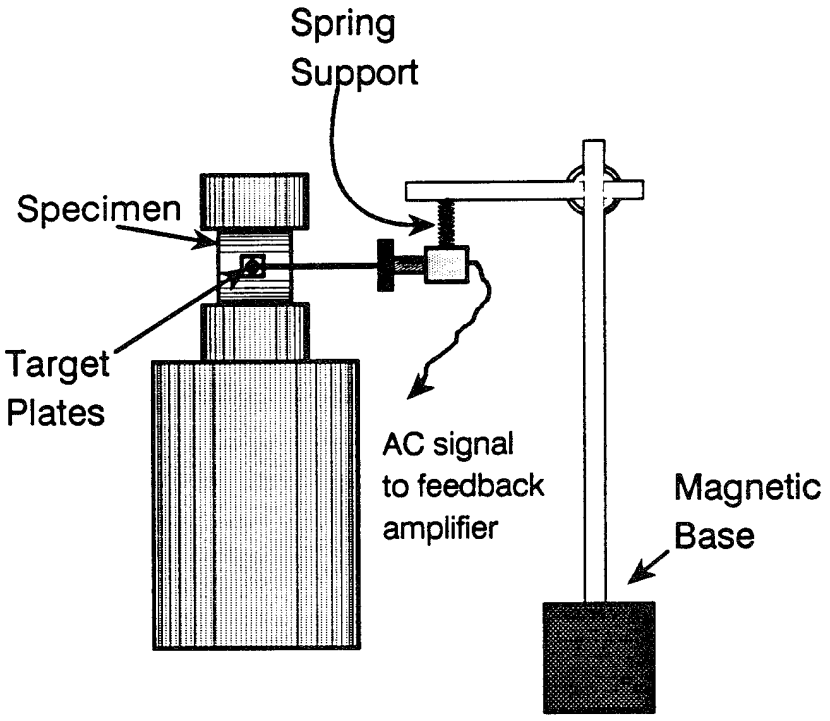

Lateral View

Figure 25 Diametral Displacement Transducer

plot there are three zones: (Zone A) linear increase of the load, (Zone B) transition stage where the first crack propagates and (Zone C) plateau where secondary cracking and final failure occurs. The main drawback of the displacement control system is that the transition stage is unstable (drop of the load at constant displacement).

The load-DD curve also shown in Figure 26 includes the same three zones. The DD in zone A, corresponding to the elastic stage, is almost zero. If this signal was used for control, a sudden increase in the load would occur prior to cracking. Zones B and C show the desired stable behavior (i.e. continuous increase of the DD) after cracking has started.

A new control system was designed in order to have stable behavior throughout the loading sequence. Figure 26 shows that in Zone A the load increases while the DD remains constant while in zones B and C the load variation is small and the DD increases. By selecting a linear combination of the load and DD signals the desired response is obtained as illustrated in Figure 26. Note that the load + DD signal continuously increase in all stages of the loading sequence.

Since the addition of two signals cannot directly be used for control by our analog closed loop control system, a feedback control system was designed. Figure 27 shows a block diagram of the testing system. In this diagram the shaded areas correspond to the components developed during the course of this investigation. Figure 28 shows a block diagram of the load + DD feedback control amplifier. The main components of the control amplifier are two channels of preamplifiers, a signal summator and three output drivers. The preamplifiers are used to select the relative weight of the load and DD signals. The summator is used to add the preamplified signals and the output drivers are used to control the calibration factors and provide separate load, DD and load + DD signals for monitoring and recording.

C. HOLOGRAPHIC INTERFEROMETRY TEST

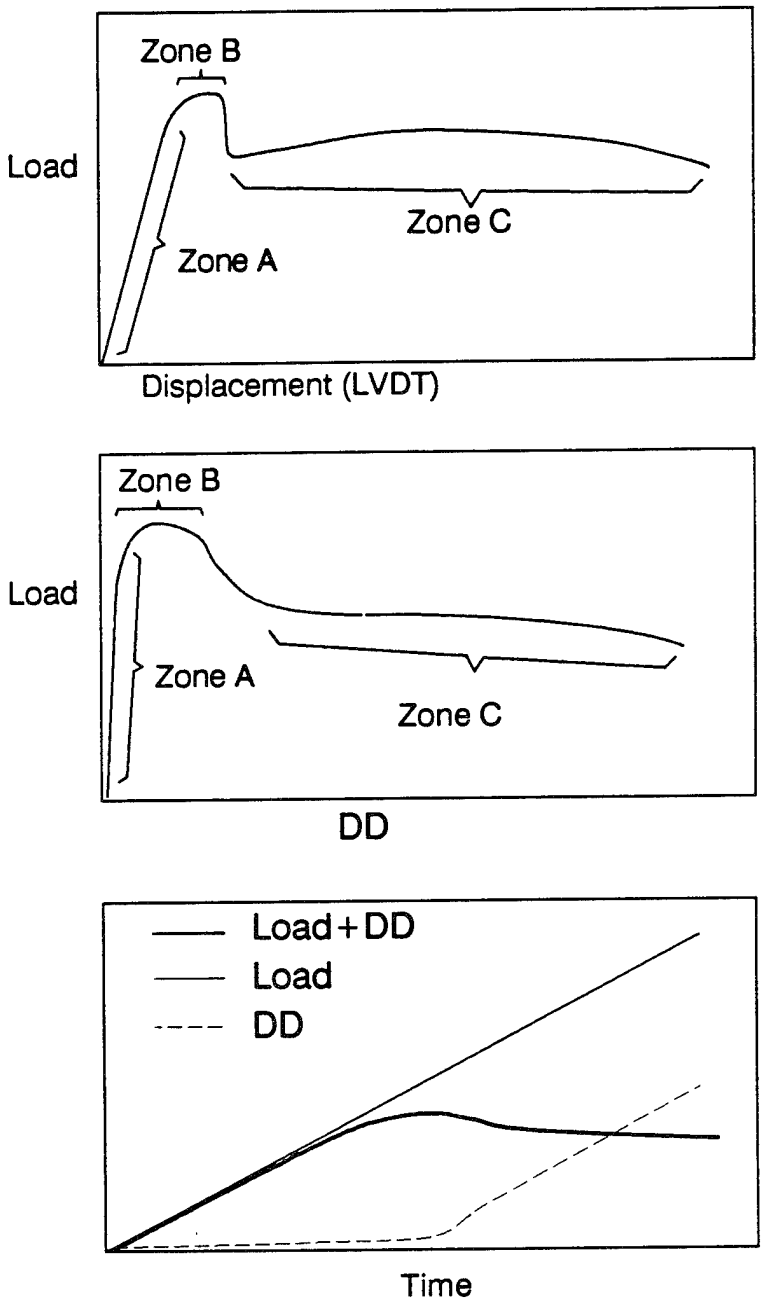

Figure 26 Control Signal

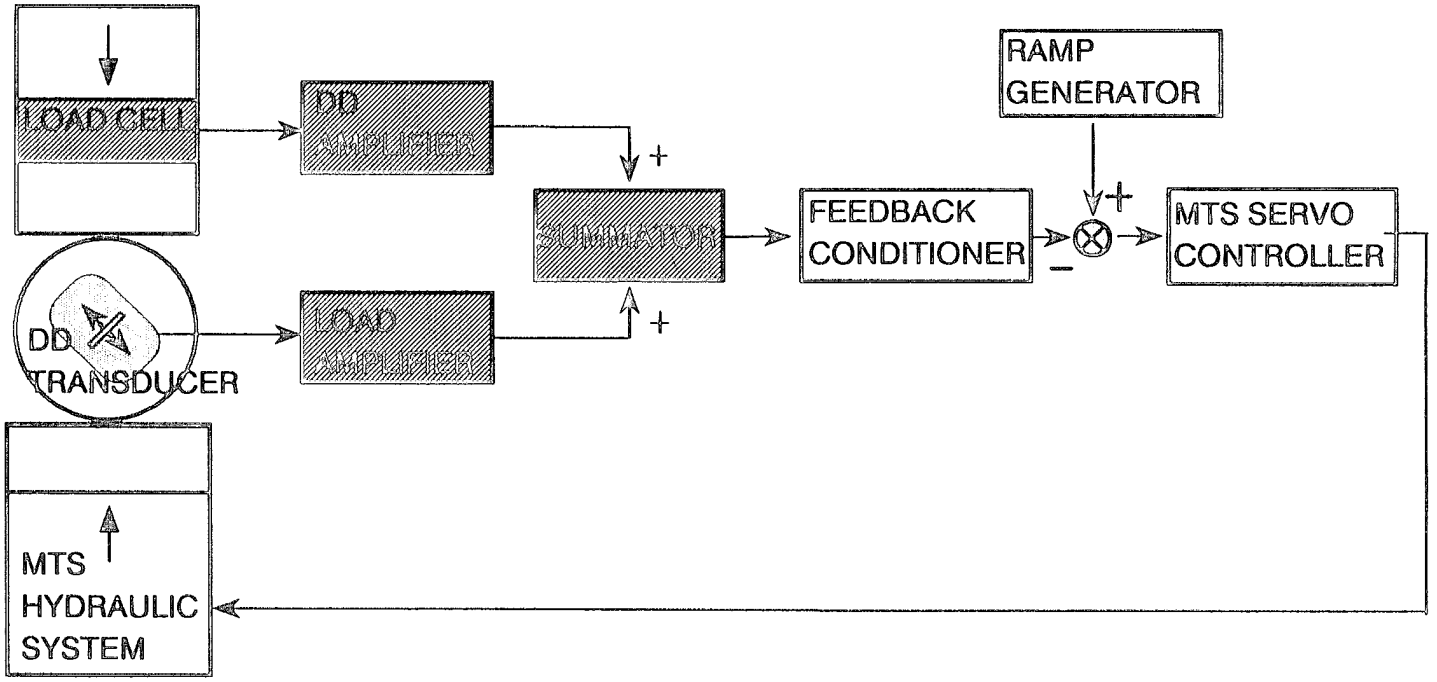

Figure 27 Closed Loop Control System

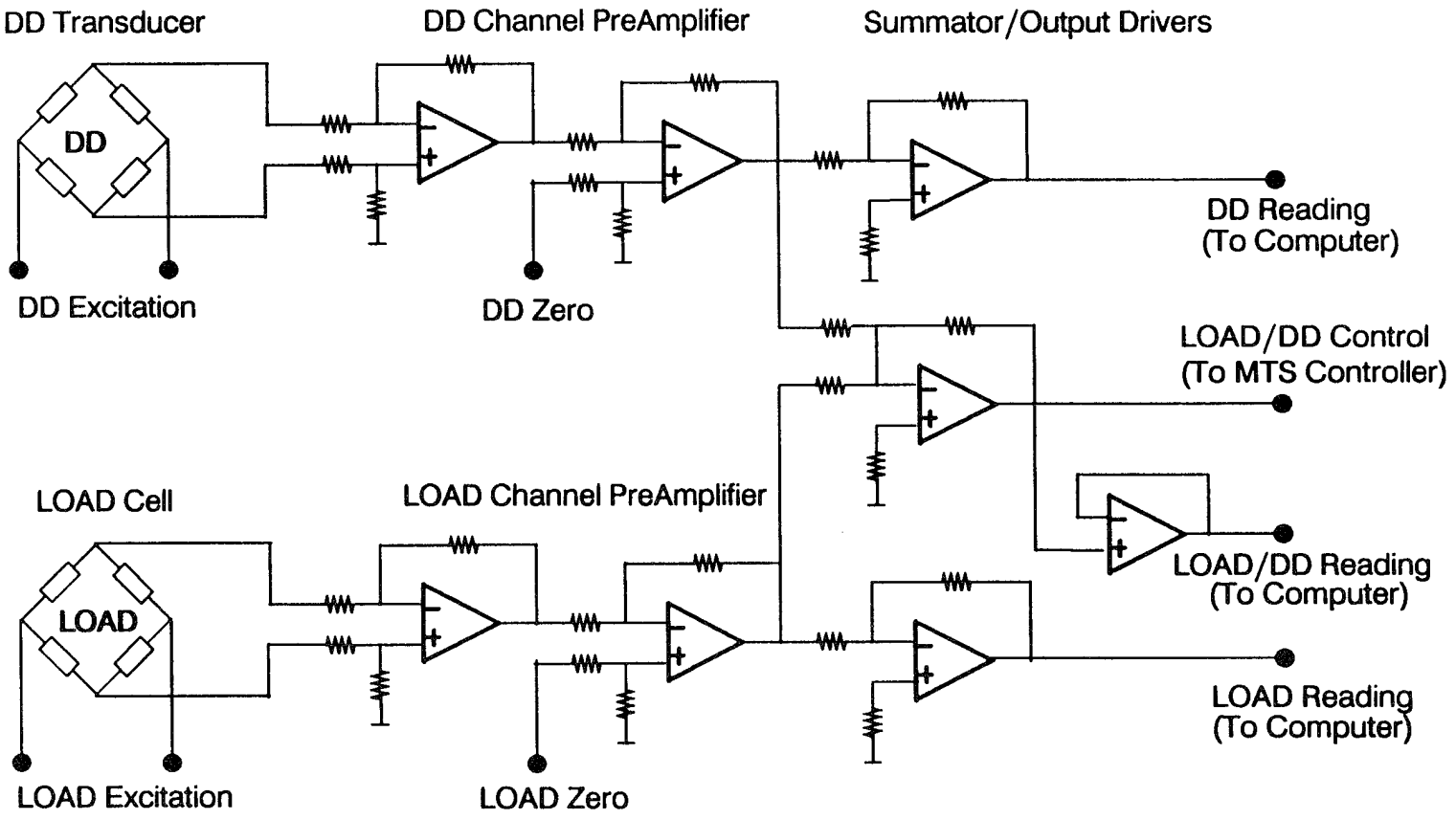

Figure 28 Load+DD Feedback Control Amplifier

To measure three dimensional displacement fields a three sensitivity vector holographic arrangement was required (see Section III.E). Split beam transmission sandwich holography (see Section II.C) was used. The complete optical arrangement is shown in Figures 29 and 30. For better use of the limited space two horizontal planes were used

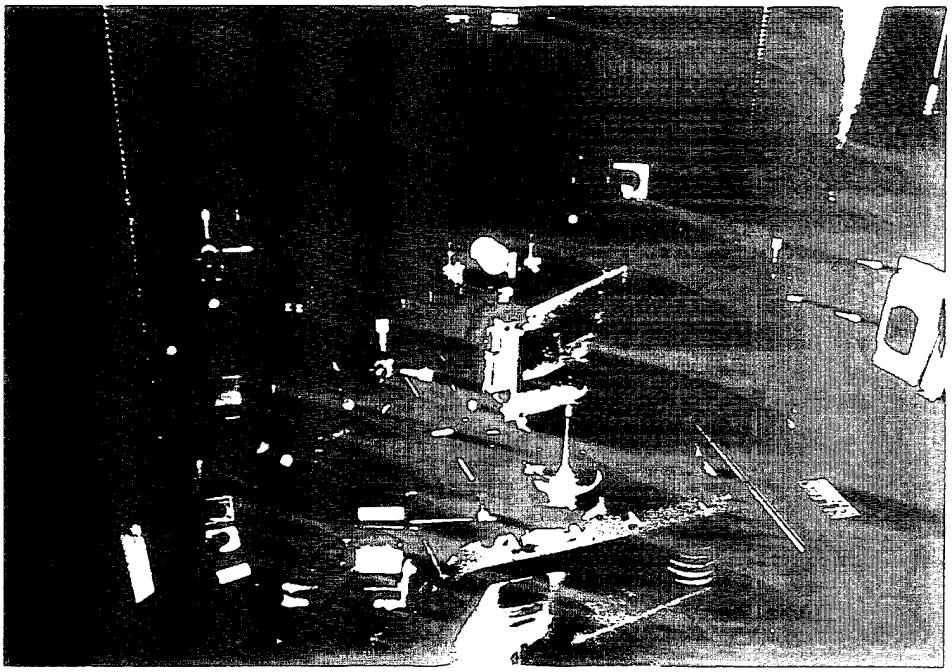

Figure 30 Optical Arrangement for Three Sensitivity Vectors

for the optical arrangement (as opposed to the more conventional single-plane setup). For easier understanding of the operation of the holographic setup, Figure 31 shows only the most significant components of the arrangement. To obtain three different sensitivity vectors, a common reference (r) beam and three different object beams (R,L,D) were used.

As noted in Section II.C, holographic interferometry experiments must be performed under very stable conditions. Conventionally, noise, light, air currents and vibrations are isolated from the system through the use of devices such as vibration isolation tables and noise dampers. However, during this investigation, the use of the servo-controlled closed

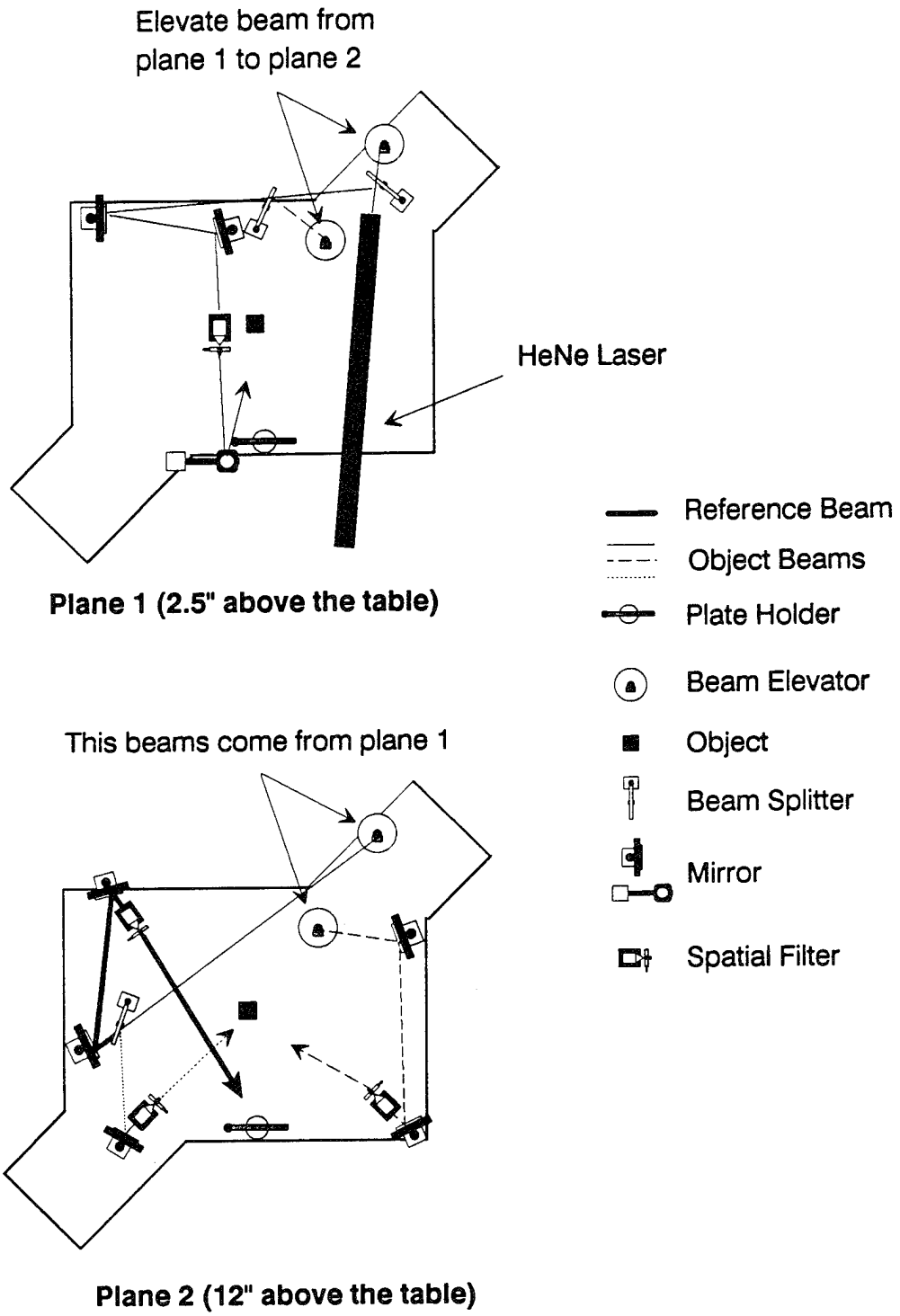

Figure 29 Optical Arrangement for Three Sensitivity Vectors (Schematic)

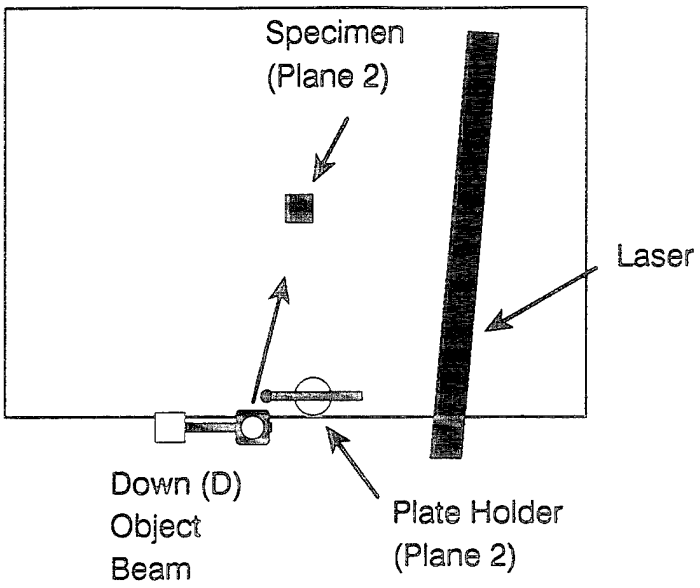

Plane 1 (2.5" above the table)

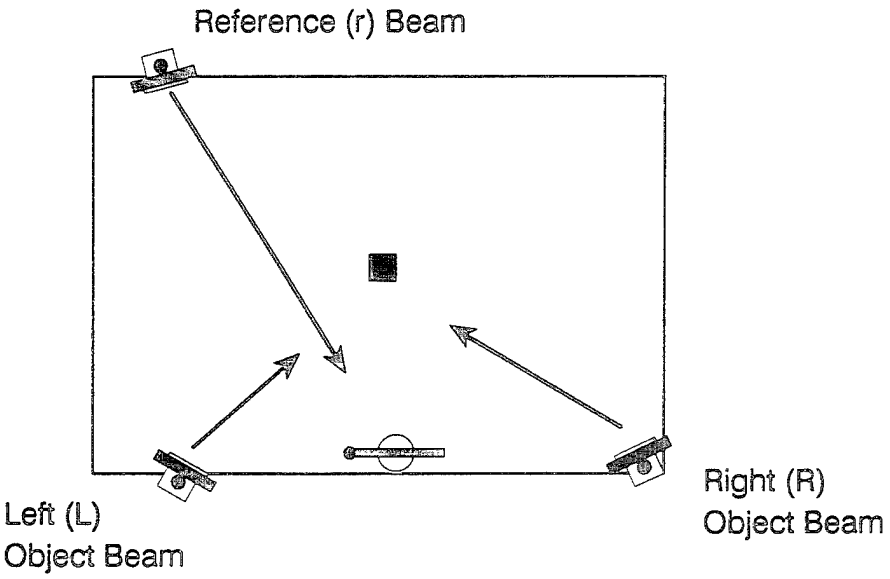

Plane 2 (12" above the table)

Figure 31 Simplified Holographic Arrangement for Three Sensitivity Vectors

loop testing system was essential for the appropriate mechanical behavior. Extreme care was placed in the adaptation of the laboratory for holographic recordings. The hydraulic pump was placed on rubber dampers to reduce vibrations transmitted through the floor to the loading frame. A tent made of light tight fabric was built around the testing frame to avoid air currents and provide dark room conditions. The plate holder shown in Figure 32 was designed to record three holograms on the same photosensitive plate which eliminates the vibrations induced by changing plates after each exposure. Also, after the plate has been developed and the real-time technique is used to determine the size of the load increment, all three holograms can be viewed at the same time. Thus, there is no need to "guess" the critical component of the displacements. A Richo XR-M camera without lens was programmed to make three exposures at 30-second intervals and placed in front of the laser head to act as a shutter. For each exposure, only one of the object beams was active (the other two were blocked with cardboard screens). In addition, all holographic experiments were performed overnight or on weekends to avoid the noise generated by normal use of the building. Before an experiment was performed, all the mechanical components were tightened, the transducers were mounted and the electronic systems were operated for 24 hours to allow for all the components to "seat" into a stable position. The electronic systems were started 24 hours in advance and the hydraulic system was started 3 hours in advance in to reach thermal stability of the system. Since the duration of a holographic experiment is approximately 8 hours and holographic stability must maintained throughout the whole process, even with all these precautions, the success ratio of the holographic experiments was approximately 1/10.

Two reference objects were included in the holographic recordings (Figure 22). One was glued to the spacer block and the other to the specimen. The reference object on the spacer block was used to determine, in case of low quality holograms, if the source of motion was due to variable load applied on the specimen or vibration on the loading platform itself. The second reference object, glued to the specimen, was used to evaluate the rigid body displacement.

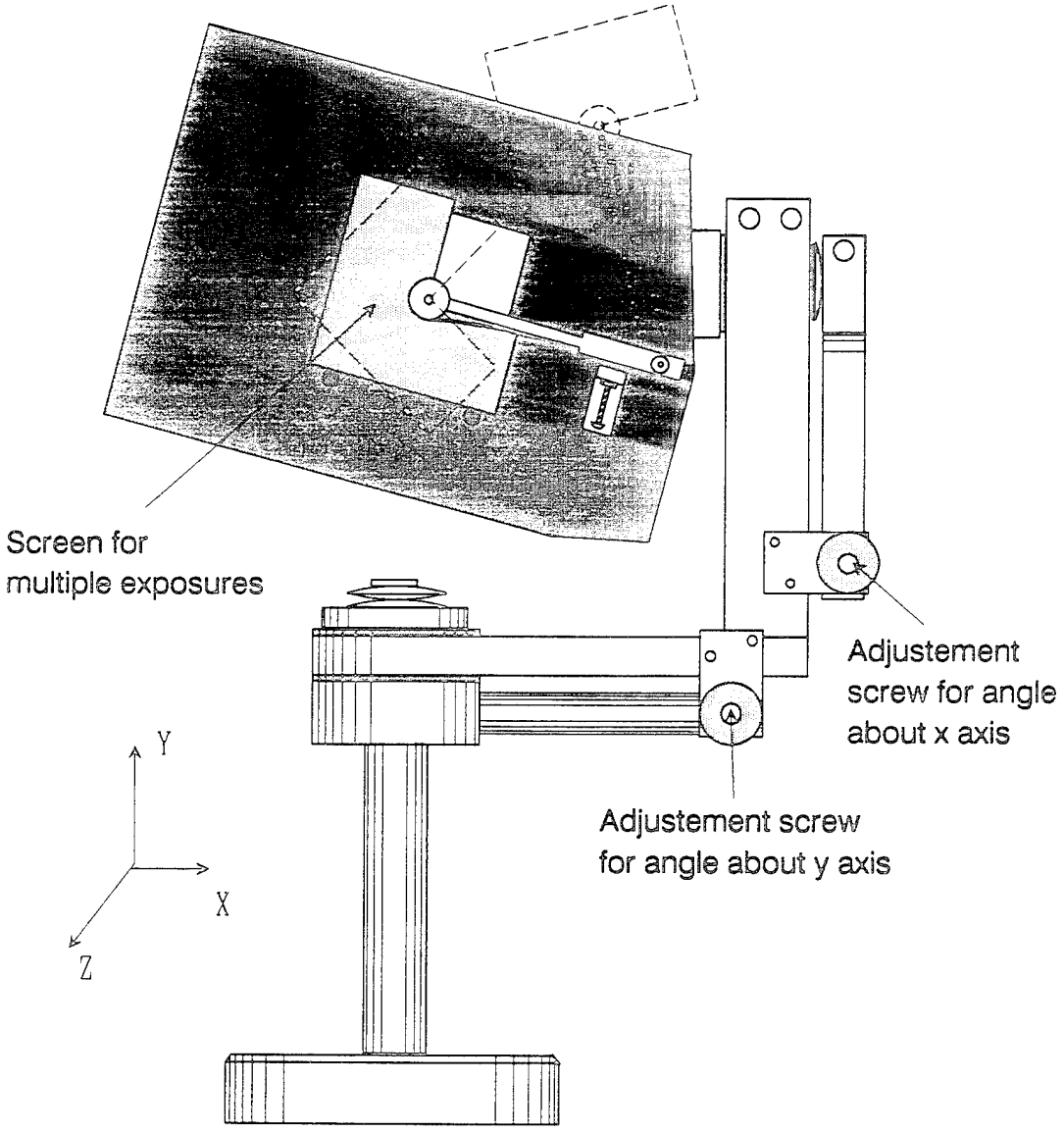

Figure 32 Plate Holder for Multiple Exposures

D. IMAGE PROCESSING (ELIMINATION OF RIGID BODY MOTION)

Holographic interferometry is sensitive to displacements, including both rigid body motion and displacements induced through deformation. In the study presented in Section II, the effect of the rigid body motion was neglected because the mechanical configuration allowed only rotation about the axis of loading. If the horizontal component of the relative displacement between Points A and B in Figure 33 is calculated, the rigid body motion displacement of Point A is the same as that of Point B. Thus, an arbitrary point of zero displacement can be selected and incremental displacements with respect to this point suffice to compute the deformation field.

However, in this study, three-dimensional deformation fields are computed. Unless the point of zero displacement (with respect to the photographic plate) is on a known position on the surface of the object, elimination of rigid body motion is necessary.

Abramson (Reference 13) showed that the rigid body motion can be eliminated from an interferogram by subtracting the fringe pattern corresponding to the rigid body motion alone. The rigid body motion can also be eliminated by rotating the sandwich holograms. However, as also noted by Abramson, the rigid body motion component provides additional information regarding the direction of the displacements.

The surface of the mortar specimen was subjected to both deformation and rigid body motion between holographic exposures, but the reference object glued to the side of the specimen was only subjected to rigid body motion. Figure 34 shows an original gray image of an interferogram of the disk specimen. Note that both the reference objects contain holographic fringes (rigid body motion). Also note that the fringe patterns on both reference objects are different which suggests that there was displacement of the specimen with respect to the loading block. The fringe orders were evaluated as in described in Section II.D.2 resulting in Figure 35. In this image, the fringe orders have integer values (fringe numbers). Note that the reference object was also colorized. The fringe order between the reference object and the mortar specimen does not have to be continuous but the direction of positive fringe count has to be consistent.

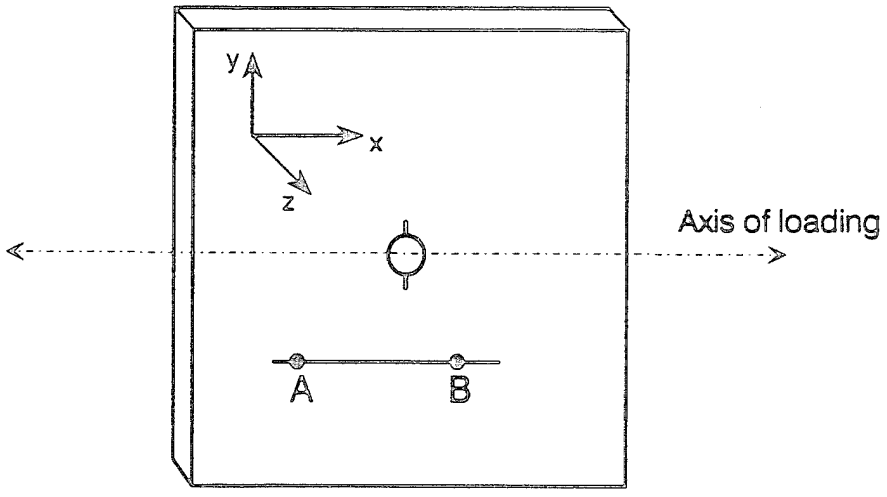

Before Rigid Body Motion (RBM)

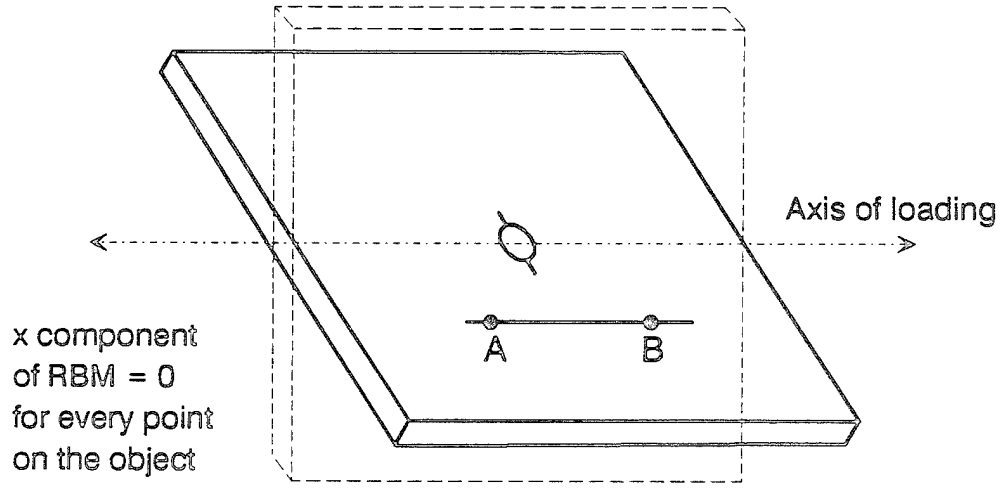

After Rigid Body Motion (RBM)

Figure 33 Effect of Rigid Body Motion on Center Notched Plate Specimen

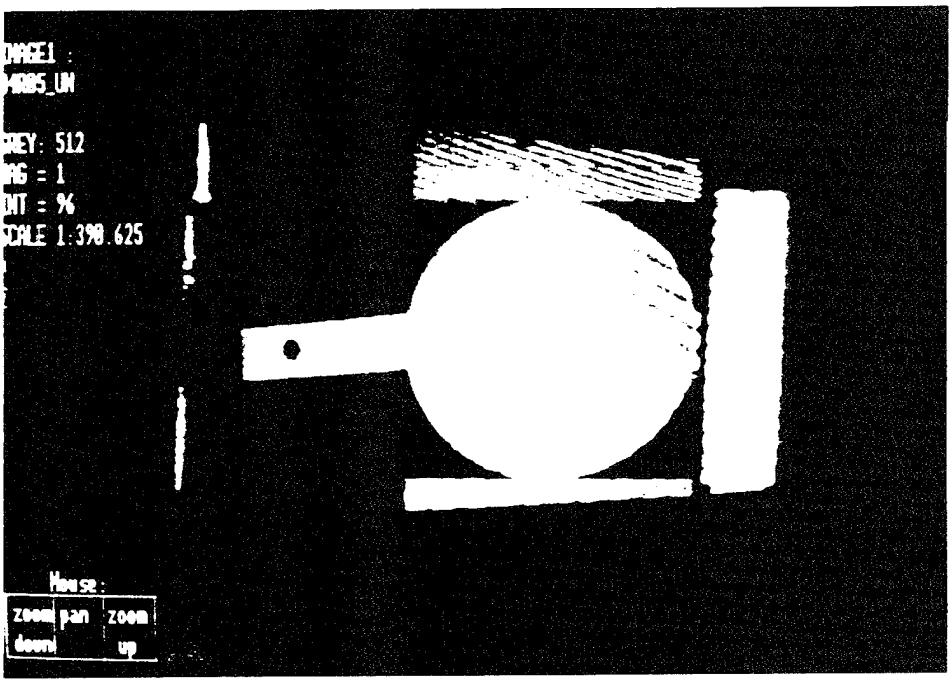

Figure 34 Holographic Interferogram of Disk Specimen (Original Image). Hologram 3

Direct application of the Moire pattern method (superimpose a grid of the same orientation as density as that on the reference object on the entire image) results on elimination of the rigid body motion but the transition between bright and dark fringes becomes ambiguous (Figure 36). A computer program was written to mathematically subtract the fringe patterns based on the orientation and density of the reference grid and the distance to the point of zero displacement (fixture between specimen and reference object). The fringe order at any point P on the object after fringe superposition is given by Equation (5).

$$I = I_1 - [(\boldsymbol{of} \times \boldsymbol{A}) \cdot \boldsymbol{k}] \, df \qquad (5)$$

where:
- I Fringe order after rigid body motion elimination
- I_1 Original fringe order
- $\boldsymbol{of}$ Unit vector defining the orientation of the reference grid

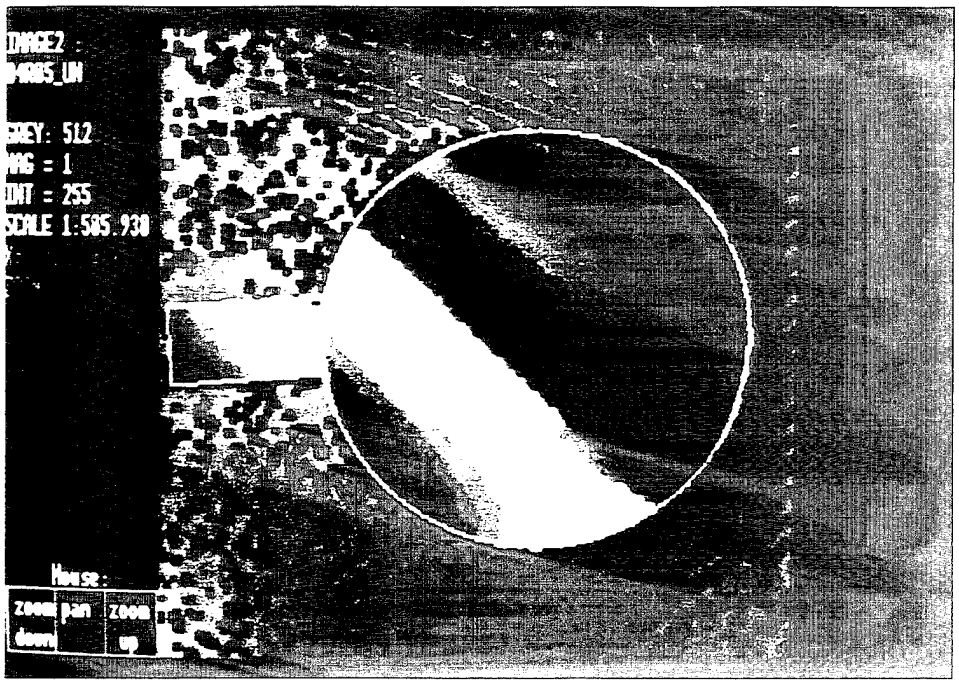

Figure 35 Colorized Fringe Pattern Before Elimination of Rigid Body Motion. Hologram 3

df	Fringe density (fringes/unit distance)
A	Vector from point of zero displacement to point P
k	Unit vector in the z direction (out of plane)

Note that in this equation the original fringe orders are real values obtained by Equation (2). Therefore, the fringe orders in the resulting image shown in Figure 37 are also real numbers. This fringe orders can directly been used for displacement calculation.

E. EVALUATION OF HOLOGRAMS (STRAIN FIELDS)

In a holographic setup, if the distances between observation points and illumination point to the object are large compared to the magnitude of the displacements, the following linear approximation can be made to the exact holodiagram solution (Figure 9). The displacement vector d can be decomposed into three orthogonal components, one along the sensitivity vector k (defined as the bisector of the angle IPO in Figure 38) and

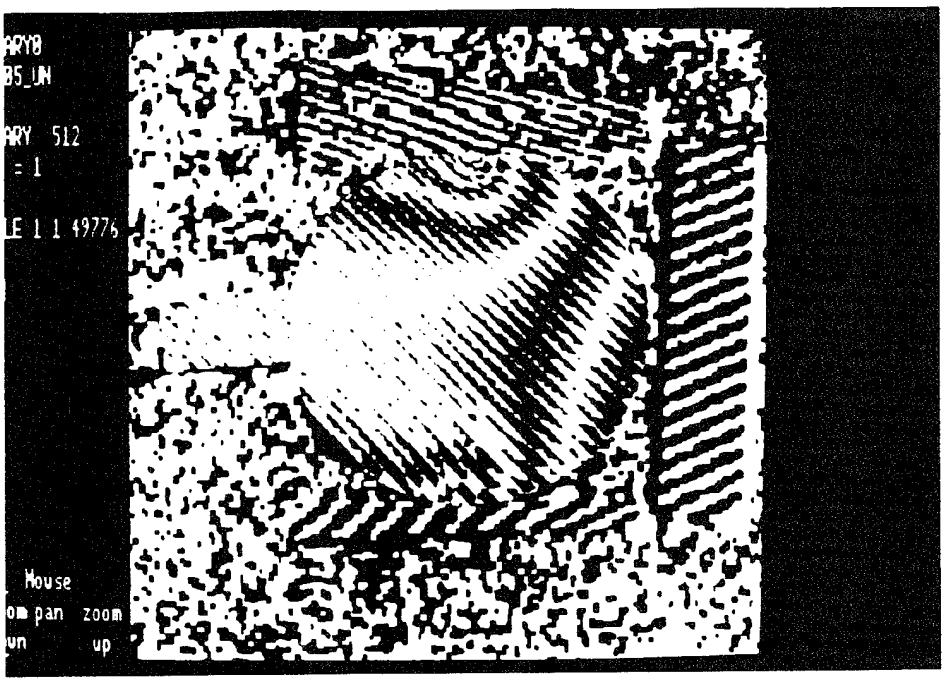

Figure 36 Elimination of Rigid Body Motion by Direct Moire Patter Superposition. Hologram 3

two perpendicular to **k**. For small displacements, motion of the point P perpendicular to **k** cause no change in in the path length I-P-O (the perpendicular motions are along the ellipse having I and O as the foci). The linear approximation of the displacement **d** is given by:

$$\boldsymbol{d} \cdot \boldsymbol{k} = \frac{\Delta(I\text{-}P\text{-}O)}{2\cos\alpha} = \frac{n\lambda}{2\cos\alpha} \qquad (6)$$

To separate the tree components of the displacement in the most general case, independent holographic readings have to be made with three different (non-coplanar) sensitivity vectors and the above equation takes the form:

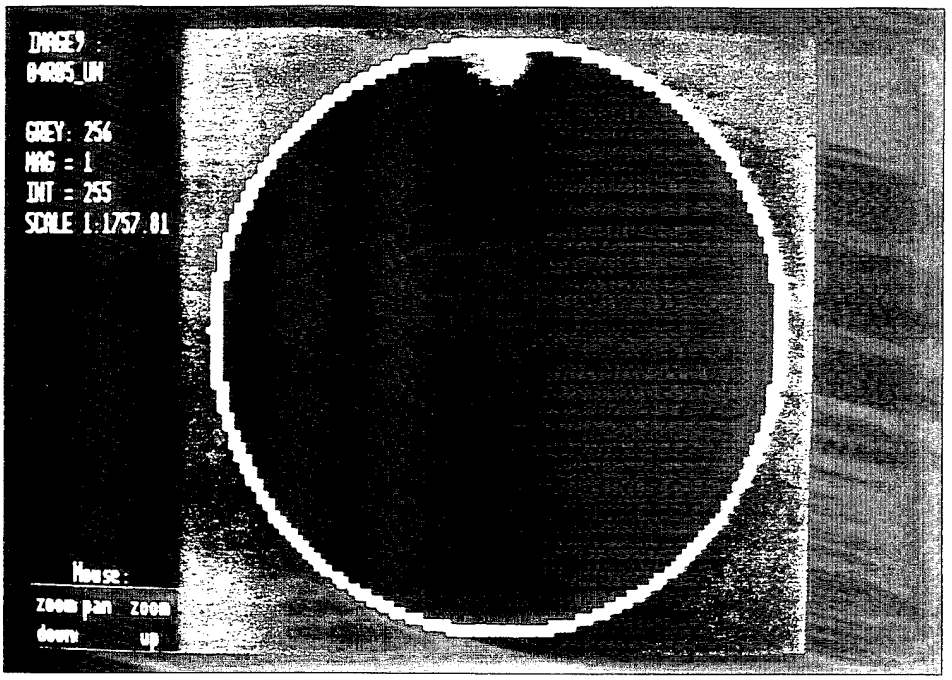

Figure 37 Colorized Image After Mathematical Elimination of Rigid Body Motion. Hologram 3.

$$\vec{d} \cdot \vec{k}_i = \frac{n_i \lambda}{2 \cos\alpha_i} \tag{7}$$

In this equation, the displacement vector $\vec{d}$ is a function only of the fringe counts n_i, and the known wave length λ and geometrical constants $\vec{k}_i$ and α_i.

A computer program was written to compute the displacements using the linear solution described above to evaluate displacements in a multiple-sensitivity vector holographic system. Displacements were evaluated every tenth of a inch on the surface of the specimen. The procedure described in Section II.E.2. was used for strain computations.

The load history is shown in Figure 39. The plateaus on this curve correspond to the time necessary to process the holographic plates during which the load was kept constant. In this figure, the stars correspond to the state when a hologram was made as shown in Table 2. Figures 40 to 44 show the strain fields (ϵ_{xx}) at three stages of

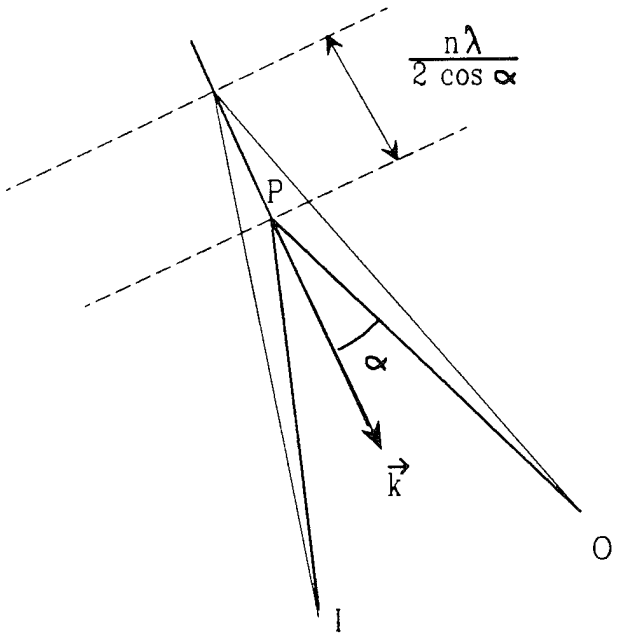

Figure 38 Linear Approximation for Evaluation of Holograms

loading. The linear elastic solution was obtained using FRANC (FRacture ANalysis Code), an interactive finite-element program that models crack tips though six-node quarter point node traingular elements and provides automatic remeshing and crack propagation (Reference 23). Note that both the holographic and the linear elastic strain fields correspond to the increment of strain from the initial preload state of 383 pounds to the given load level. Holograms 3 (Figures 37 and 40) give a typical strain distribution in the "elastic" range. The measured values show the same trends and maximum tensile strain of 100 $\mu\epsilon$ as the numerical solution. However, the holographic results show a concentration of strain near the point of application of the load at the bottom of the specimen, which may suggest that even at this load level (first crack at 2,738 pounds) the crack initiation location can be predicted. Holograms 11 (Figures 41 and 42)

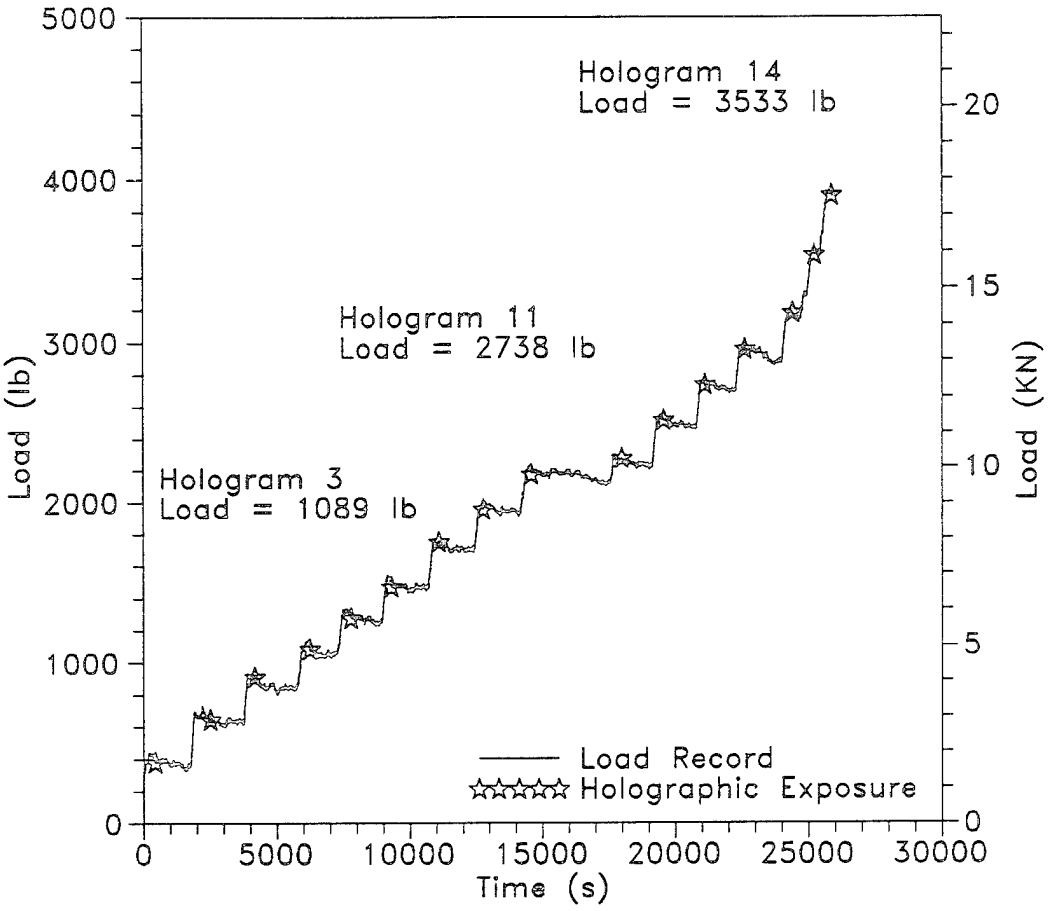

Figure 39 Load History. Specimen HOLO-UN-1

correspond to the crack initiation stage. At this load level the crack is 0.1 inch (2.5 mm) long (crack lengths are accurate within 0.05 in) starting 0.15 inch above the lower load point. Comparison of the holographic strain fields with the LEFM solution (assuming a 0.1 inch crack) shows the same behavior described in Section II.E.2 for the center loaded plate specimen. The holographic results show a concentration of strain around the crack tips but it is not as sharp as the increase in strain corresponding to the numerical

TABLE 2 HOLOGRAPHIC RECORDINGS. SPECIMEN HOLO-UN-1

Holographic Recording	Time	Load	
	s	lb	N
P (Preload)	427	383	1,724
1	2,500	648	2,916
2	4,163	913	4,109
3	6,250	1,089	4,901
4	7,800	1,281	5,765
5	9,310	1,472	6,624
6	11,116	1,752	7,884
7	12,785	1,958	8,811
8	14,584	2,179	9,806
9	18,000	2,282	10,269
10	19,560	2,517	11,327
11	21,113	2,738	12,321
12	22,600	2,959	13,316
13	24,400	3,180	14,310
14	25,200	3,533	15,899
15	25,860	3,901	17,555

solution. A second strain concentration is observed near the top of the specimen indicating probable crack development after further loading. A significant difference between this study and the center-notched plate specimen presented in Section II is that the strain levels are significantly higher for the cylinder specimen as compared with the center loaded plate specimen even on the uncracked region. This can be attributed to the presence of high compressive stresses in the transverse direction but it has not yet been investigated. Although further analysis is necessary, a preliminary investigation based on the elastic solution shows that the mode II (shear) stress intensity factor (K_{II})

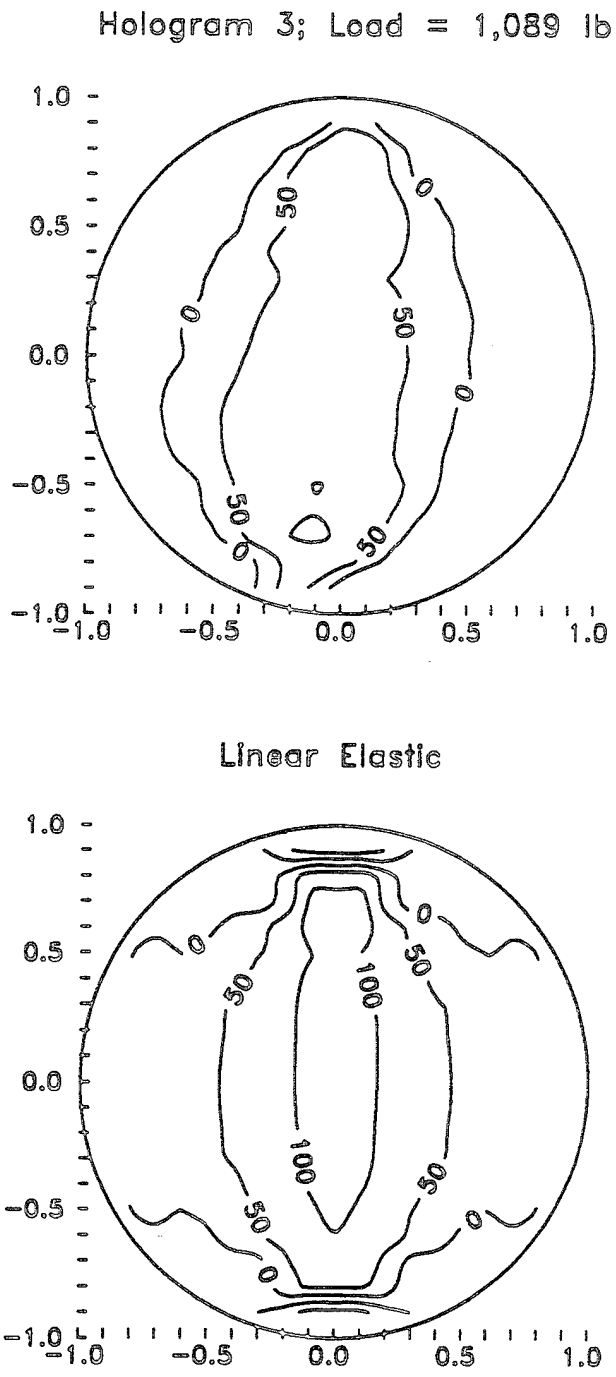

Figure 40 Strain Fields. Hologram 3; Load = 1,089 lb

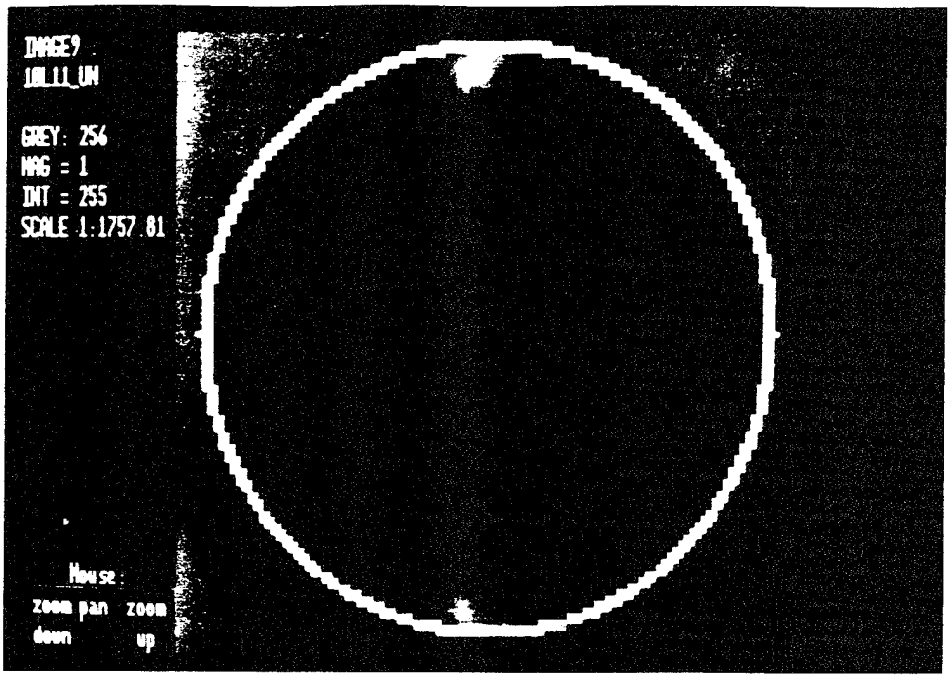

Figure 41 Interferometric Fringes. Hologram 11.

is approximately 10 times higher than K_I.

Holograms 14 (Figures 43 and 44) were taken at the last stable load level and can be considered the failure stage. At this load stage, strain could not be obtained experimentally near the points of application of the load. The size of the interferometric fringes was beyond the resolution of the optical system used. It was inconclusive if the crack propagated to the edges of the specimen or not. At this stage the crack has grown 0.2 inch towards the center of the specimen. For this crack length, the elastic solution shows the sharp strain relaxation behind the crack tip typical of noncohesive cracks while the experimental results still show significant strain behind the crack tip. At the crack tip near the center of the specimen, the LEFM K_{II}/K_I ratio is approximately 1.

Additionally, Figure 45 shows two interferograms corresponding to exposures at 3901 pounds of applied load. Note that the crack length is different for interferograms 14D15 and 14R15 (Down and Right object beams respectively), which indicates crack propagation between exposures for the same applied load. The third hologram (14L15)

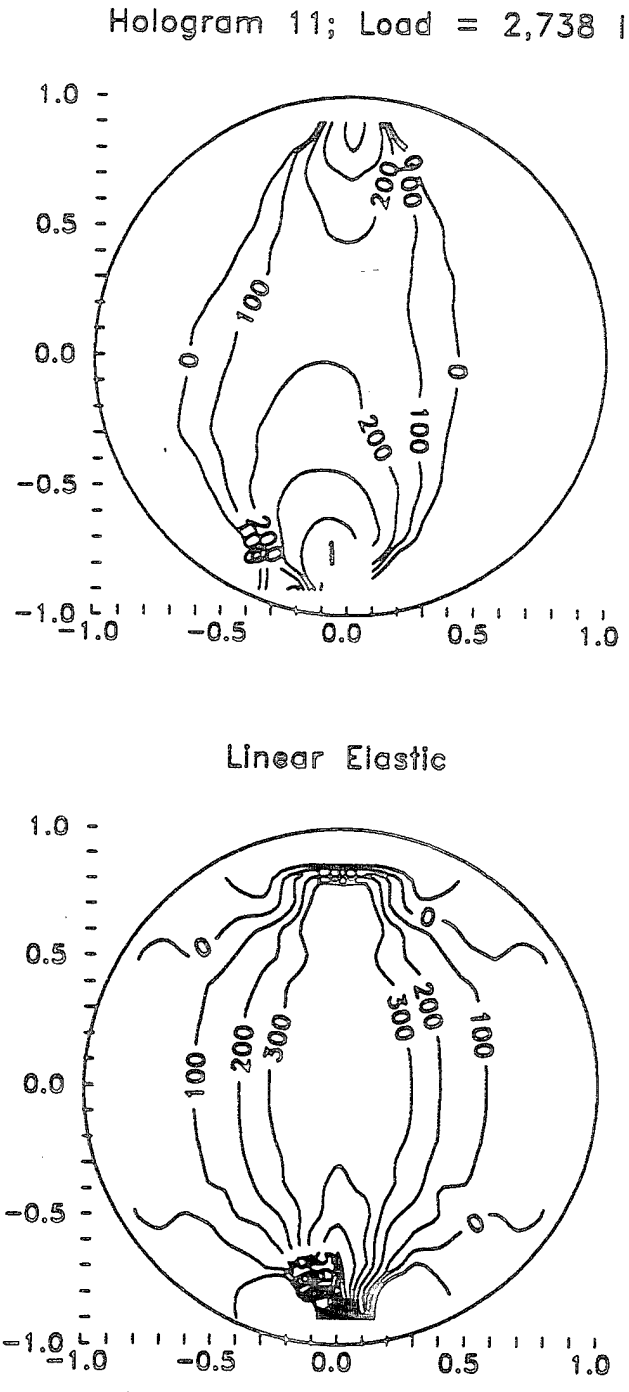

Figure 42 Strain Fields. Hologram 11; Load = 2,738 lb

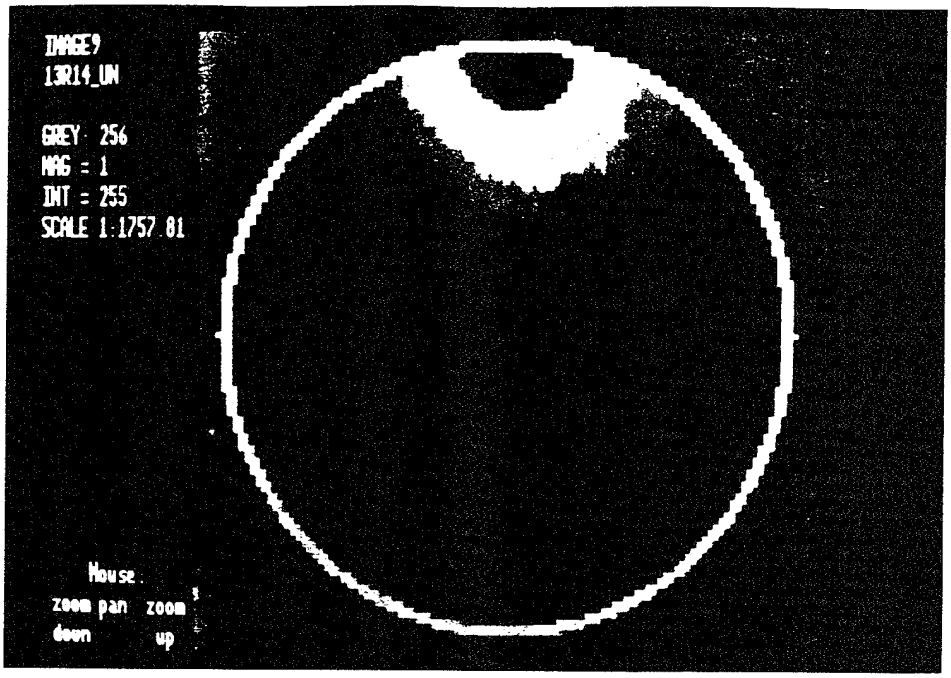

Figure 43 Interferometric Fringes. Hologram 14.

was not recorded because the crack propagated and the specimen failed during its exposure. The specimen was loaded beyond the range of the displacement contorl transducers under constant rate of load point displacement (stroke) in order to determine the final failure mode. The observed failure sequence is shown in Figure 46. A very similar failure sequence at high strain rates have been reported by Tedesco et al. (Reference 24)

F. CONCLUSIONS

1. Laser holographic interferometry can be used to measure three dimensional displacement fields under closed loop testing conditions.
2. A mechanical arrangement was developed to produce stable crack growth in disk specimens (Brazilian Test).
3. Image processing can be effectively used for elimination of rigid body motion from holographic recordings resulting in well defined and accurate fringe orders.

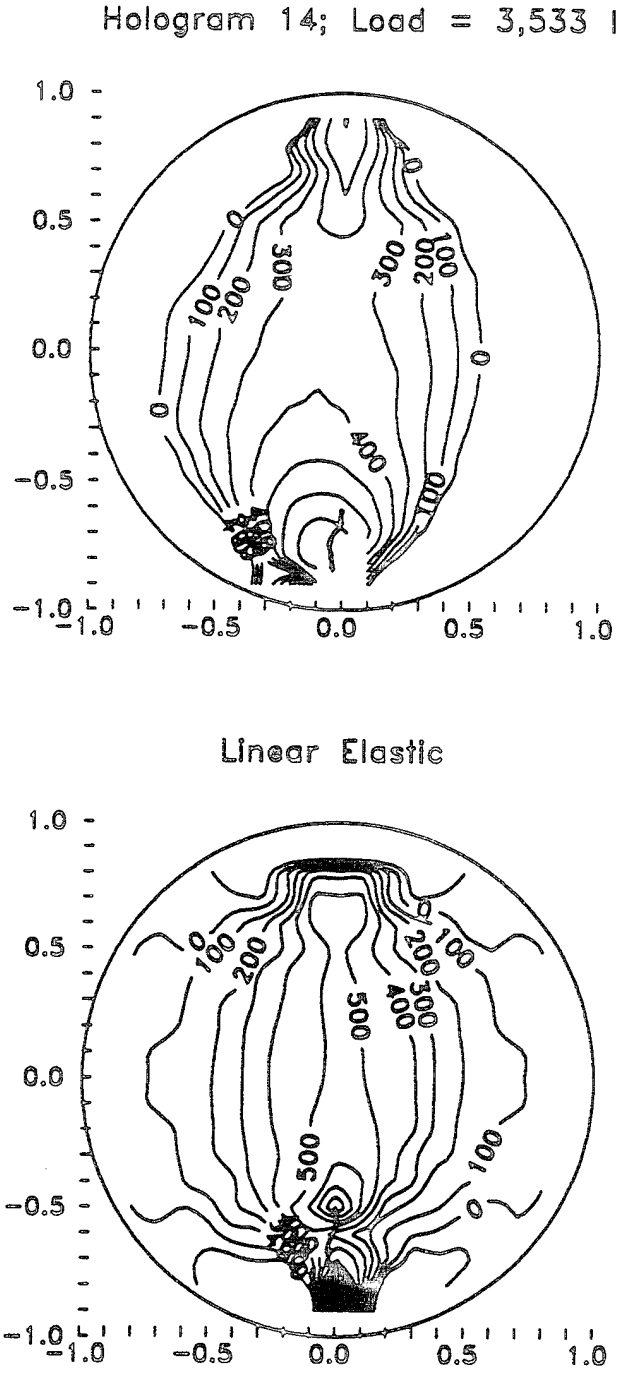

Figure 44 Strain Fields. Hologram 14; Load = 3,533 lb

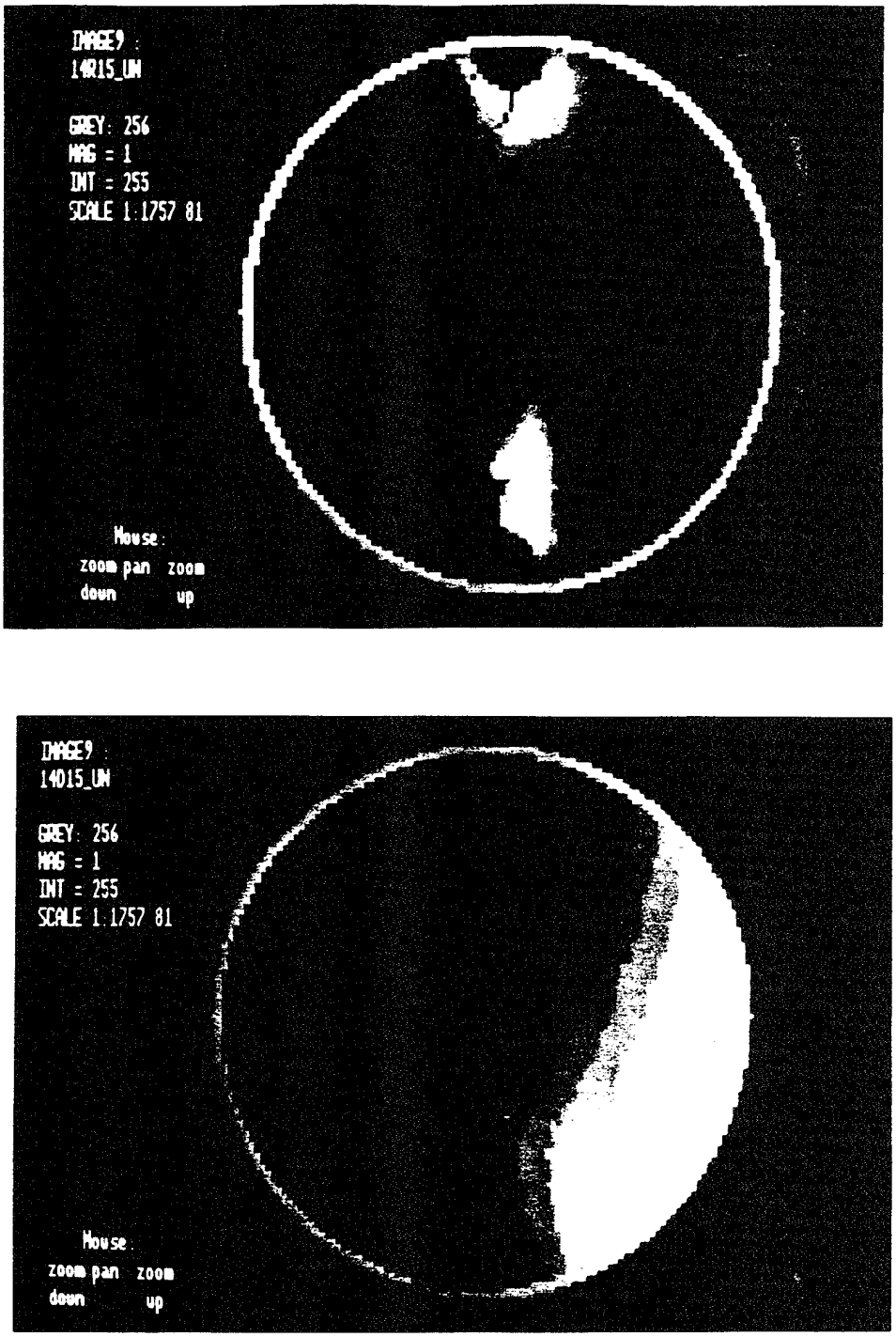

Figure 45 Holographic Interferograms at Failure State.

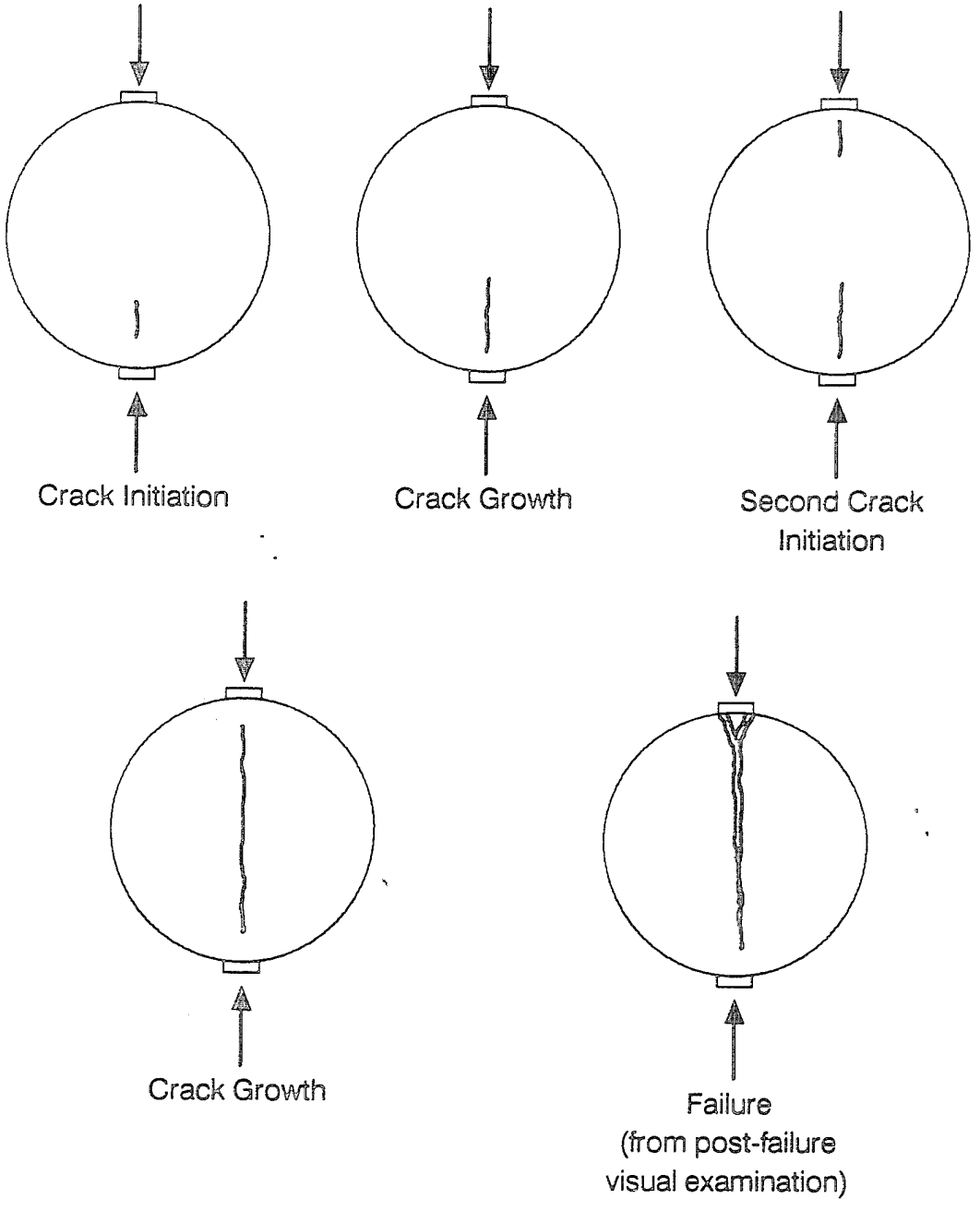

Figure 46 Observed Failure Sequence.

4. Examination of the strain distribution measured at early low stages can give indication of the crack initiation location.
5. Crack initiation occurs at approximately 70 percent of the failure load.
6. Tensile strain levels before cracking are significantly higher than those found under uniaxial stress conditions.
7. Even though the Brazilian Test was developed and has been useful to determine the tensile strength in concrete, failure does not start in the region of uniform tensile stress. Thus, the relationship between tensile strength and the applied load may differ from that proposed by Carneiro.
8. From the experimental observations, it is clear that stable crack propagation has an important role in the determination of the structural response.
9. Crack initiation location may be one of the reasons why the post peak part of the load-deformation diagram is difficult to reach. The effect of crack opening on the diametral displacement is very small at the initial stages of crack propagation.
10. The reported wedge formation in the Brazilian Test configuration constitutes a secondary failure mode and occurs after a single crack has propagated through the diameter of the specimen and a significant loss of strength has taken place. The above is true for the specimen size used during this investigation. A change of failure sequence may occur for larger specimens (Reference 25)

SECTION IV

STRAIN FIELDS IN MIXED MODE FRACTURE PROCESS ZONE

A. INTRODUCTION

Linear elastic fracture mechanics has been used to model quasi-brittle behavior of cement-based materials. Indirect methods such as the multicutting technique (Reference 26) and experimental observations using acoustic emission (Reference 27) and holographic interferometry (Reference 28) have demonstrated that there is transfer of tensile stress between the crack faces. Cohesive crack models that simulate the stress transfer across the crack and otherwise conventional linear elastic fracture mechanics have been used to simulate Mode I cracking (References 29, 7, 8 and 30).

Since Mode I tests can be conducted easily in laboratories compared to other modes, cohesive crack models and several other methods have been proposed to characterize Mode I crack propagation in concrete (References 31, 32 and 33). However, many structural applications involve a mixed-mode loading condition. It is necessary to see if an extension of the Mode I model can be applied in the case where both tensile and shear forces associated with crack opening and sliding are transmitted trough the crack faces. The study presented in this section was intended to measure the strain distribution in the fracture process zone in mixed mode specimens in order to provide the information required to develop a cohesive crack model similar to those for Mode I.

B. EXPERIMENTAL PROGRAM

Specimens similar to the disk specimen used in the study discussed in Section III were used. A 0.4 inch notch was cast longitudinally at the center of the specimens as shown in Figure 47. Three center-notched disk specimens (CNDS) were cast at the same time the unnotched disk specimen for the Brazilian test were made. A summary of the material properties is shown in Table 1.

TABLE 3 HOLOGRAPHIC RECORDINGS. SPECIMEN HOLO-00-8 NOTCH INCLINATION ANGLE B=0°

Holographic Recording	Time	Load	
	s	lb	N
P (Preload)	350	368	1,656
1	2,500	633	2,849
2	3,000	751	3,380
2*	5,000	670	3,015
2**	7,000	618	2,781
3	8,024	927	4,172
4	8,900	1,148	5,166
4*	10,400	1,100	4,950
4**	12,000	1,075	4,838
5	14,000	1,457	6,557
6	15,500	1,722	7,749
7	17,290	2,105	9,473
8	18,761	2,326	10,467
9	19,100	2,355	10,598
10	19,450	2,429	10,931
11	20,000	2,400	10,800
12	20,500	2,340	10,530

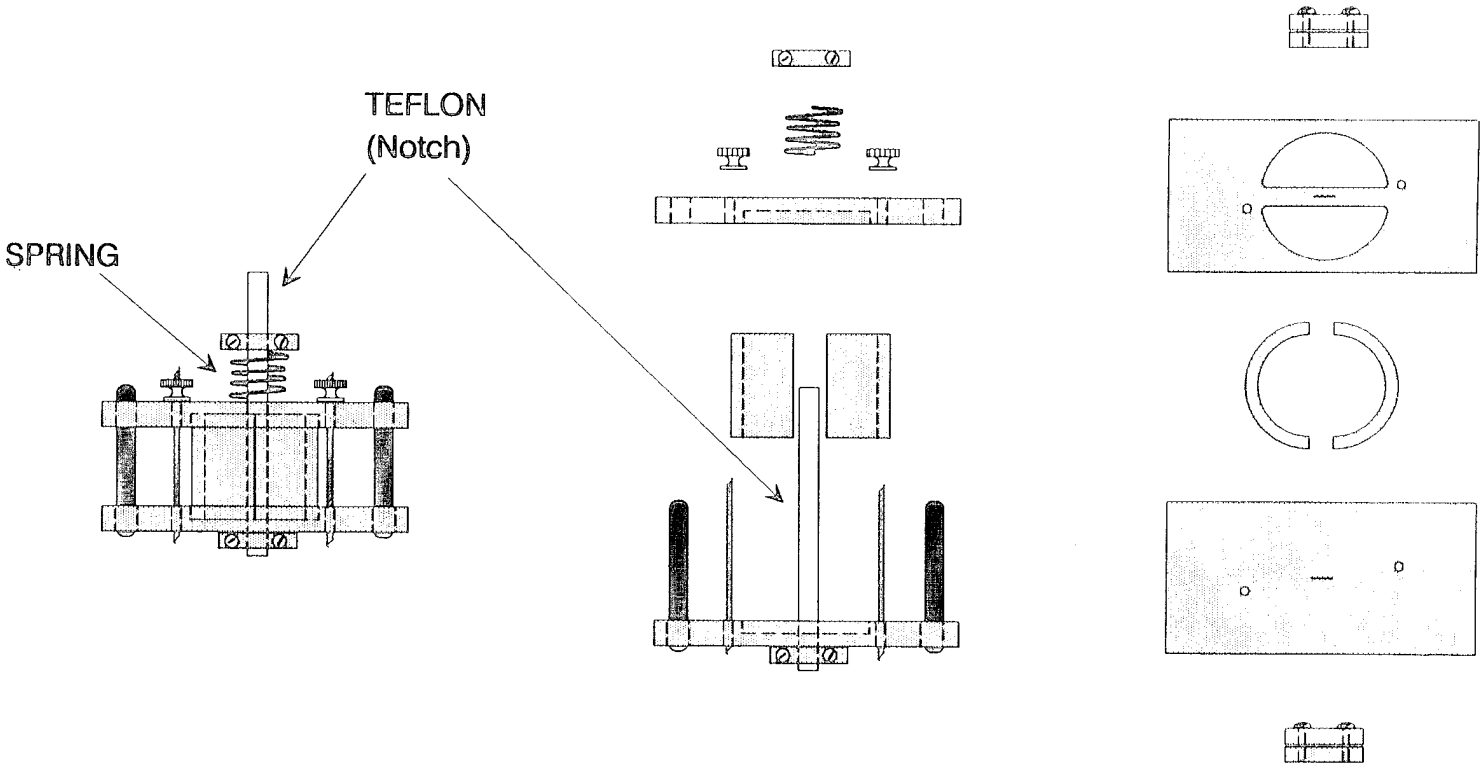

Figure 47 Mold for Center Notched Disk Specimens (CNDS)

Figure 48 (Reference 34) shows how by rotating the notch inclination angle (β) with respect to the loading direction, it is possible to change the mode of fracture from tensile (Mode I for $\beta = 0°$) to mixed mode (Tension-Shear for $\beta < 30°$ and Compression-Shear for $\beta > 30°$).

Both the mechanical arrangement and the holographic setup used are identical to those described in Section III. Diametral displacement was measured as opposed to the crack opening displacement, to preserve symmetry. Preliminary tests indicated that the opening force induced by standard clip gages is enough to produce asymmetric cracking.

Specimens were tested at five different inclination angles (0°, 18°, 36°, 54° and 72°), but it was not possible to make holographic recordings for β = 36° during crack propagation due to the brittleness of the response. The following two sections discuss the results corresponding to notch inclination angles β = 0° and β = 54°. In all cases, the loading process was continued after the first crack propagated throughout the specimen, up to the limit of the instrumentation used for close loop control, but collapse of the specimens was not reached.

After the deformation control transducers were out of range, the specimens were loaded under stroke control, up to collapse, to obtain the final failure mode as reported in Figure 49.

C. STRAIN FIELDS (B = 0°)

Figure 50 shows the load vs. diametral displacement curve. In this plot, the stars correspond to the holographic recordings as shown in Table 3. The initial part of the curve is not reliable because it was affected by the vibrations and air currents induced at the start of the test. This was reflected in the low quality of the holographic recordings obtained at this load levels. As shown in Table 3, Holograms 2 and 4 had to be repeated until the desired quality was obtained.

The shape of this curve is similar to that reported by Ojdrovic and Petroski (Reference 35) for notch-length/diameter ratio of 0.3. Stable crack growth occurs

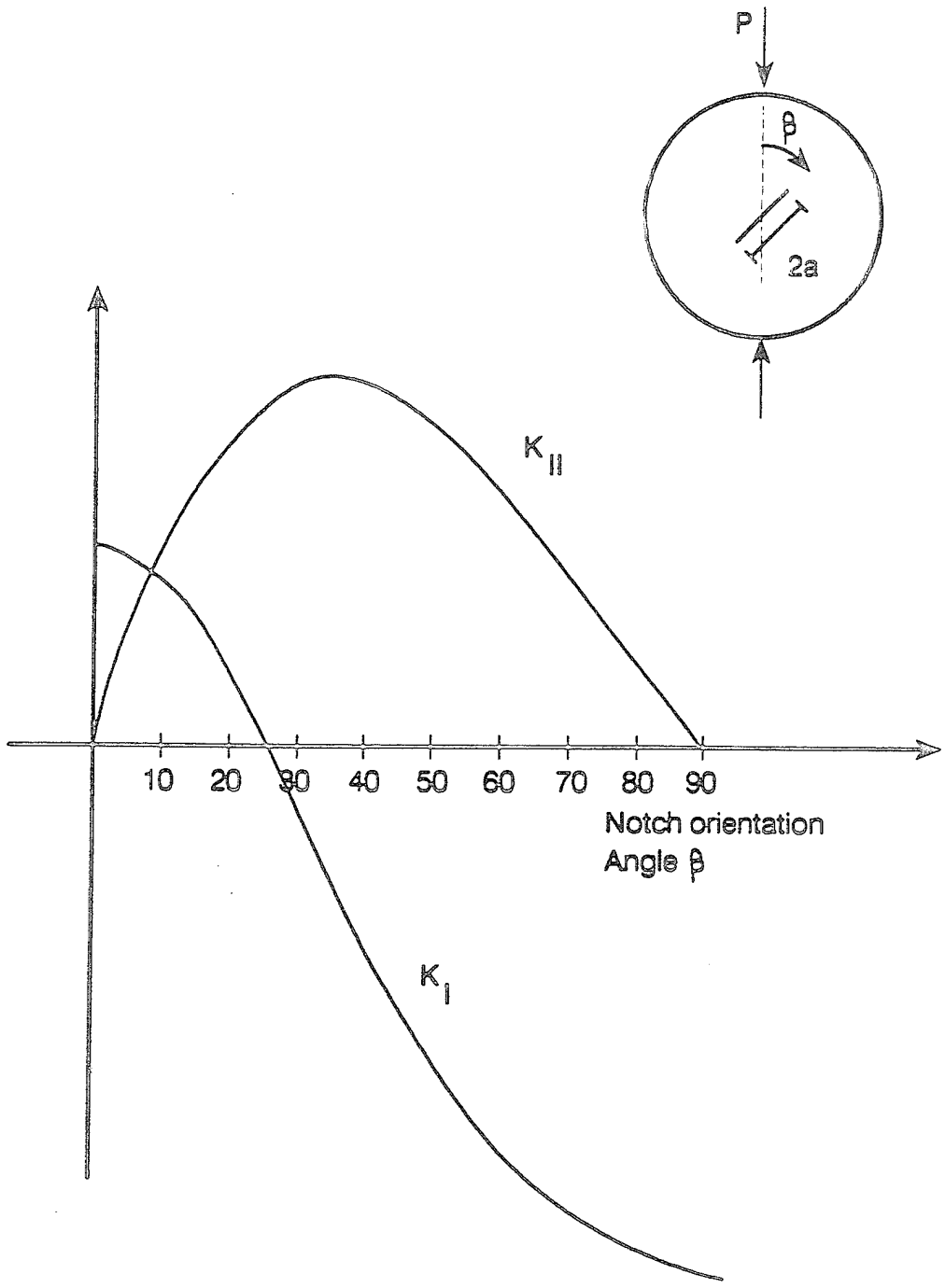

Figure 48 Variation of Stress Intensity Factors for CNDS.

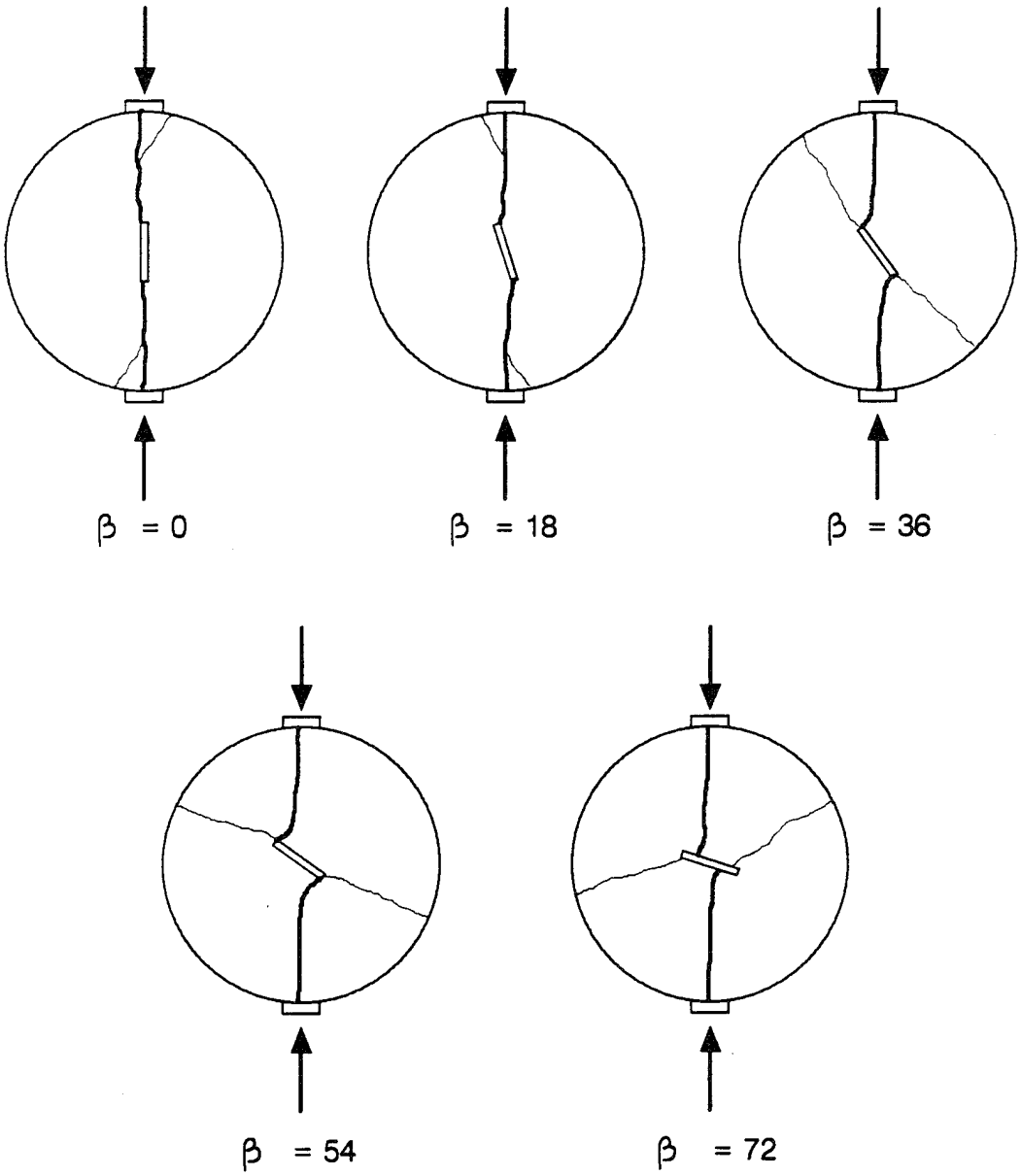

Figure 49 Initial and Final Failure Modes for Various Inclination Angles

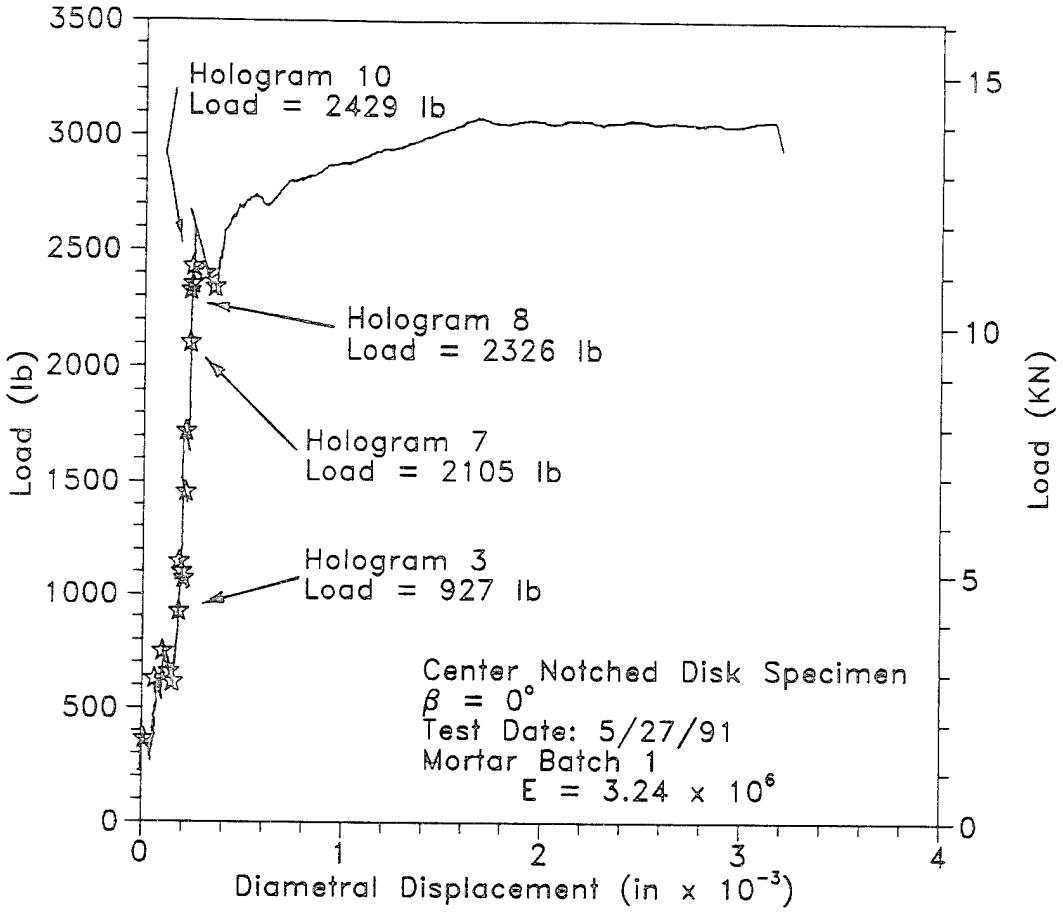

Figure 50 Load vs. Diametral Displacement Curve. $\beta = 0°$

between Holograms 7 and 10 (2105 pounds and 2429 pounds respectively) even though there is no macroscopic evidence of nonlinearity. After Hologram 10, the first crack propagated through the specimen and the nonlinear response is significant. Further increase of the load after this point is possible. A maximum load of 3,040 pounds was reached. After the loading sequence was completed, a second set of cracks starting

from the perimeter of the cylinder have formed, initiating the wedge formation reported by Ojdrovic.

Figures 51 to 58 show the interferometric fringes and corresponding strain fields

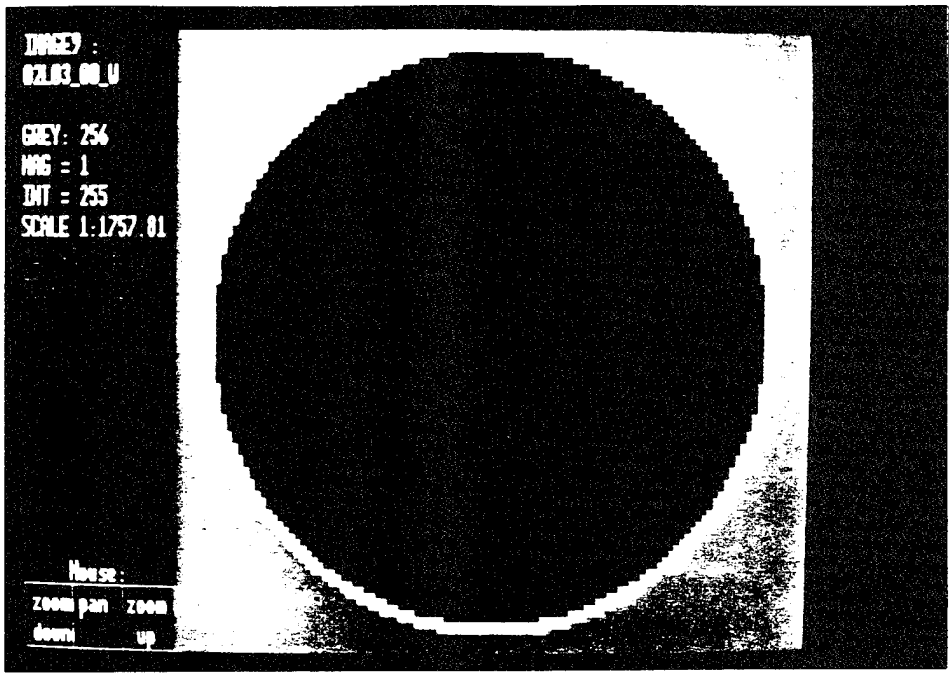

Figure 51 Interferometric Fringes. Hologram 3

for four stages of the loading process. Figure 52 shows the strain distribution during the elastic range. Although there are variations with respect to the linear elastic solution, there is indication of strain concentration in the region surrounding the notch tips. Figure 54.

corresponds to crack initiation. At this load level, the crack initiated from the bottom notch tip. The strain distribution is similar around top and bottom notch tips because the crack is very short (less than 0.1 inch) and crack initiation at the top notch tip is just about to occur. The zones of strain concentration are wider and the strain increase is lower compared to the linear elastic solution. The linear elastic solution was obtained by propagating a crack in the finite element mesh using the crack trajectory obtained from the holographic recordings. The same observation can be made during stable crack

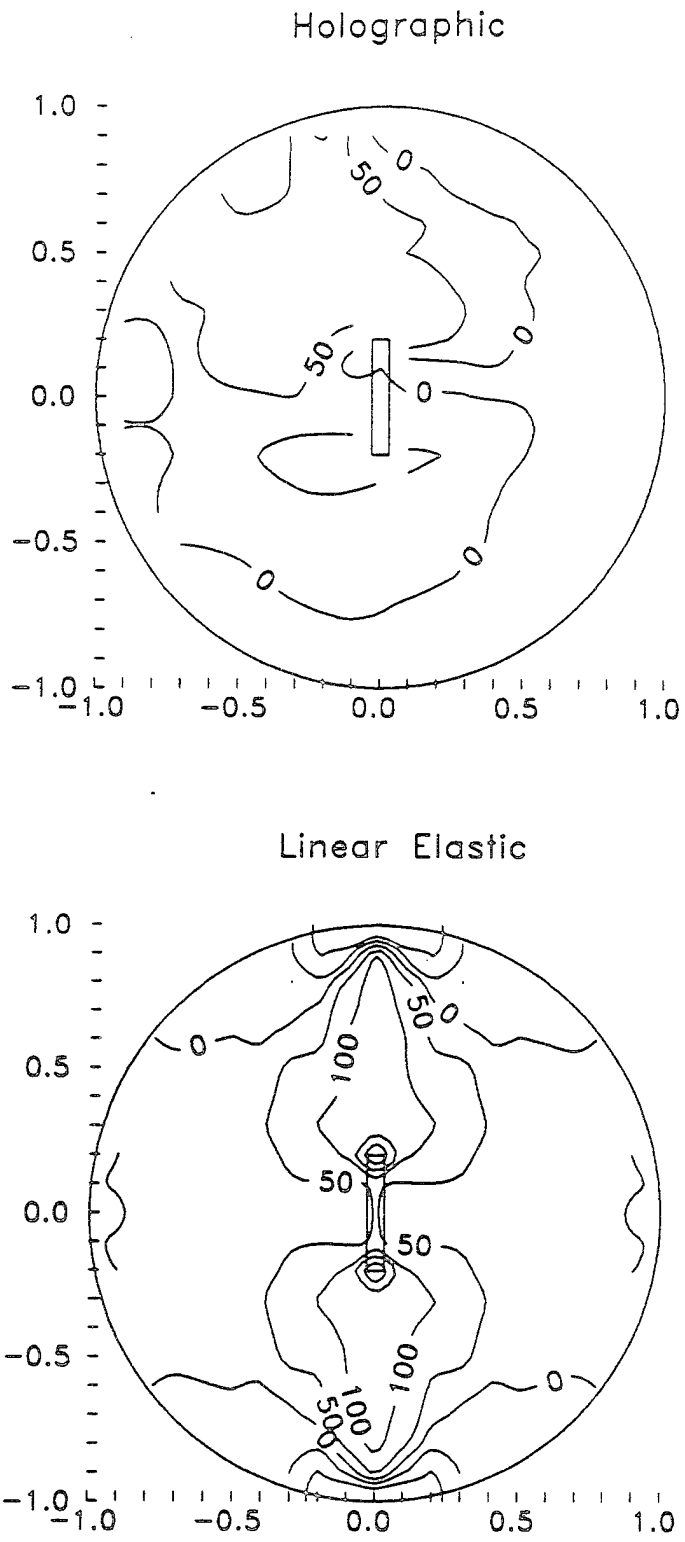

Figure 52 Strain Fields (ϵ_{xx}). β = 0°, Hologram 3, Load = 927 lb. Elastic Range

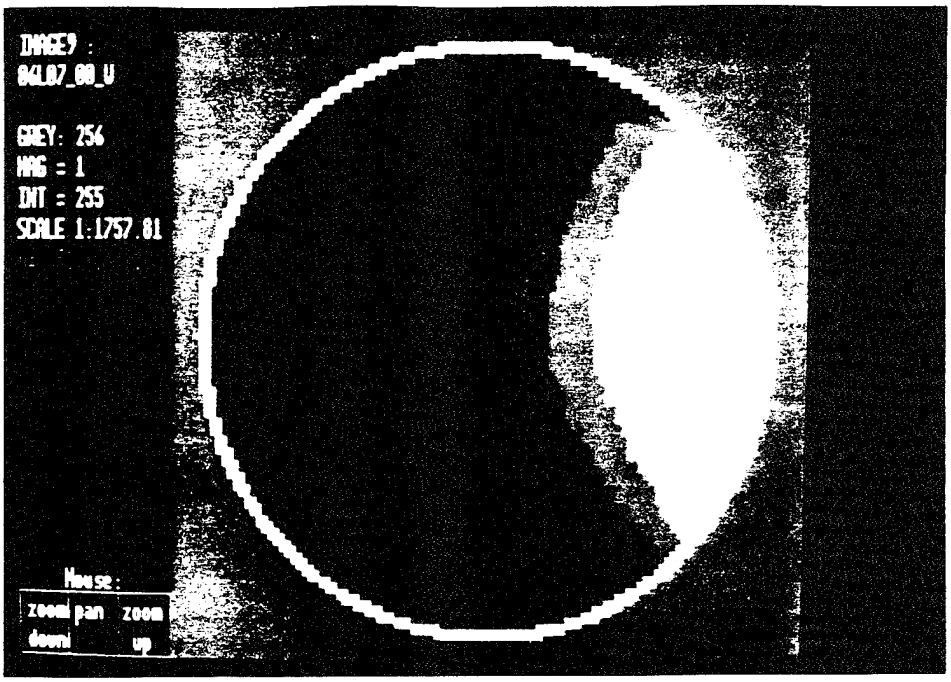

Figure 53 Interferometric Fringes. Hologram 7.

propagation and failure stages illustrated in Figures 56 and 58. Also, in these figures it is apparent that the strain relaxation behind the crack tip is complete for the linear elastic solution whereas the experimental strain values do not immediately reach zero.

D. STRAIN FIELDS (B=54°)

The load vs. diametral displacement is shown in Figure 59. A summary of the holographic recordings is in Table 4.

The descending part of the load-deformation plot immediately after unstable crack propagation indicates a reduction of the ductility as compared to the previous case. Stable crack growth was still possible and occurs between Holograms 8 and 12 (1560 pounds and 2120 pounds respectively). A maximum load of 2,307 pounds was reached. Signs of secondary cracking were found after the completion of the experiment.

Strain distribution and interference fringes for four load levels are shown in Figures 60 to 67. In general, similar conclusions as those from the previous specimens can be

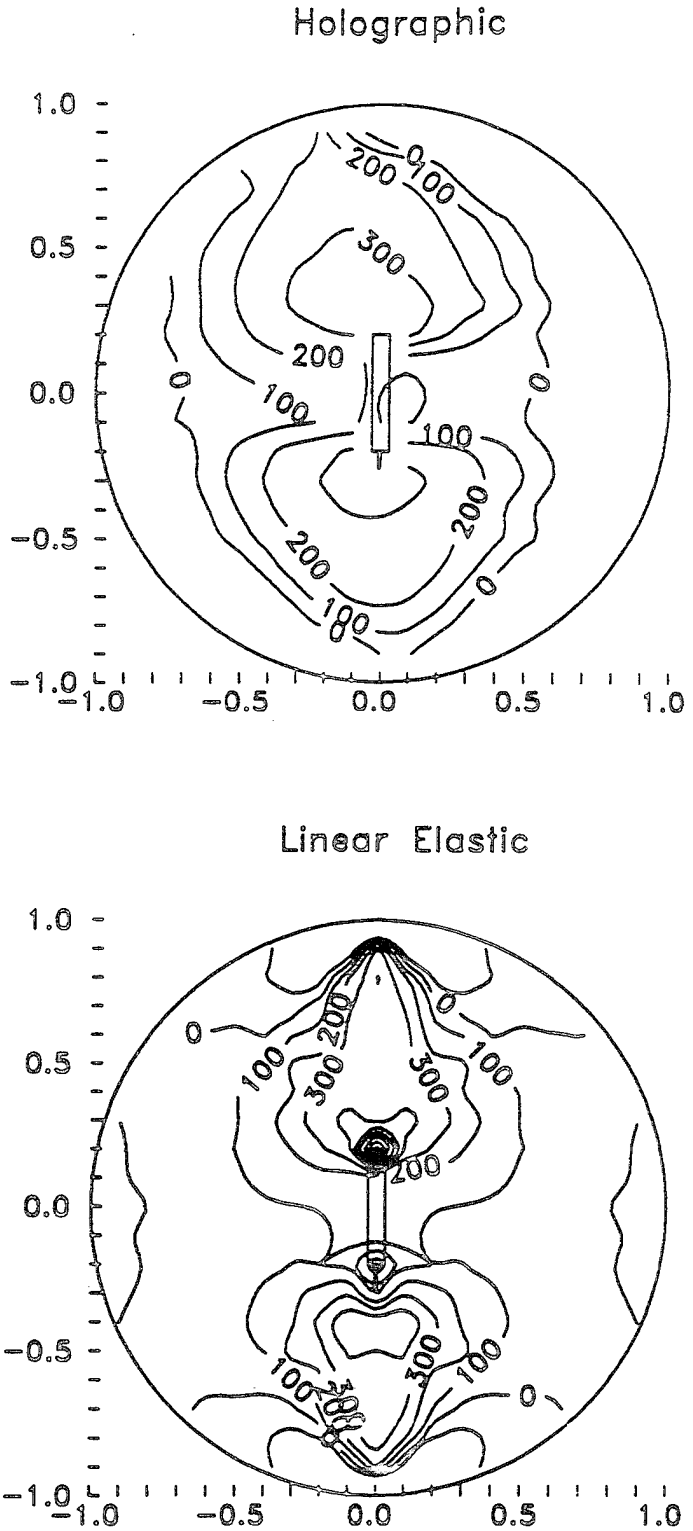

Figure 54 Strain Fields (ϵ_{xx}). β = 0°, Hologram 7, Load = 2,105 lb. Crack Initiation.

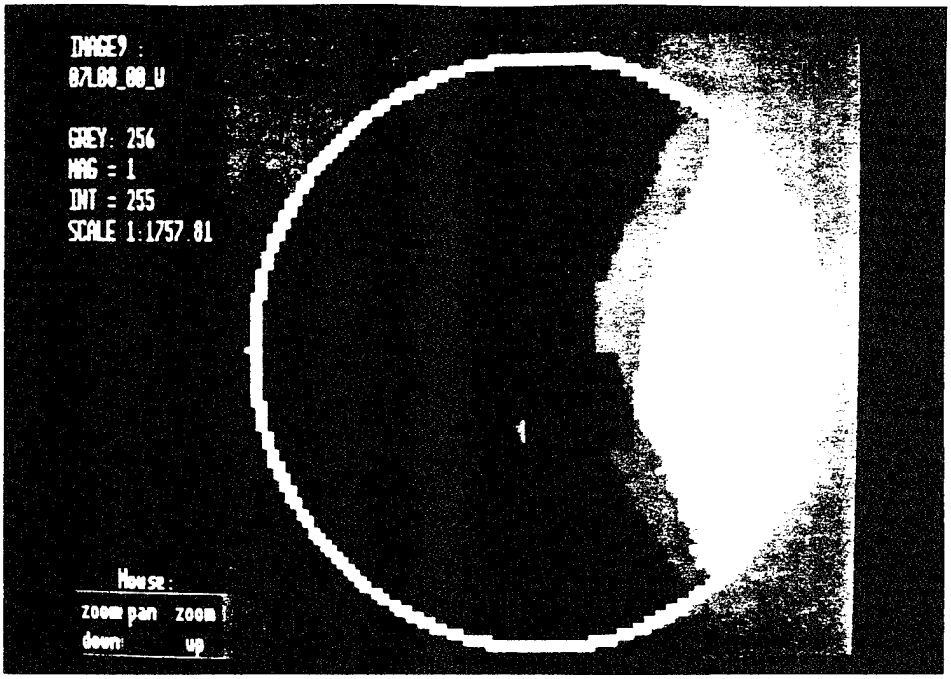

Figure 55 Interferometric Fringes. Hologram 8.

made regarding the strain distributions relative to the crack tip location. Also, note that even at low load levels, the strain level is higher on the top half of the specimen, which can be related to the mode of failure. The cracks initiated at the same time at both notch tips and initially, the bottom crack propagates slightly. Then, the top crack propagates up to failure.

E. FRACTURE PROCESS ZONE

A similar approach to that presented in Section II was used to enclose the FPZ, defined as the zone of deviation from linearity exceeding 60 $\mu\epsilon$. Figure 68 contains the difference in strain field between the linear elastic and the holographic solutions for notch inclination angle β = 0°. Before crack propagation, the FPZ is larger on the bottom of the specimen which corresponds to the direction of maximum crack propagation at latter loading stages. The width of the fracture process zone remains approximately constant. Unfortunately, the specimen size makes unclear whether or not the FPZ grows with crack

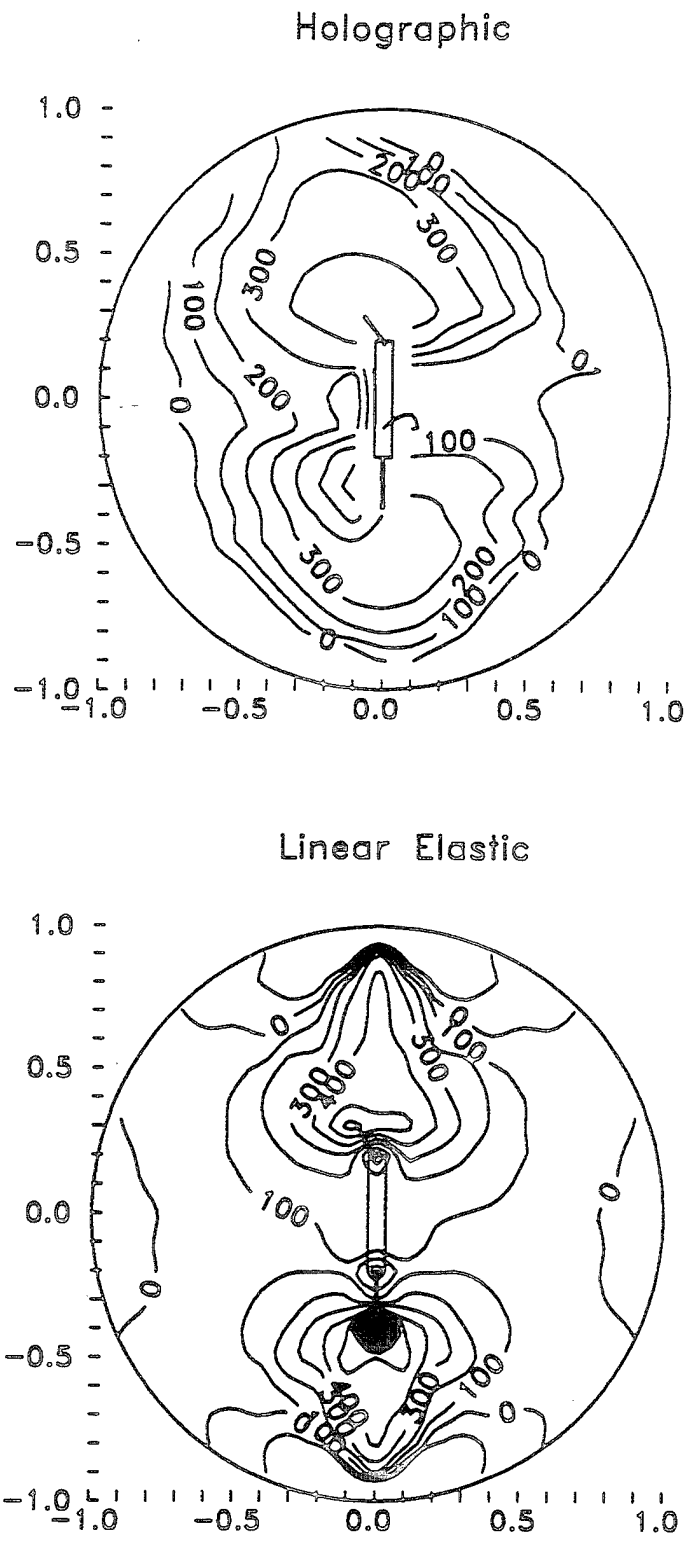

Figure 56 Strain Fields (ϵ_{xx}). β = 0°, Hologram 8, Load = 2,396 lb. Stable Crack Propagation

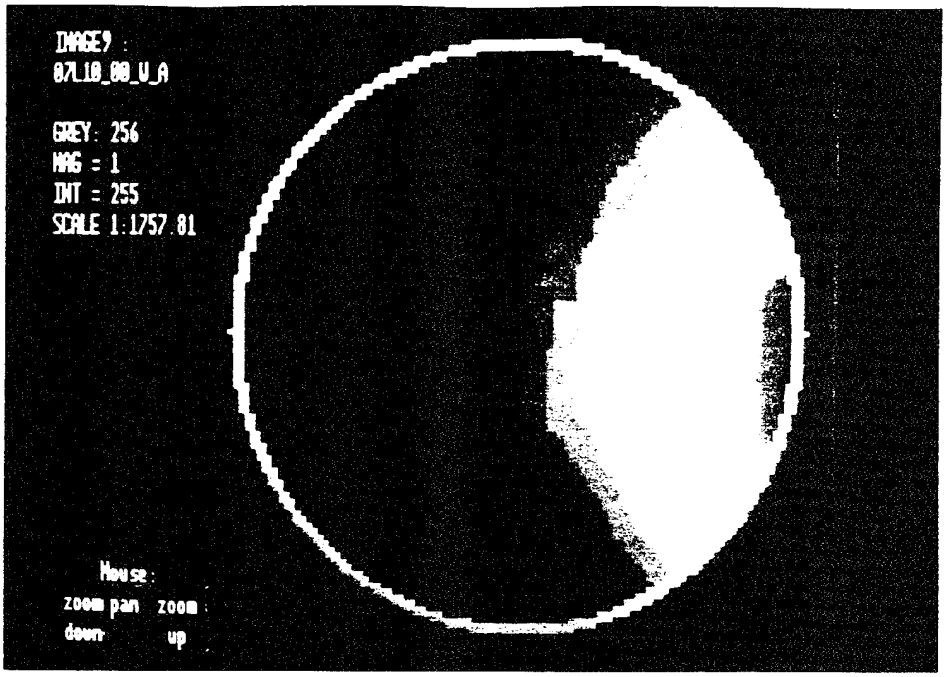

Figure 57 Interferometric Fringes. Hologram 10.

length. Zones B in Figure 68 correspond to the so-called wake of the fracture process zone (WFPZ) and are attributed to stress transfer between the crack faced behind the crack tip. Zones B do not appear until the bottom crack has propagated 0.2 inches from the notch tip which correlates well with the model proposed by Cook, et al. (Reference 29).

If the same definition based on difference in tensile strain is used, the FPZ for 54° notch inclination (Figure 69) is smaller than those obtained for tension cracks (β = 0° and plate specimen studied in Section II) for short crack lengths. For longer crack lengths (after 2120 pounds of applied load), when the crack stopped curving and has adopted a straight line trajectory, both the FPZ and WFPZ grow to similar dimensions.

The apparent LEFM stress intensity factors (Figure 70) calculated by Equation (8)

$$K = \left[K_I^2 + K_{II}^2 \right]^{1/2} \quad (8)$$

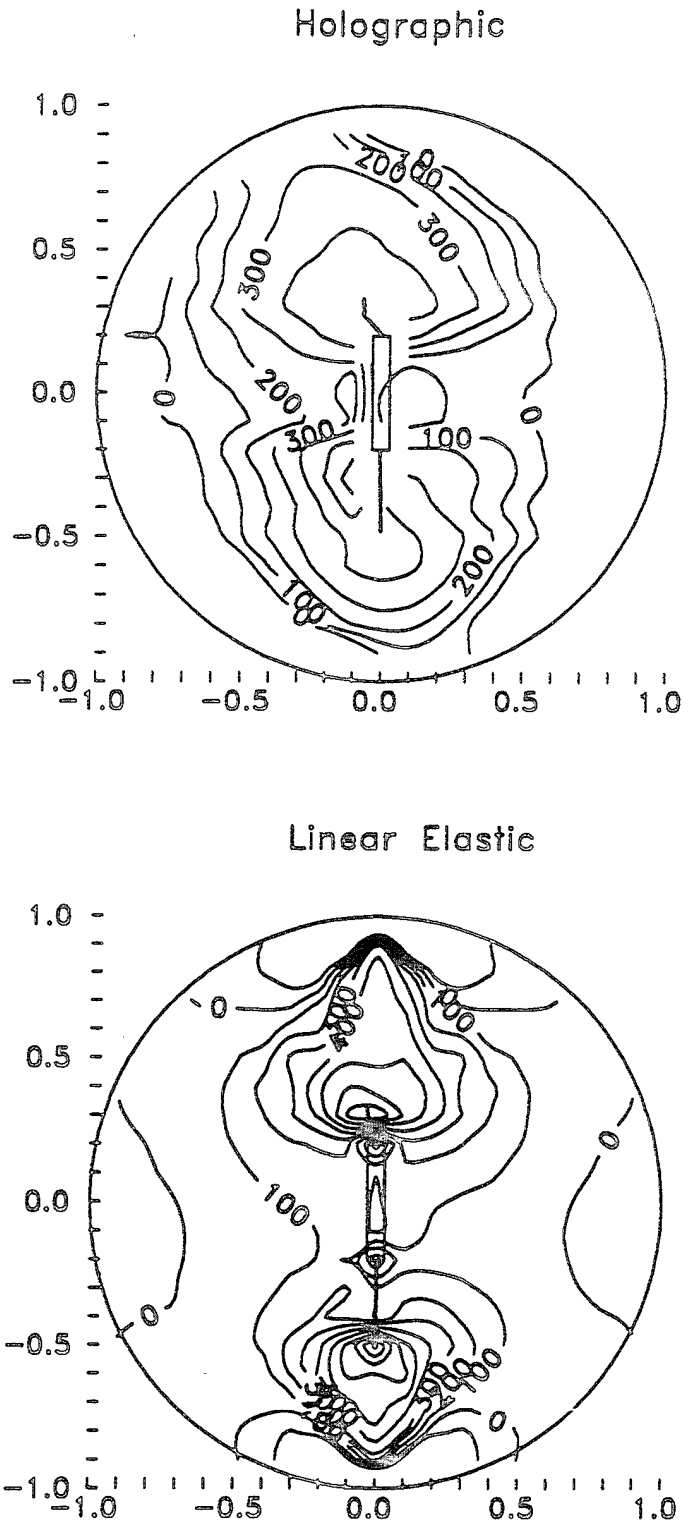

Figure 58 Strain Fields (ϵ_{xx}). β = 0°, Hologram 10, Load = 2,429 lb Failure

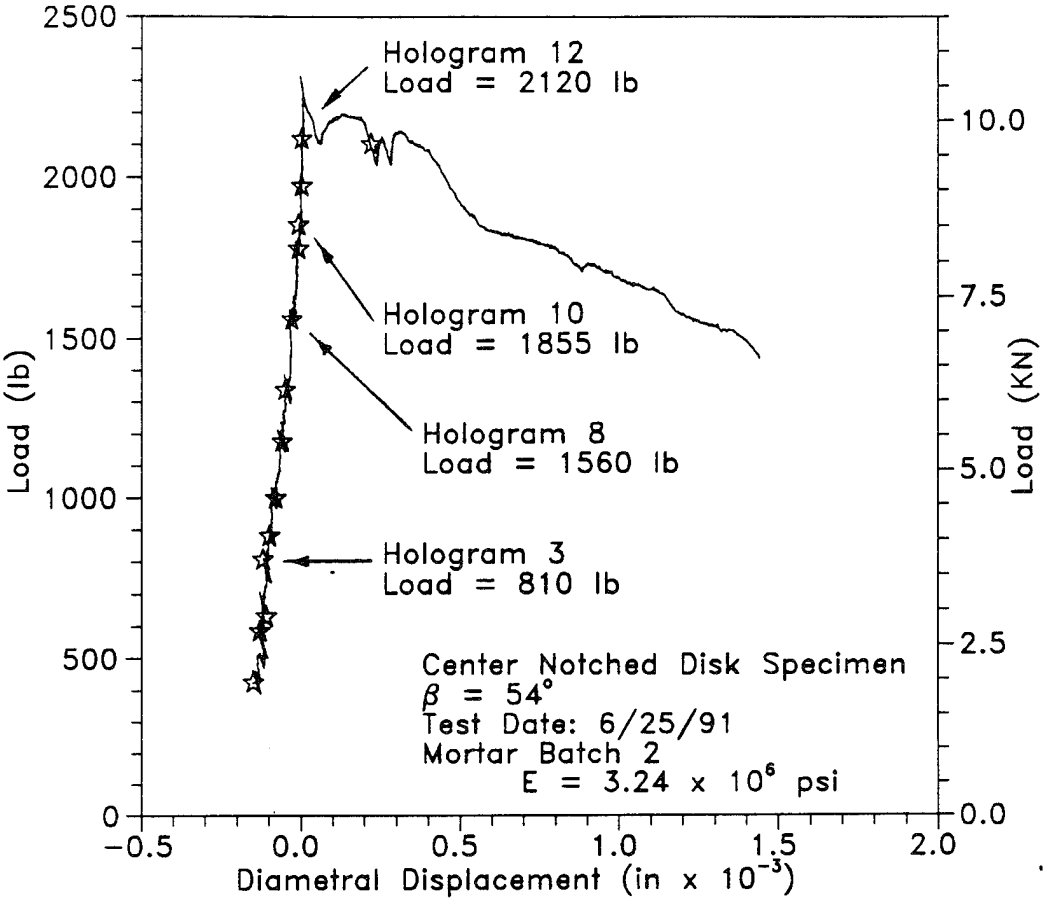

Figure 59 Load vs. Diametral Displacement Curve. β = 54°

as proposed by Jenq (Reference 36) follow an R-curve type of behavior. However, it has been shown in Section II that a cohesive crack model can be used to simulate the stress transfer between crack faces which may results in a constant (or rather a narrow band) of values for the stress intensity factor (Reference 37). Thus, a constant fracture toughness (K_c) can be used to predict crack propagation. The development of a cohesive crack model for mixed mode cracking is not simple because the complex

TABLE 4 HOLOGRAPHIC RECORDINGS. SPECIMEN HOLO-54-0 NOTCH INCLINATION ANGLE B = 54°

Holographic Recording	Time	Load	
	s	lb	N
P (Preload)	0	426	1,917
1	2,800	589	2,651
2	3,500	633	2,849
3	5,000	810	3,645
4	6,600	883	3,974
5	8,100	1,001	4,505
6	10,000	1,178	5,301
7	11,500	1,354	6,093
8	13,000	1,560	7,020
9	14,700	1,780	8,010
10	15,200	1,855	8,348
11	15,600	1,972	8,874
12	16,100	2,120	9,540
13	16,700	2,105	9,473

coupling existing between normal and shear forces and opening and sliding displacements along the crack faces (References 38, 39 and 40).

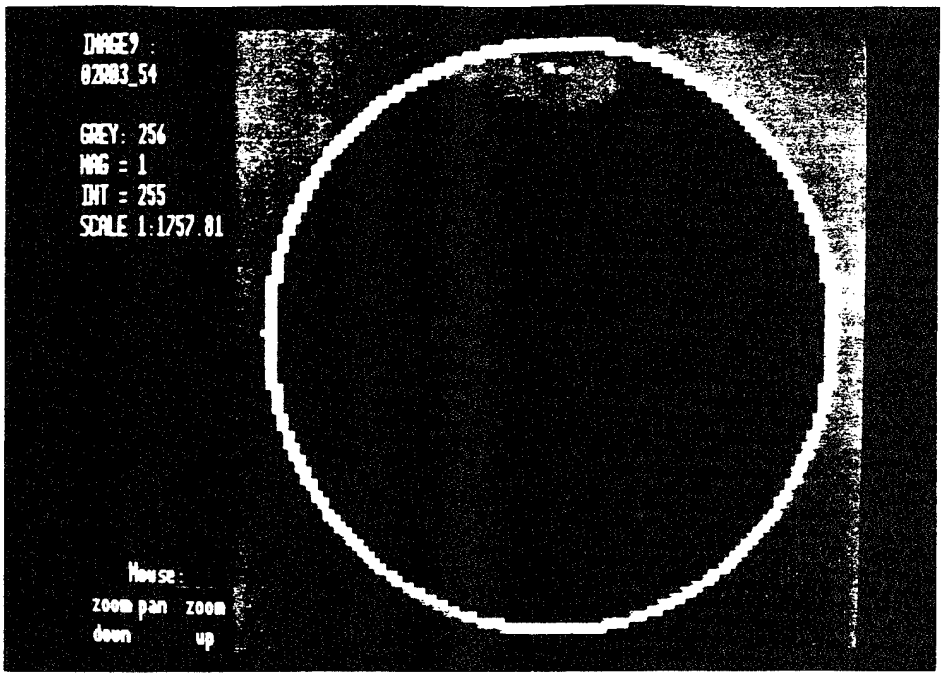

Figure 60 Holographic Interferogram. Hologram 3.

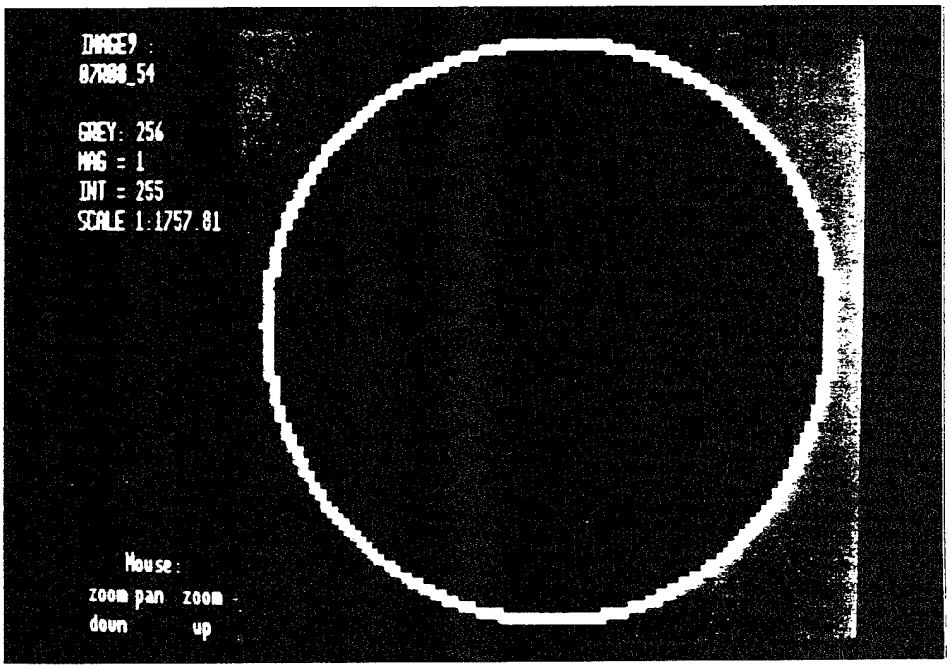

Figure 61 Holographic Interferogram. Hologram 8.

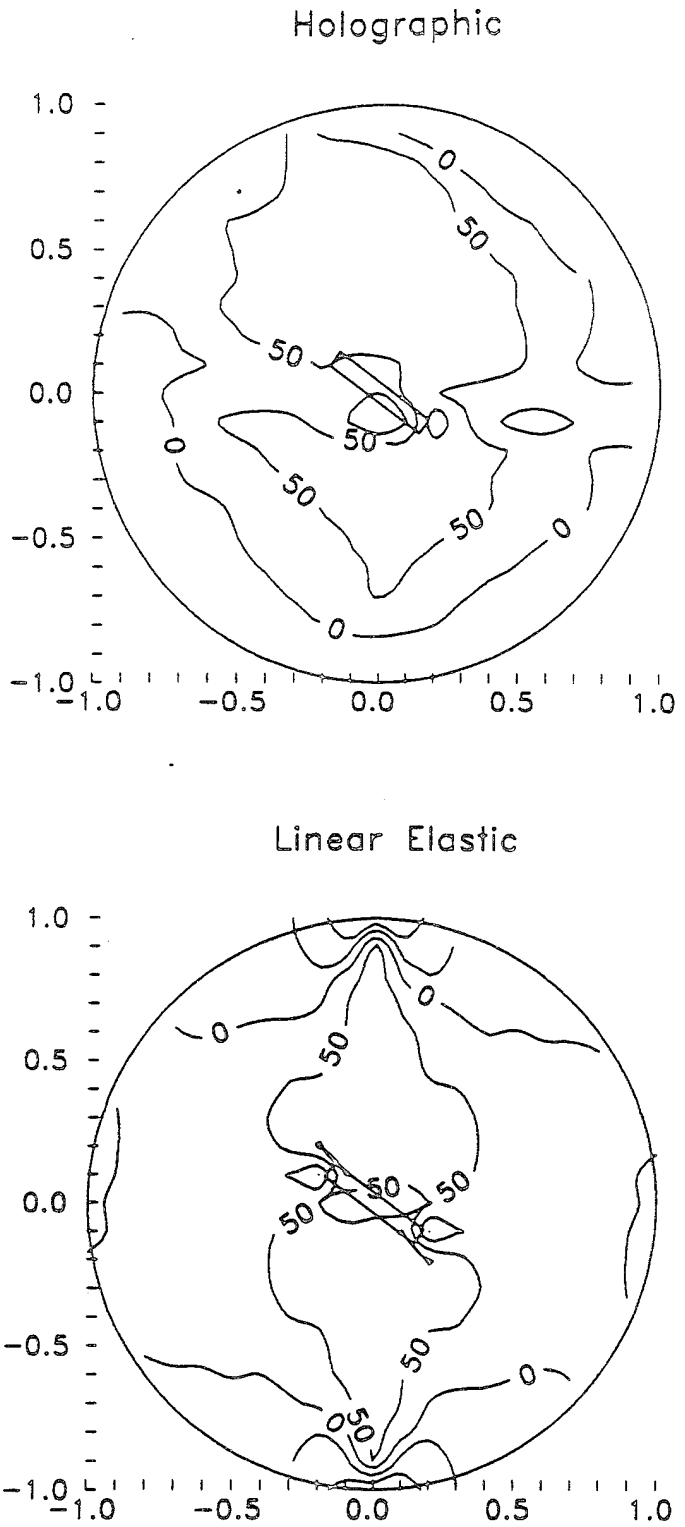

Figure 62 Strain Fields (ϵ_{xx}). β = 54°, Hologram 3, Load = 810 lb Elastic Range

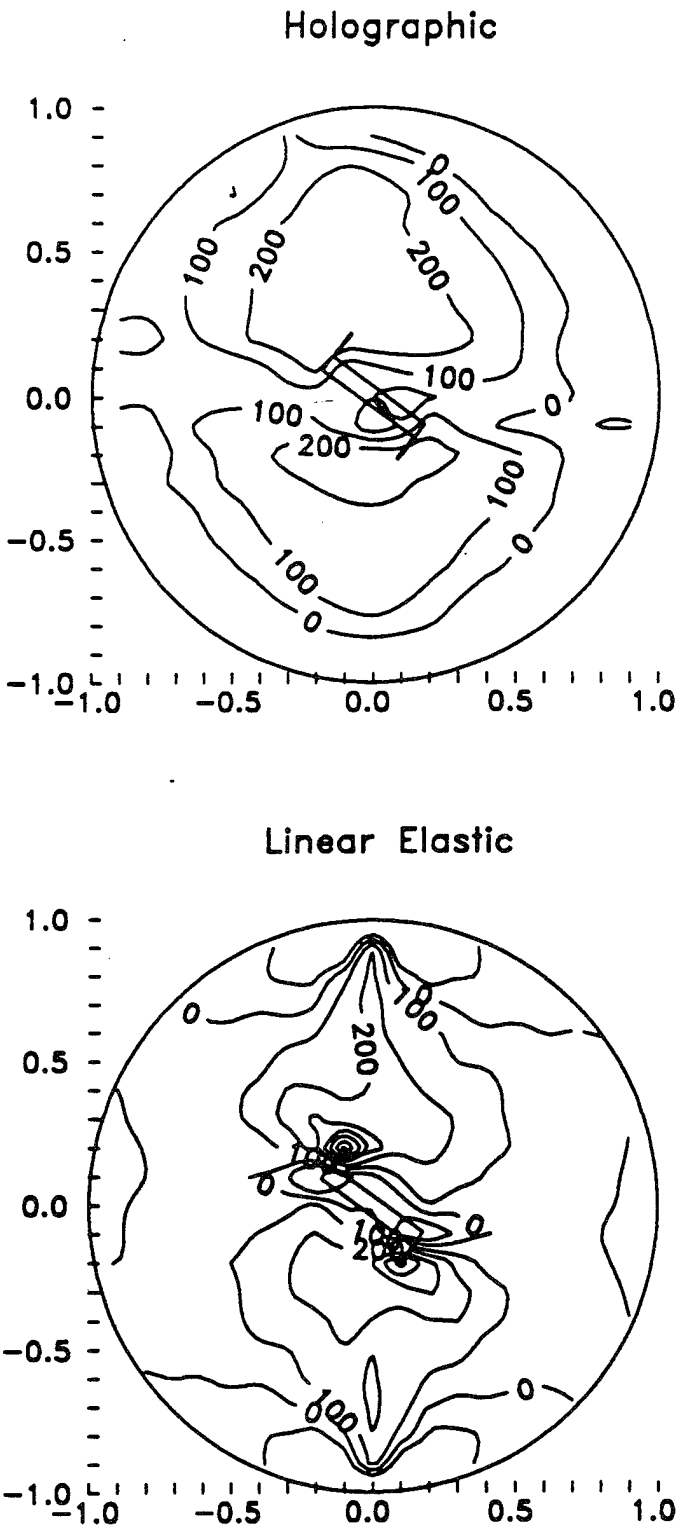

Figure 63 Strain Fields (ϵ_{xx}). β = 54°, Hologram 8; Load = 1,560 lb Crack Initiation

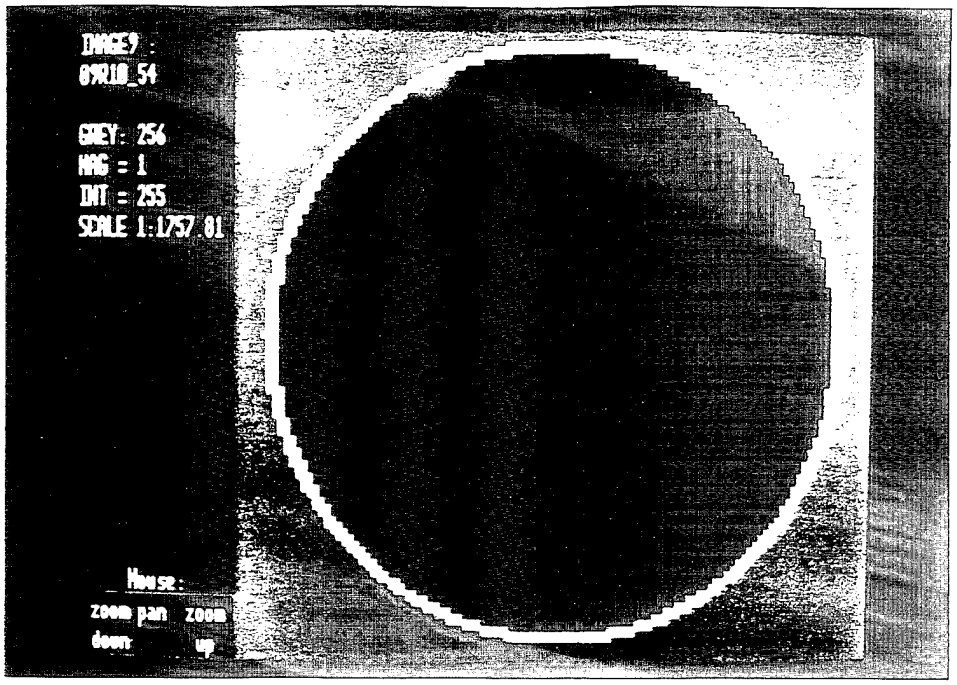

Figure 64 Interferometric Fringes. Hologram 10.

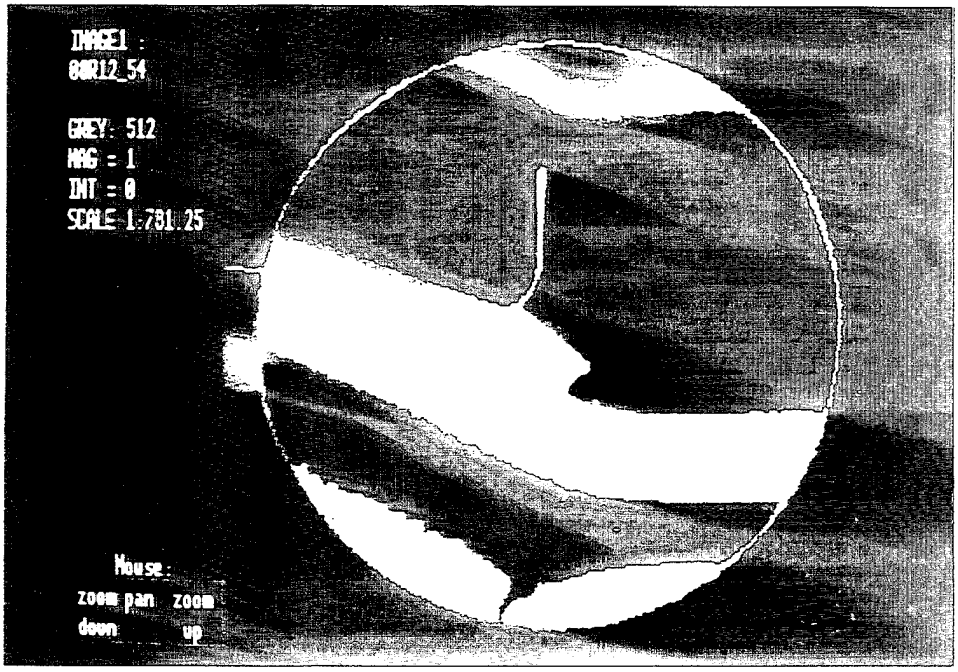

Figure 65 Interferometric Fringes. Hologram 12.

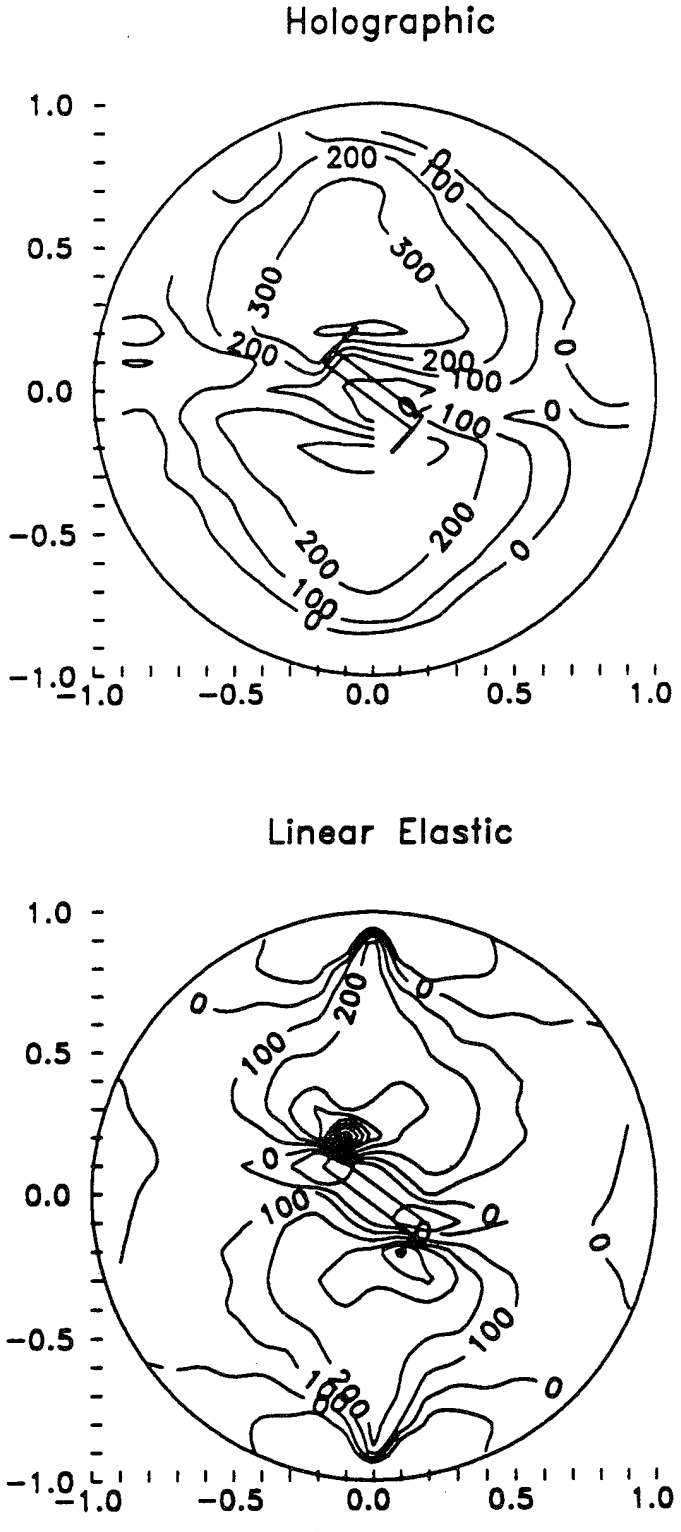

Figure 66 Strain Fields (ϵ_{xx}). β = 54°, Hologram 10, Load = 1,855 lb
Stable Crack Propagation

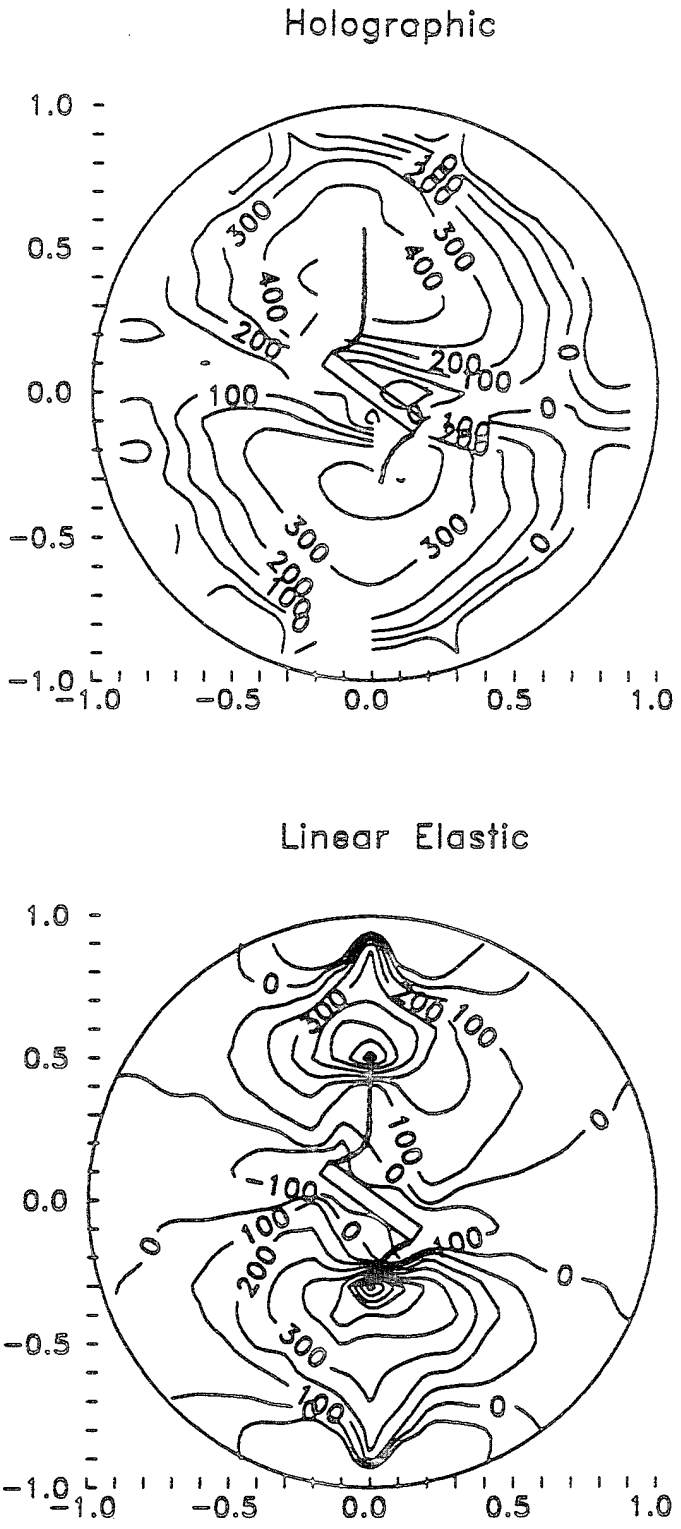

Figure 67 Strain Fields (ϵ_{xx}). β = 54°, Hologram 12, Load = 2,120 lb Failure

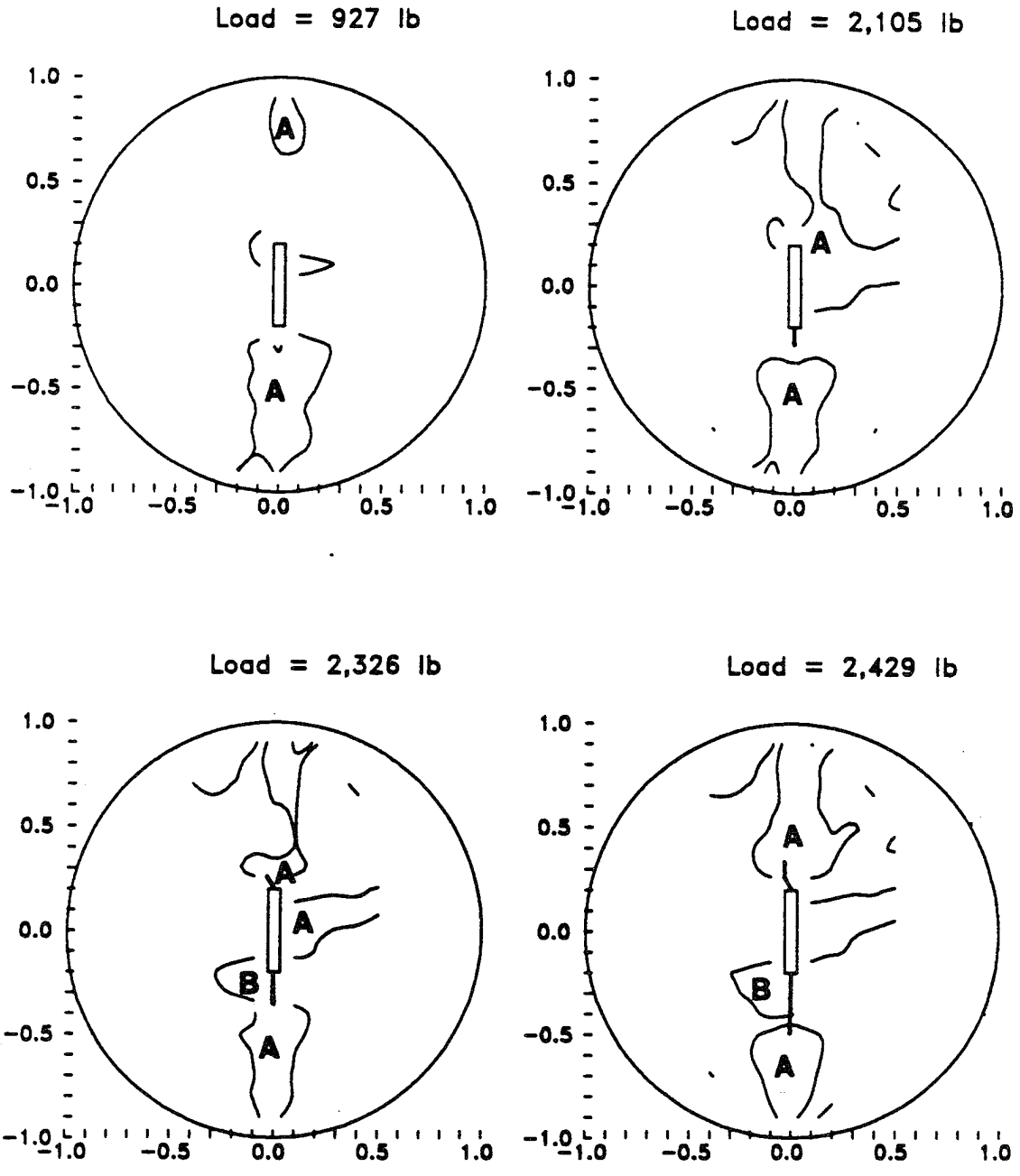

Figure 68 Difference Between Holographic and Linear Elastic Strain Fields. β = 0°

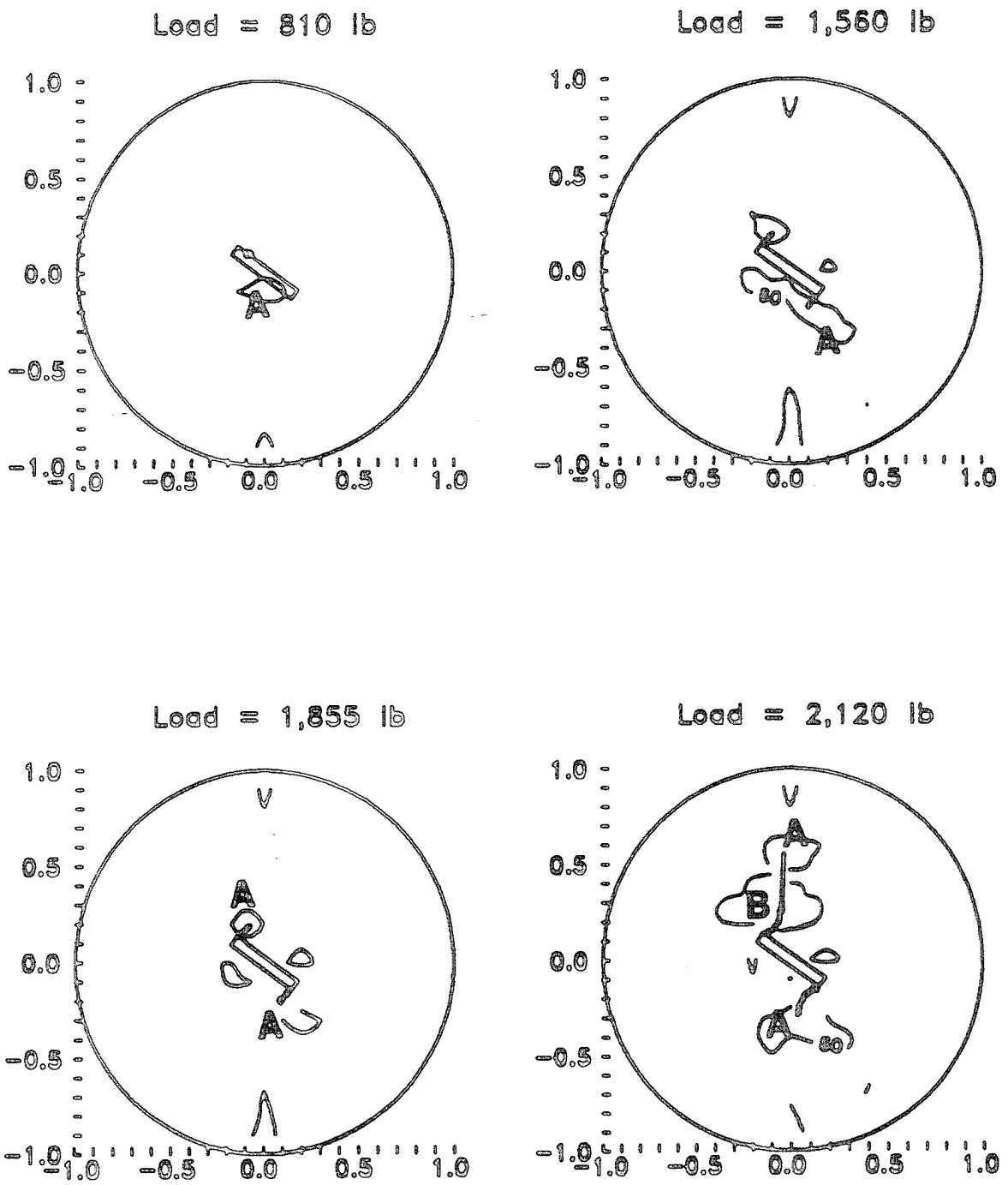

Figure 69 Difference Between Holographic and Linear Elastic Strain Fields. β = 54°

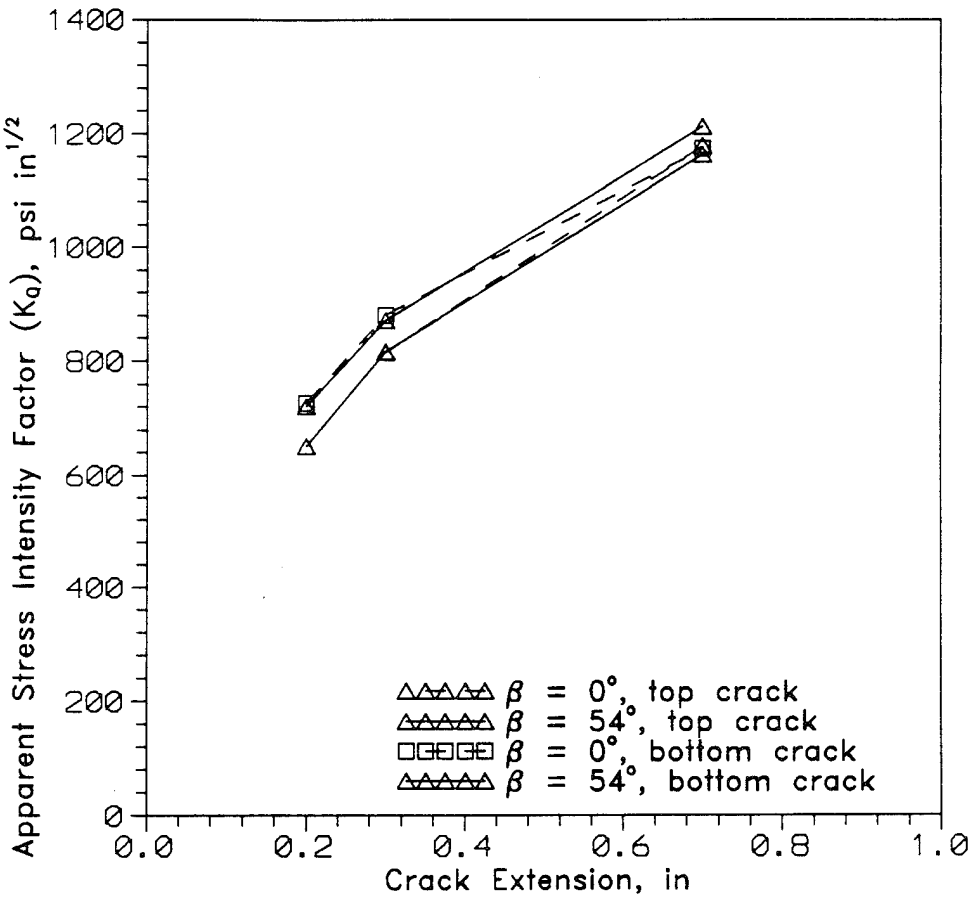

Figure 70 Apparent Stress Intensity Factor(K_Q) vs. Crack Extension(a)

F. CONCLUSIONS

1. Crack initiation occurs at less than 70 percent of the ultimate load for both notch inclination angles. For notch inclination angle $\beta = 0^{\circ}$ the load can be increased beyond the unstable crack level while the mixed mode case is more brittle ($\beta = 54^{\circ}$) in the secondary cracking stage (after the first peak).
2. Examination of the strain distribution at early loading stages can give an indication of the crack growth sequence.
3. The size of the FPZ defined as a function of the tensile strain distribution can give an indication of the cracking mode. Both the FPZ and WFPZ are smaller for mixed mode cracking than they are for mode I.
4. The mixed mode apparent stress intensity factor K_Q exhibits R-curve type of behavior.

SECTION V

STRAIN RATE EFFECT

A. INTRODUCTION

Experimental results indicate that the tensile and compressive strengths of concrete increase with increase of rate of loading (Reference 1, 2). Recent investigations have revealed that such favorable rate effects in strength may be offset by an adverse change in mode of failure. Reinforced concrete structures designed to fail in a ductile flexural mode at slow rates of loading have been observed to fail in a brittle diagonal tension-shear manner at impact rates of loading (Reference 3).

Knowledge of the effect of impact loading on fracture of concrete is essential to predict the rate dependent failure mechanisms in concrete structures. In general, the fracture of reinforced concrete elements occurs under combined Mode I and Mode II loading conditions. Little information is available on the effects of rates of loading on fracture properties of concrete subjected to combined tensile and shear loading.

Various test methods have been used to investigate the effect of impact loading on mechanical properties of concrete in tension, flexure and compression. Ramakrishnan, et.al. (Reference 41) used a conventional drop-weight test to determine the performance of steel-fiber-reinforced concrete. The test consists of repeatedly dropping a known weight on the specimen. The impact resistance is characterized according to the number of strikes required to induce visible damage. Bhargava and Rehnstrom (42) use explosives and high-speed photography to study to the dynamic cracking

behavior of regular and polymer-modified concrete. The Charpy Impact Test developed originally for metals consists of a pendulum-type hammer striking a specimen. The fracture energy is evaluated from the travel of the pendulum after impact. However, the measured energy also includes that absorbed by the testing system and the kinetic energy imparted to the specimen. Both the drop weight test and the Charpy Impact Test have been modified, adding instrumentation to measure load, displacement and strain versus time responses of the specimen during the impact event. Gopalaratnam, Shah and John (Reference 43) developed an instrumented Charpy impact testing system to measure Hammer and support loads independently. They used this test setup to study the impact behavior of steel and glass fiber-reinforced cement composites (Reference 44). For higher rates of loading, the split-Hopkinson bar test enables the determination of stress-strain response in tension and compression. Reinhardt, et al., Malvern, et al. and Ross, et al. (References 6, 5 and 4) have used this method to study the high strain rate behavior of cement based specimens in tension and compression.

The study presented in this section includes the testing of the same center notched cylinder specimens described in Section IV at different rates of loading. First, a quasi-static rate of loading was used under closed loop conditions. Reflection photoelasticity and conventional TV imaging (30 frames per second) was used to evaluate the crack growth. For higher rates of loading, a modified Charpy machine and high speed photography (10,000 frames per second) were used.

B. TESTING PROCEDURE

1. Reflection Photoelasticity

Many transparent, noncrystalline materials are optically isotropic when free of stress but become optically anisotropic and display characteristics similar to crystals when stressed. This behavior is known as temporary double refraction. Materials that exhibit this behavior will be referred to as photoelastic medium in this dissertation. The stress-optic law developed by Maxwell in 1853 (Reference 45) states that the indexes of refraction are linearly proportional to the stresses and followed the following relationships:

$$n_i - n_0 = c_1 \sigma_i + c_2 (\sigma_k - \sigma_i) \quad (9)$$

where: σ_i principal stress
σ_k $\sigma_1+\sigma_2+\sigma_3$
n_0 refraction index in unstressed state
n_i refraction index in stressed state associated with principal direction i
c_1, c_2 stress-optic coefficients

If a plane stress condition is assumed, the stress optic law from the previous equation takes the form:

$$n_2 - n_1 = (c_2 - c_1) (\sigma_1 - \sigma_2) = c (\sigma_1 - \sigma_2) \quad (10)$$

where c a material property (usually independent of the wave length of the light) called the relative stress-optic coefficient.

Now, consider a photoelastic medium of thickness *h* and recall that the refraction index is the ratio of the wave velocity in free space (v_o) to the wave velocity in the material (v) or $n=v_o/v$. Thus, the time (t) required for passage through a material of thickness *h* is given by:

$$t = \frac{h}{v} \quad (11)$$

therefore, the distance by which the wave trails a wave traveling on free space (linear phase shift) is:

$$\delta = v_o t - h = \frac{v_o h}{v} - h = h (n - 1) \quad (12)$$

and the relative linear phase shift between waves traveling along the principal directions of a stressed photoelastic medium is:

$$\delta_{12} = \delta_2 - \delta_1 = h (n_2 - n_1) \qquad (13)$$

which corresponds to the relative angular phase shift given by:

$$\Delta = \frac{2 \pi}{\lambda} \delta_{12} = \frac{2 \pi h}{\lambda} (n_2 - n_1) = \frac{2 \pi h c}{\lambda} (\sigma_1 - \sigma_2) \qquad (14)$$

In engineering practice, this expression is usually expressed in the following form:

$$\sigma_1 - \sigma_2 = \frac{N f_\sigma}{h} \qquad (15)$$

or in terms of principal strains (if the photoelastic medium is perfectly elastic):

$$\varepsilon_1 - \varepsilon_2 = \frac{N f_\varepsilon}{h} \qquad (16)$$

where N is the relative phase shift in terms of complete cycles of retardation and f_σ and f_ε are known as the material fringe values in terms of stress and strain respectively and can be established by calibration.

A polariscope is used in order to measure the phase shift (N) at each point on a stressed model. A dark field circular polariscope (Figure 71) was used during this investigation. A detailed explanation of the operation of this and other types of polariscope was shown in Reference 45.

The objective of the polariscope is to transform relative phase shifts into observable intensity differences. If the stressed photoelastic medium shown in Figure 71 is illuminated through the polariscope by a light beam of intensity k and frequency ω, the light wave emerging from the polariscope is:

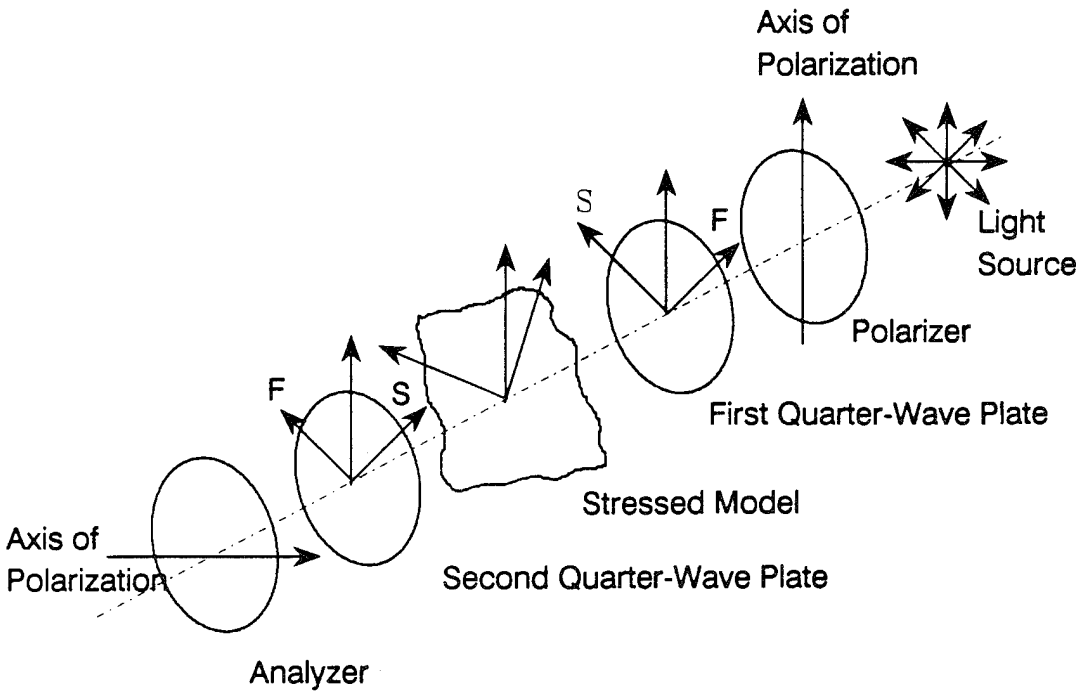

Figure 71 Circular Polariscope (Dark Field)

$$E_{ax} = k \sin\left(\frac{\Delta}{2}\right) \sin\left(\omega t + 2\alpha - \frac{\Delta}{2}\right) \qquad (17)$$

Since the intensity of light is only proportional to the square of the amplitude of the light wave, the intensity of the light beam emerging from the circular polariscope is a function only of the angular phase shift (independent of the frequency, ω and the phase, α) and is given by:

$$I = K \sin^2\left(\frac{\Delta}{2}\right) \tag{18}$$

When $\Delta/2 = n\pi$, where n=0,1,2,3,..., the intensity value is zero (extinction). A fringe is formed of the loci of all the point in the model with the same order of extinction (n). This fringe pattern is called the isochromatic fringe pattern. The order of extinction n, depends on both the principal stress difference and the wave length used to illuminate the model (Equation V.7). When the model is illuminated with white light (linear combination of light waves of different wave length), the isochromatic fringe pattern appears as a colored fringe pattern and there is a relationship between fringe color and relative phase shift. The polariscope described above is called a dark field polariscope because the unstressed material appears dark. If the analyzer plate is rotated 90 degrees such that the axis of polarization is parallel to that of the polarizer plate (light field polariscope), the unstressed material would appear white. In this investigation a dark field arrangement was selected for quasi-static loading and a light field polariscope for impact loading because they were best suited for the corresponding imaging method.

In order to study opaque objects, the method of birefringent coatings or reflection photoelasticity is used. The photoelastic medium is a thin coating which is bonded to the surface of the specimen. Figure 72 shows the reflection polariscope used for this study. The operation of the polariscope is very similar to that of a conventional circular polariscope. The bonding agent between the photoelastic medium and the specimen is highly reflective and provides a mirror like surface. Since the light travels through the coating in both the incident and the reflected direction, a modified thickness h' = 2h should be used for the analysis.

2. Quasi-Static Loading

Center-notched disk specimens (CNDS) identical to those described in Section IV were used. A photoelastic coating type PS-1, 0.01 inch thick was glued to each surface

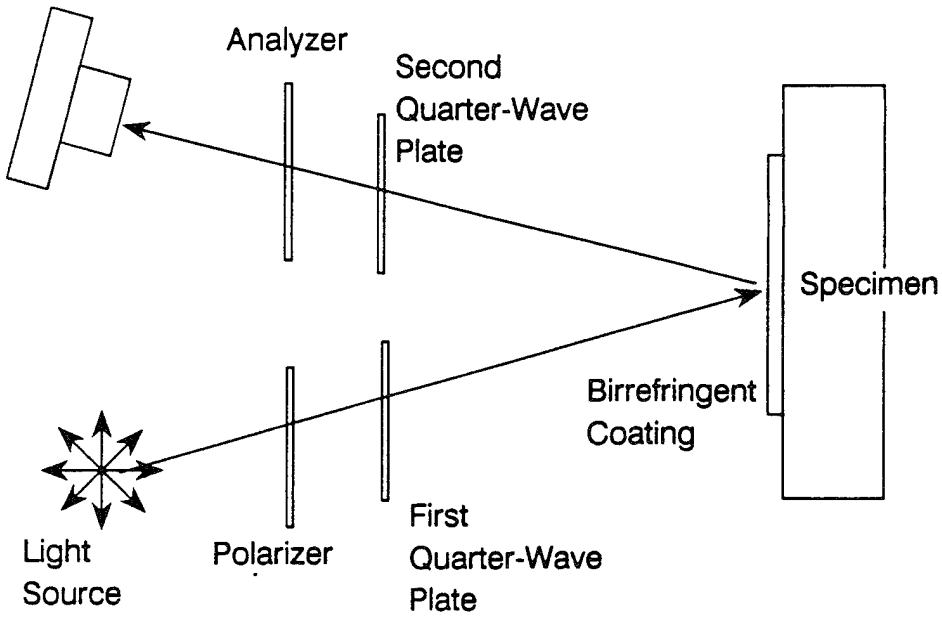

Figure 72 Circular Reflection Polariscope

of the specimen to preserve symmetry. Specimens were tested using the same mechanical setup and instrumentation described in Section III up to the limit of the instrumentation used for closed loop control. A Panasonic S-VHS TV camera was used to record the isochromatic fringes continuously.

3. Instrumented Impact Loading

The instrumented Charpy machine used by Gopalaratnam, Shah and John (Reference 43) (Figure 73) was modified to accommodate CNDSs. A modified instrumented striker (tup), instrumented anvil, a specimen support and an anchor were fabricated. Figures 74 to 76 show the instrumented striker, instrumented tup and general assembly for he modified Charpy machine. A full Wheatstone bridge was connected on both tup and anvil

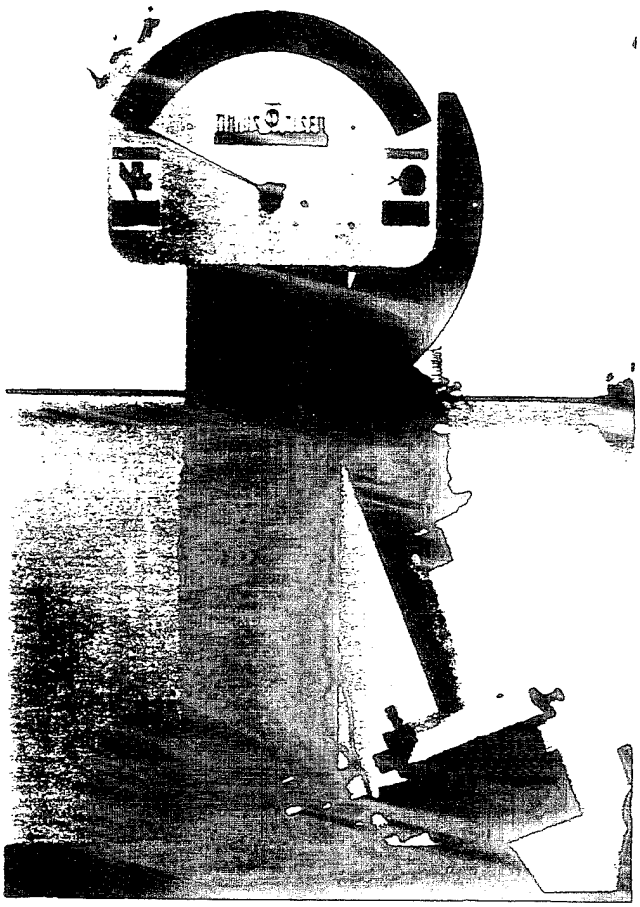

Figure 73 Instrumented Charpy Machine

sensitive only to axial load. A Tektronix 2232 model oscilloscope was used for data acquisition at a rate of 250 KHz. Both the striker and the anvil were calibrated at static rate of loading in a 20 kip capacity MTS load frame under load control up to 10,000 lb. Dynamic calibration was achieved by placing a dynamic load cell in place of the specimen. Typical calibration results are shown in Figure 77. In order to estimate the inertial effect dummy specimens were tested and the responses from the tup and anvil were compared as shown in Figure 78. It was found that both peak load and arrival time differences are small (5 percent) compared to the overall response and inertia effects can be neglected.

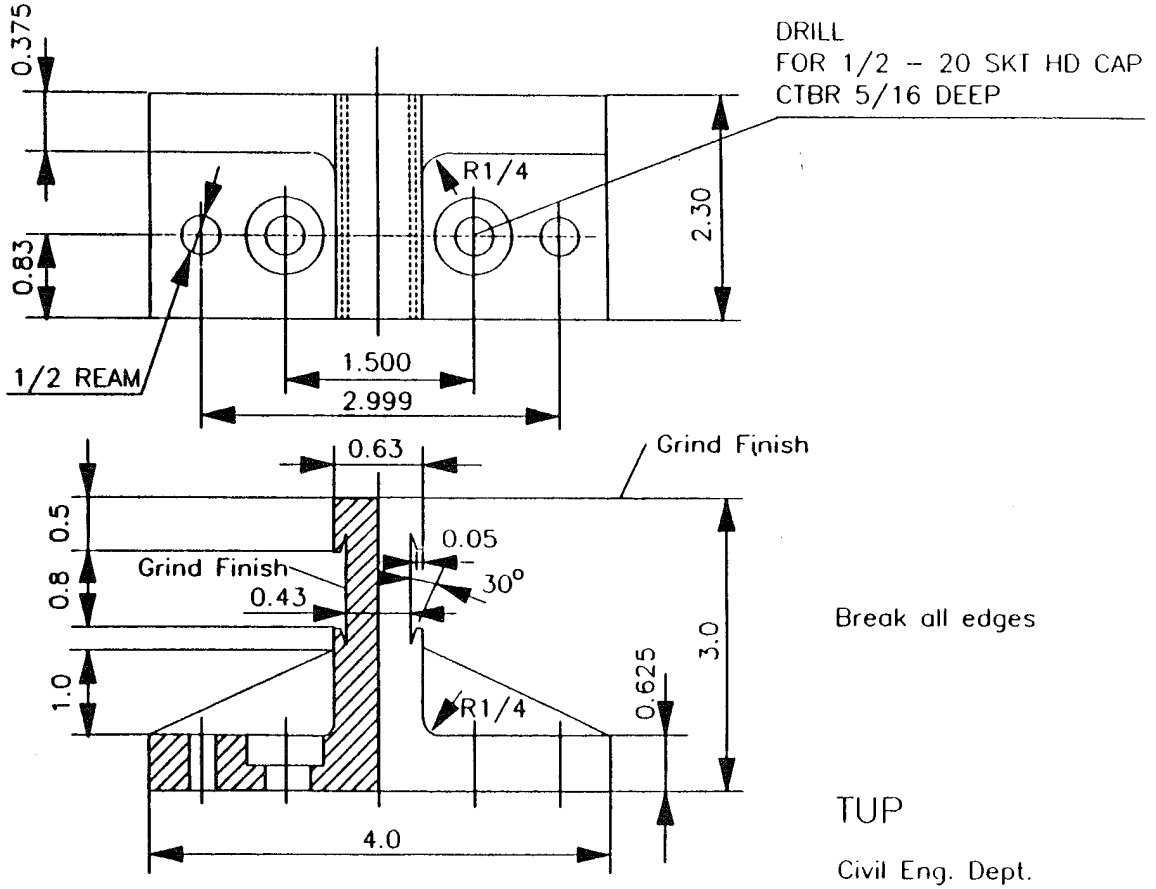

Figure 74 Instrumented Striker (Tup)

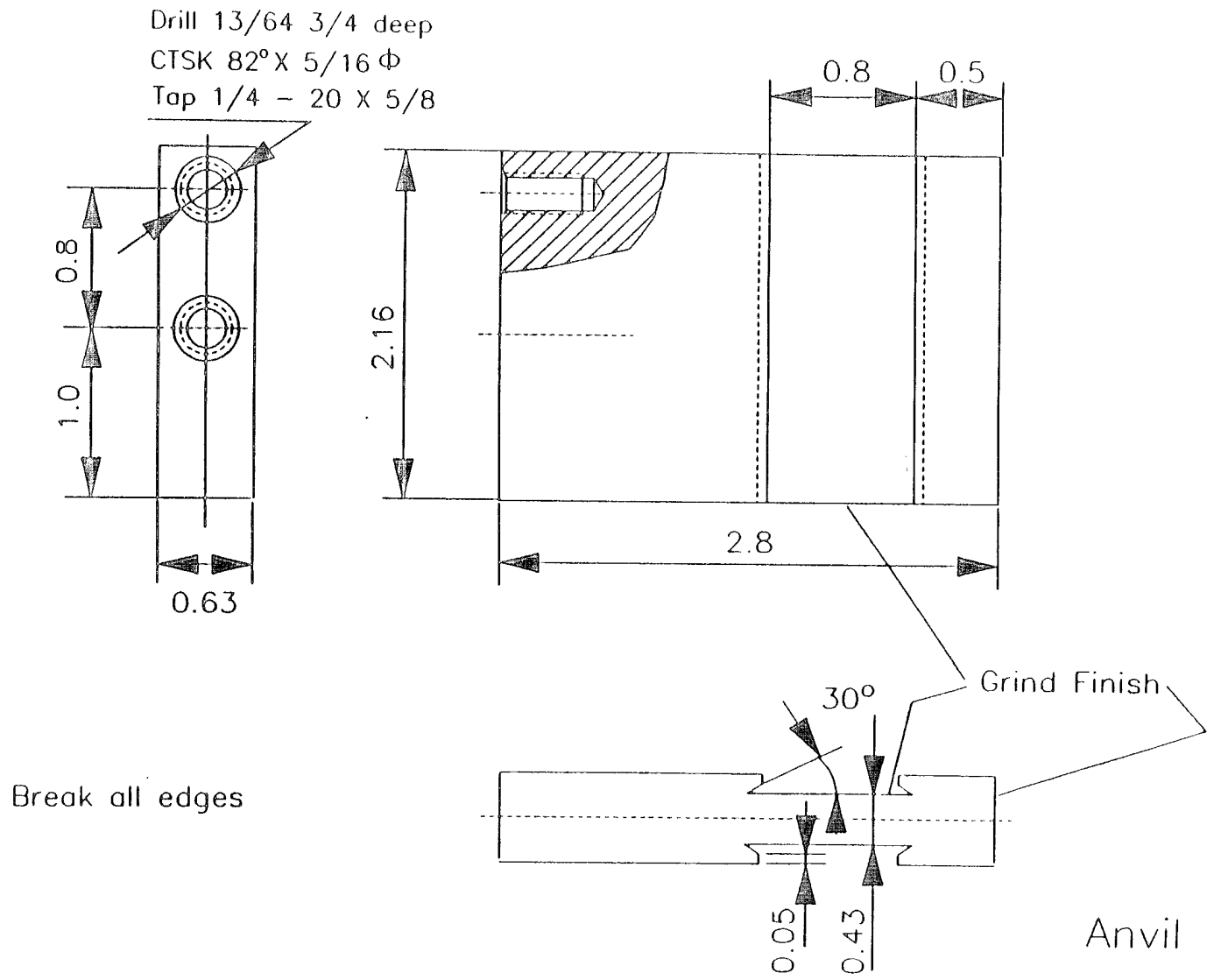

Figure 75 Instrumented Anvil

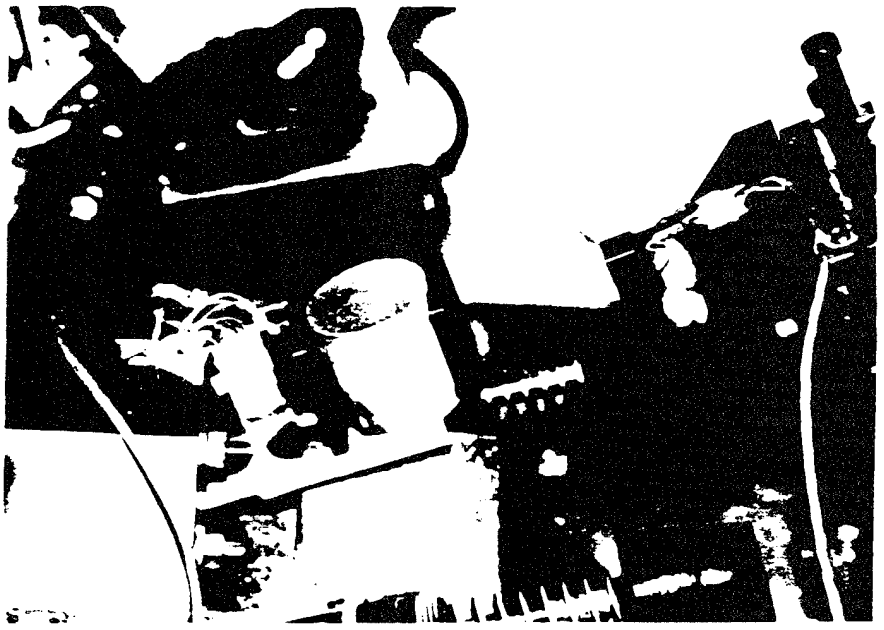

Figure 76 Modified Charpy Machine Striker-Support Assembly

For evaluation of crack propagation, the same photoelastic coating described in Section V.2.2 was glued to front and back faces of the specimens. A lens was incorporated in the polariscope arrangement (Figure 79) to increase the light intensity to the level required for high-speed photography. Halogen light was used for illumination. A high-speed camera Model 100 (Photographic Analysis Company) was used for recording of the isochromatic fringes (Figure 80). 450-foot rolls of SO-259 Kodak film (400 ASA) for high speed photography were used. The high speed camera was used to trigger the overall system. After a time delay required to bring the film up to speed, the camera closes an electric circuit which activates a relay to release to pendulum of the Charpy machine (Figure 81). Data acquisition was triggered by the impact between the striker and the specimen. A second 2232 Model Tektronix oscilloscope was used at low frequency (5 KHz) to measure the time difference between the release of the pendulum and impact with the specimen.

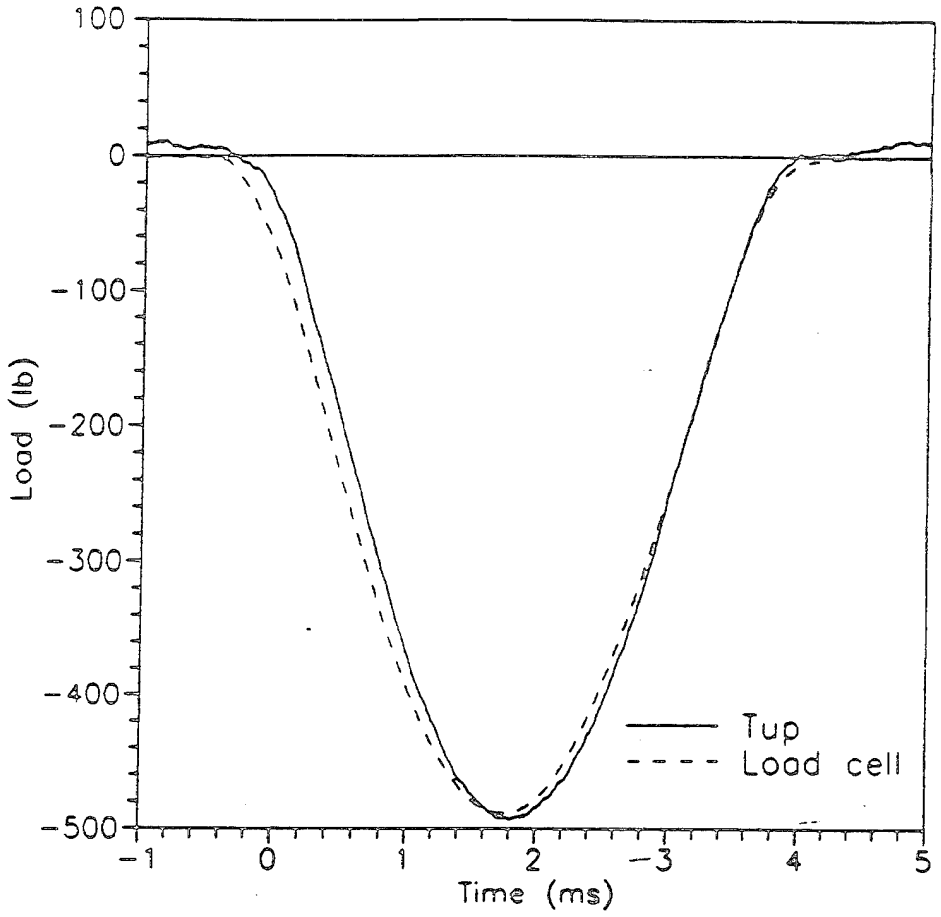

Figure 77 Typical Calibration Results

C. RESULTS

1. Quasi-Static Loading

Specimens with 5 different notch inclination angles were tested. Figure 82 shows a compilation of the results for the specimens tested at quasi-static loading. A more detailed presentation of the results for the unnotched, 0° and 54° inclination angles is discussed in the following paragraphs.

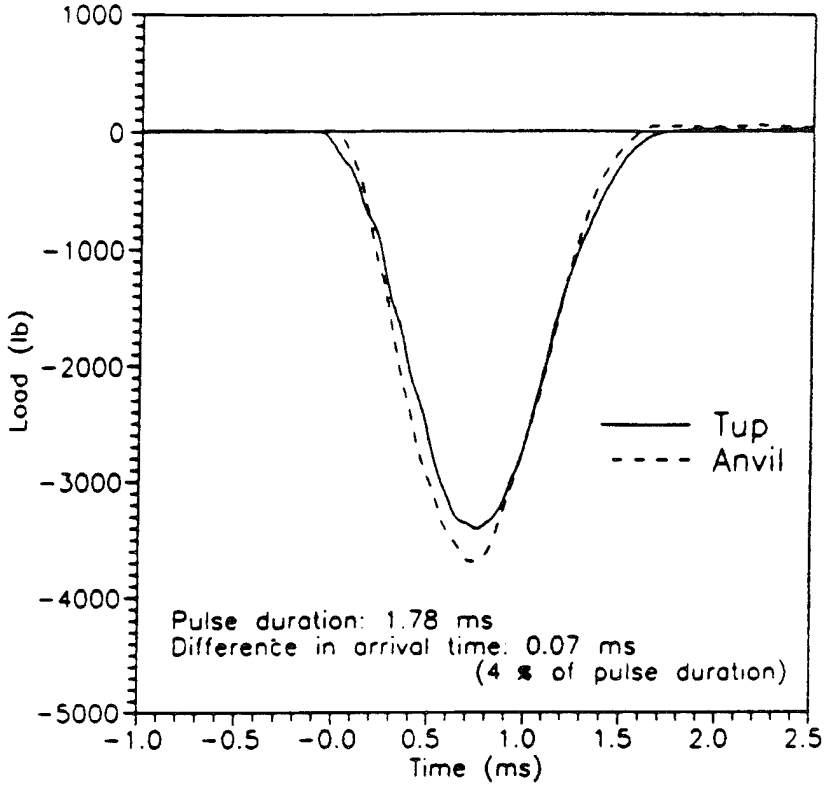

Figure 78 Dynamic Calibration. (Inertia Effect)

In the load-deformation curve for the unnotched specimen shown in Figure 83, the stars indicate the location of photographic recordings. As discussed earlier, continuous imaging at 30 images per second were recorded using a S-VHS tape recorder. The most significant stages of crack propagation are shown in Figures 84 and 85. Note that the failure sequence follows closely the holographic observations presented in Section III.5. The images in Figure 84 and 85 lead to the conclussion that the more sensitive (0.125 inch thickness) photoelastic coating used in this experiment is sensitive to deformations along the crack trajectory, but measurement of the far-field deformations is not possible. To reduce the 'reinforcing' effect of the photoelastic coating, a thinner, less sensitive coating was used for all the subsequent experiments.

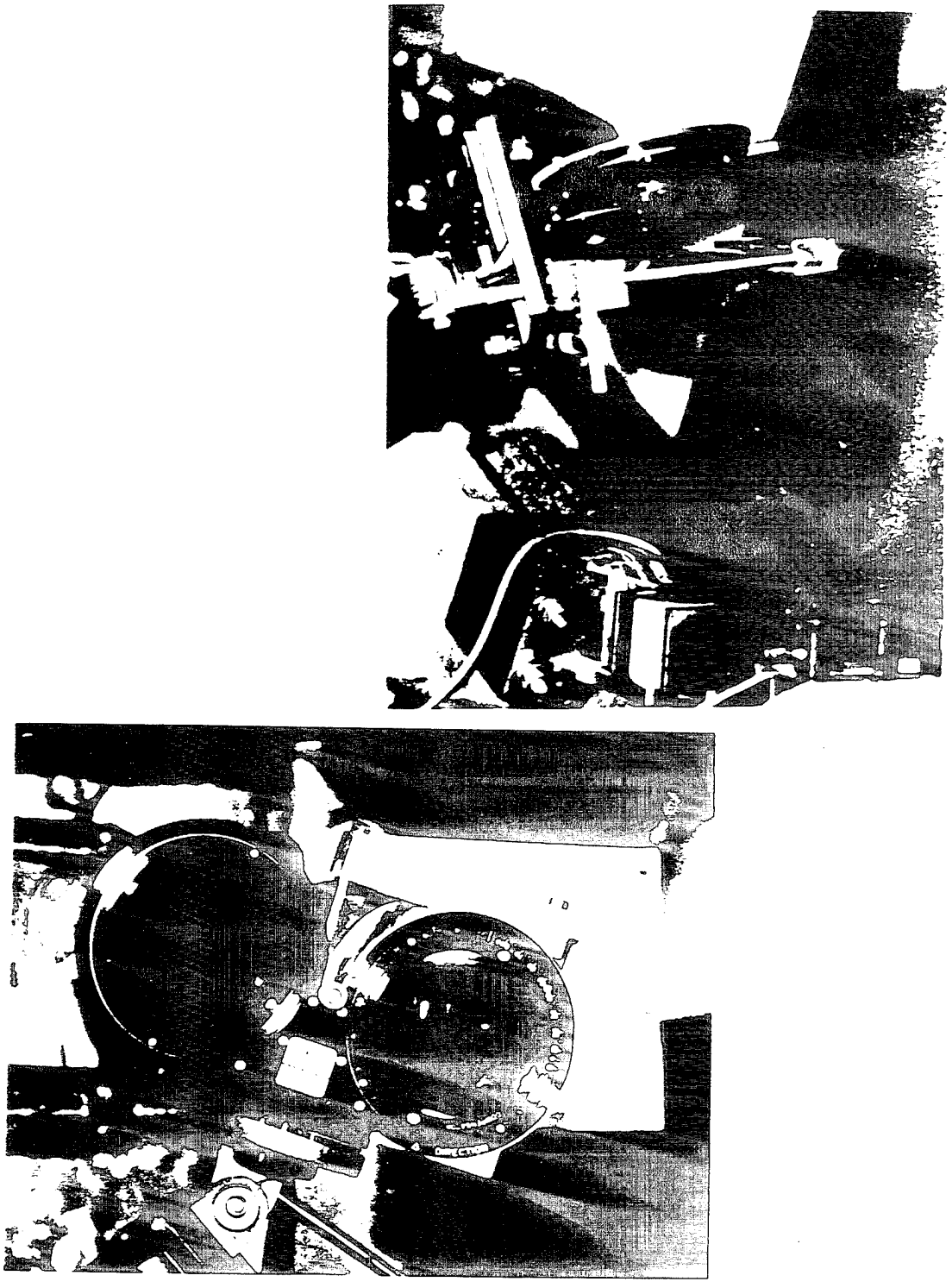

Figure 79 Reflection Polariscope Arrangement for Instrumented Impact

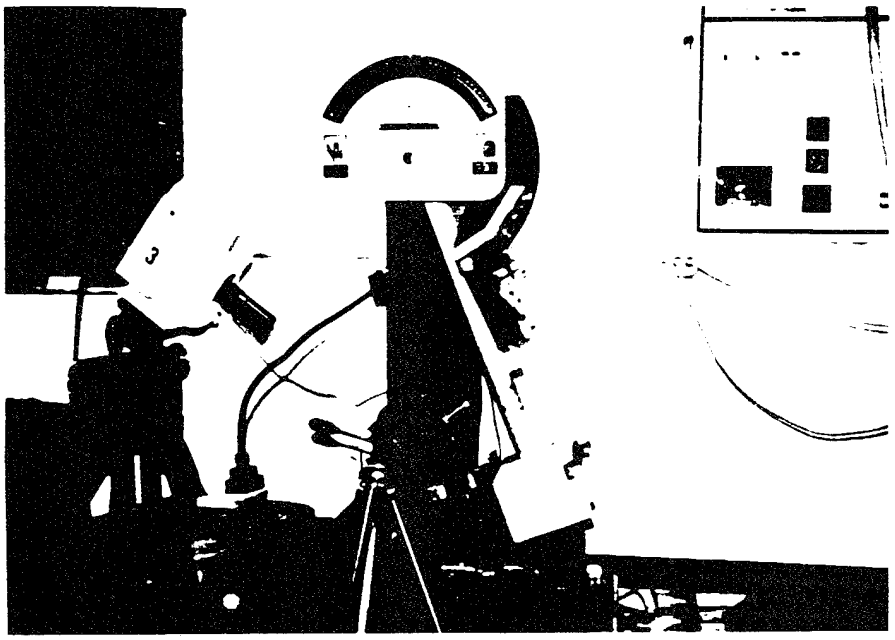

Figure 80 High Speed Photography Arrangement for Instrumented Impact

Figure 86 shows the load deformation curve for a specimen with notch inclination angle $\beta = 0°$. Note that at Point B, there is a first peak characteristic of crack initiation and propagation based on the holographic results reported earlier. However, the isochromatic fringe patterns shown in Figures 87 and 88 indicate that cracking starts at Point C. Between Points C and G the main crack grows through the specimen and a second peak is observed in the load-deformation curve. The above phenomenon can be attributed to asymmetric failure. Previous calibration experiments had shown that it is possible for the crack to initiate and propagate on one face of the specimen before cracking starts on the opposite face due to slight eccentricity of the load or specimen imperfections. A difference in behavior between the holographic test reported in Section II and this experiment is the significant additional load capacity after crack propagation. After cracking, a secondary failure mechanism develops which results in the failure wedge reported in Section IV. However, even after large crack openings, the photoelastic coating provides a relatively strong joint between the crack faces as compared to the

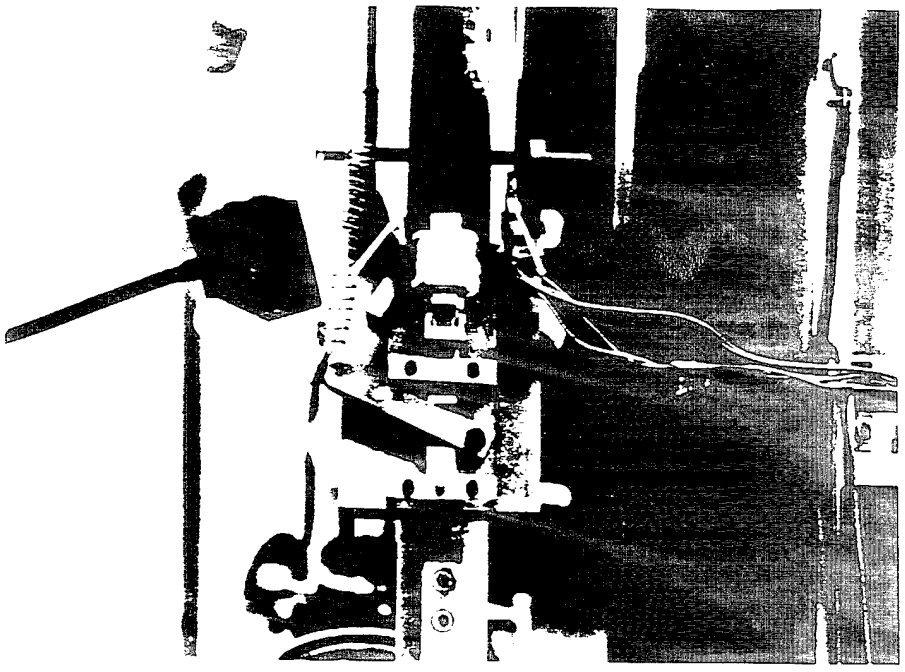

Figure 81 Pendulum Release Mechanism

uncoated specimens. Final failure occurs at 2.5×10^{-3} inch of diametral displacement, which corresponds to the wedge formation.

Figures 89 to 91 show the load-deformation curve and isochromatic fringe patterns for a specimen with notch inclination angle $\beta = 54°$. Symmetric failure was observed in this specimen and both the load-deformation curve and the crack growth agree with the observation obtained using laser holographic interferometry. The first crack propagates through the specimen between Points B and G located before the first peak in the load-deformation curve. The second peak reaches a slightly higher load value than the first peak (as opposed to the lower load level in the holographic experiment). The top of the second peak can be correlated to the initiation of the secondary crack at Point K. Between the two peaks the physical mechanism is characterized by opening of the first crack and the reinforcing effect of the photoelastic coating becomes important.

After the secondary cracks have grown, there is a plateau in the load-deformation curve at collapse of the specimen occurs at point N after the photoelastic coating has

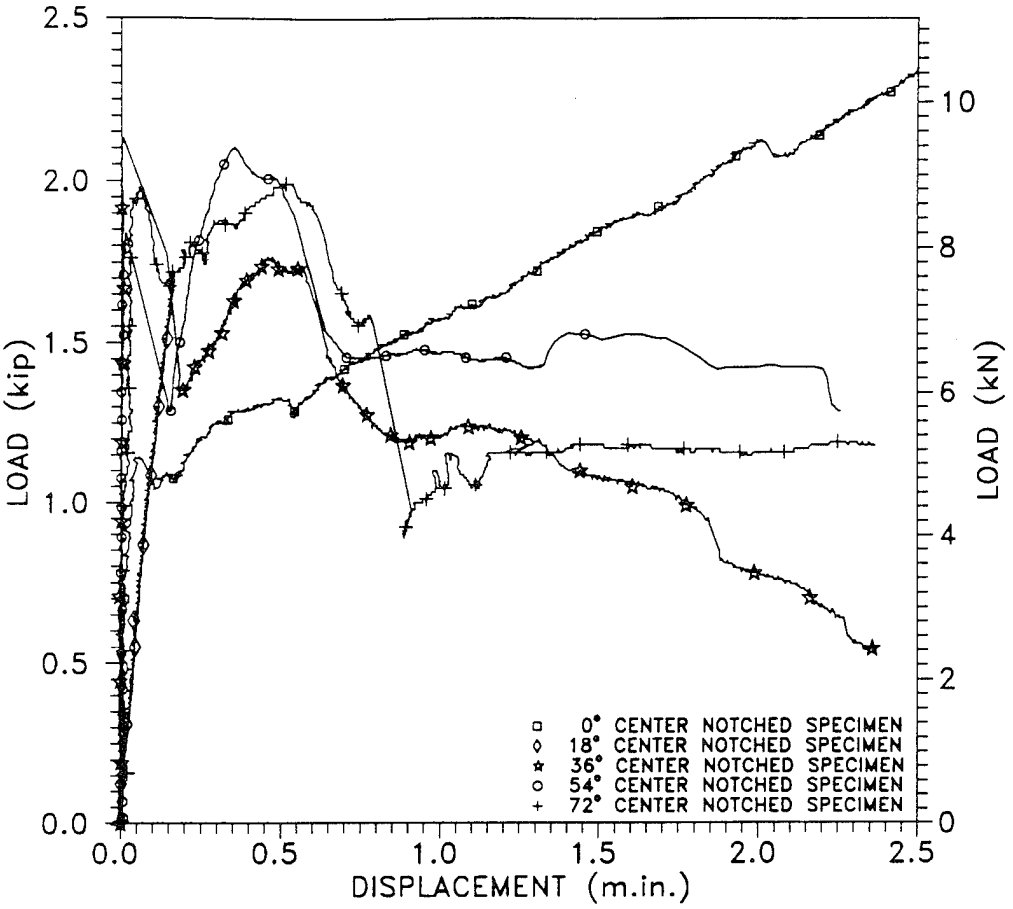

Figure 82 Load Deformation Curves for Specimens Tested at Quasi-Static Loading.

debonded from the specimen.

Post-failure examination of the specimen indicates that the concentration of isochromatic fringes follows closely the crack trajectory on the surface of the specimen. Thus, the possibility of local debonding of the photoelastic coating before cracking should be eliminated.

In general, an acceptable agreement was found between holographic and photoelasticity observations regarding crack formation and propagation at slow rates of loading. The modes of failure were not modified by the existence of the photoelastic

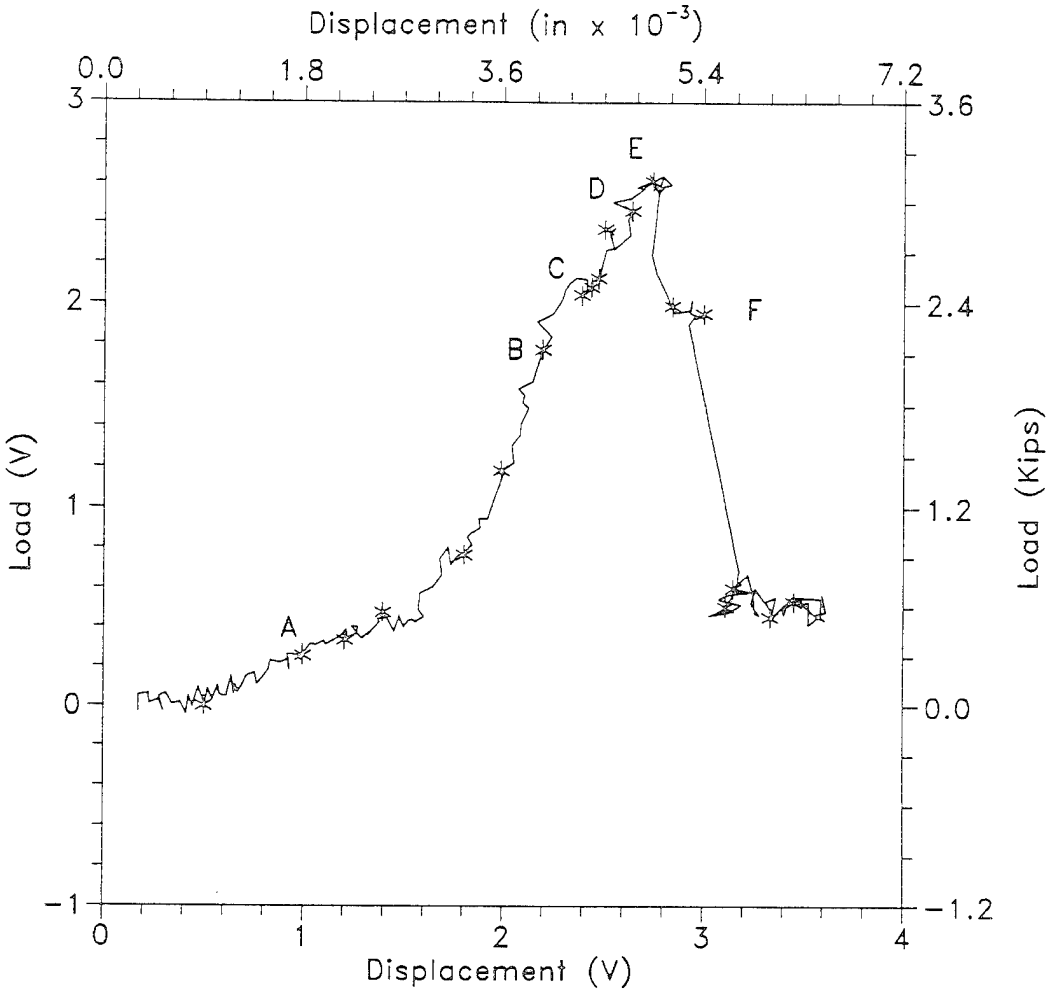

Figure 83 Load Deformation Curve. Unnotched Specimen. Quasi-Static Loading.

coating and, although some reinforcing effects were observed the structural behavior of the specimen showed the same trends for different notch inclination angles.

2. Impact Loading (strain rate 1 to 10 per sec)

A comparison of the load vs. recordings at impact loading for various notch inclination angles is shown in Figure 92. In general, the trends agree with results obtained at low rates of loading. For inclination angles $\beta = 0°$ and $\beta = 18°$, there is evidence of ductile

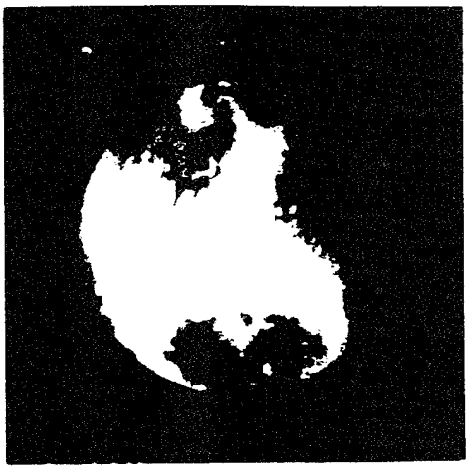

A

B

C

Figure 84 Isochromatic Fringes. Unnotched Specimen. Quasi-Static Loading. (Expossures A,B and C)

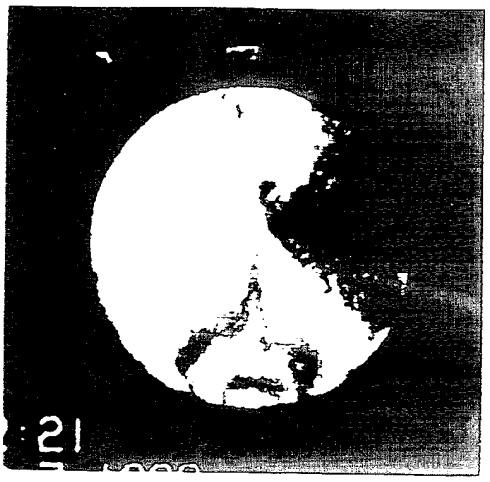

D

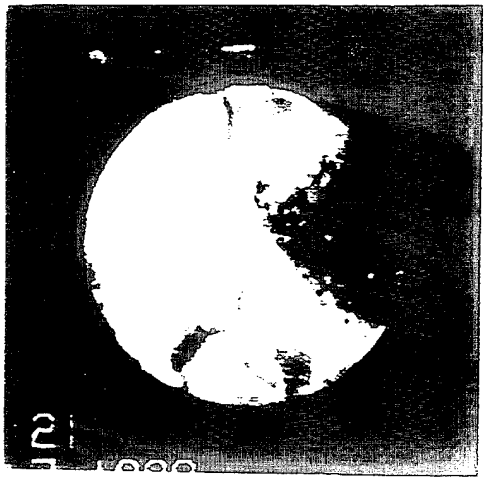

E

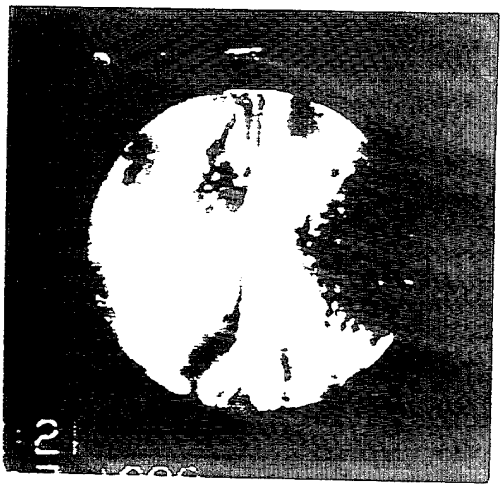

F

Figure 85 Isochromatic Fringes. Unnotched Specimen. Quasi-Static Loading. (Expossures D,E and F)

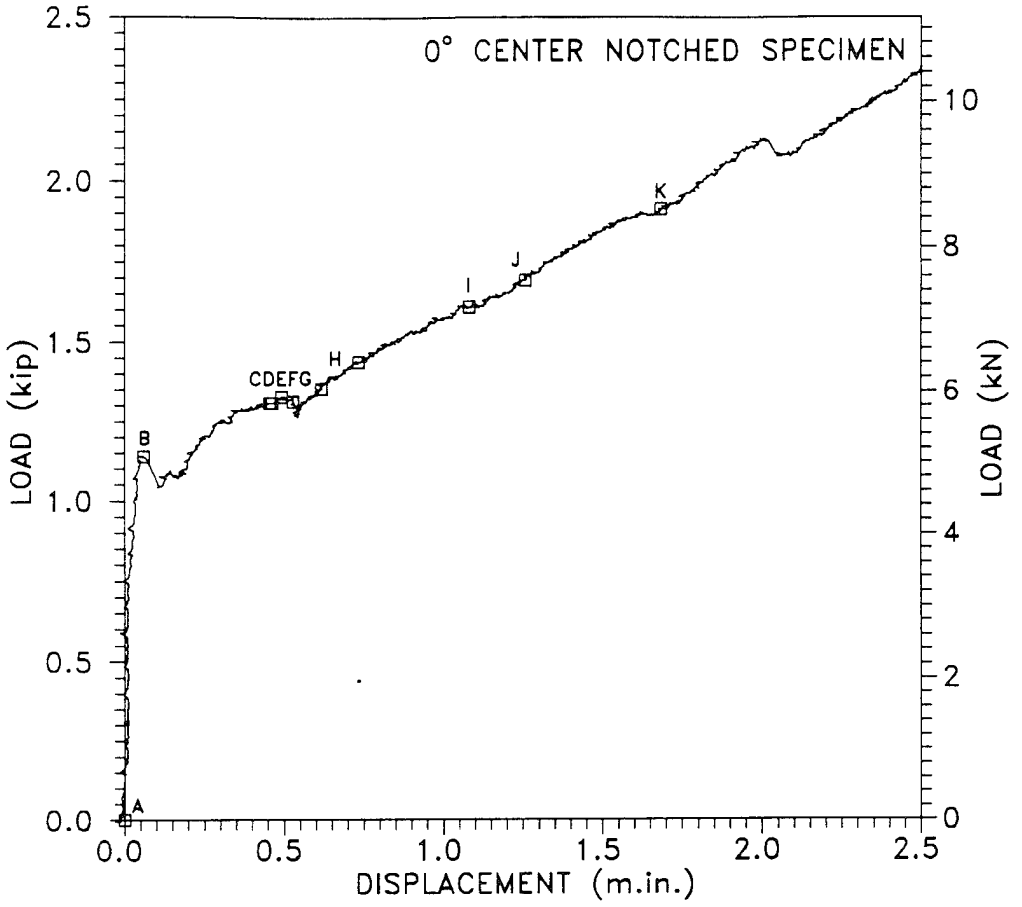

Figure 86 Load-Deformation Curve. $\beta = 0°$. Quasi-Static Loading.

behavior represented as a short plateau at the peak load while for higher inclination angles the response is quite brittle. The unnotched specimen shows a sharp unloading after the peak load followed by a subsequent region of constant load over a relatively long period of time. Two unnotched specimen were tested under impact loading using high speed photography. Unfortunately, none of the recordings was successful in observing crack growth for the unnotched specimen.

The impact energy was selected such that the failure mode remained the same as that observed during the slow rate experiments. Therefore, the observed macroscopic rate

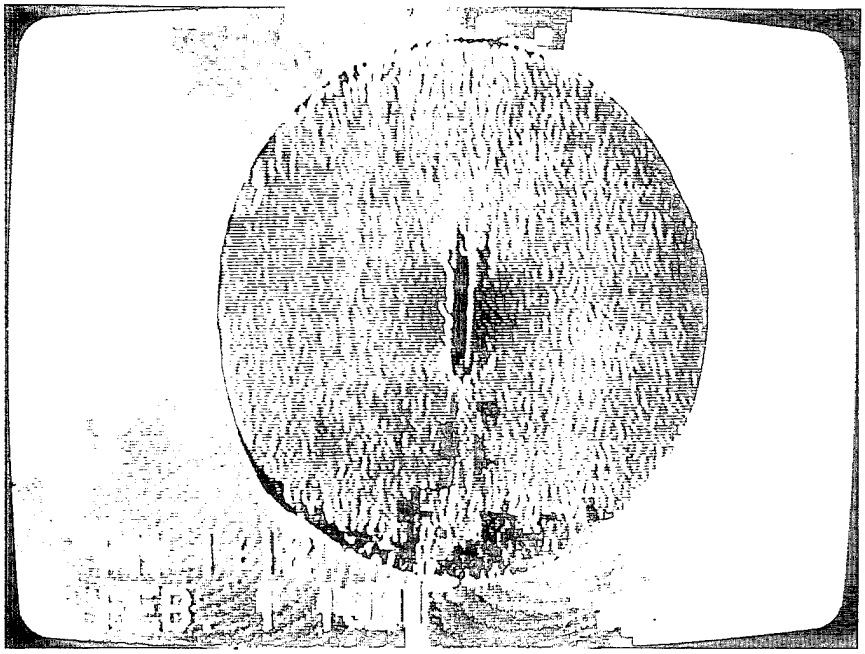

B

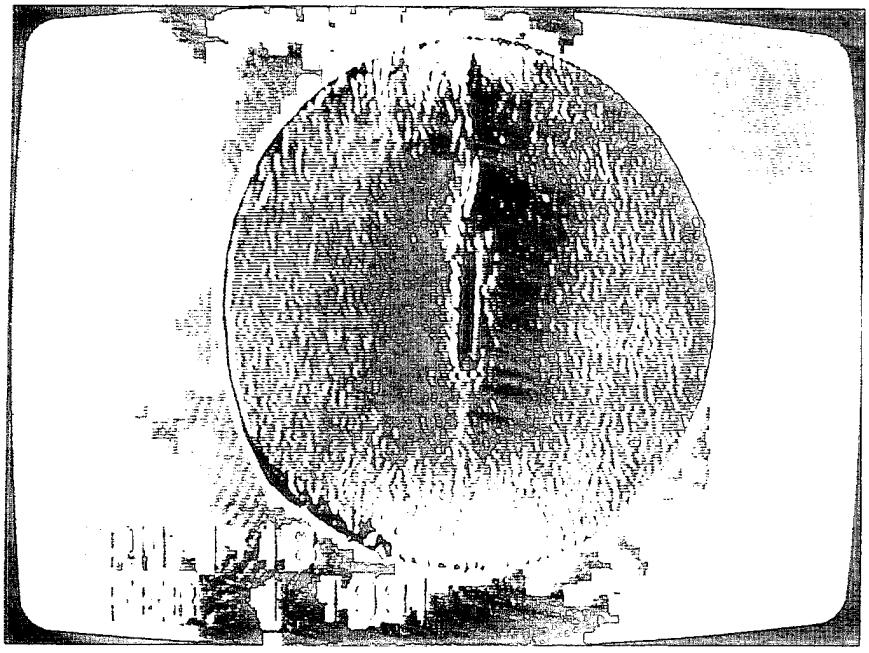

C

Figure 87 Isochromatic Fringes. β = 0°. Quasi-Static Loading. (Expossures B and C)

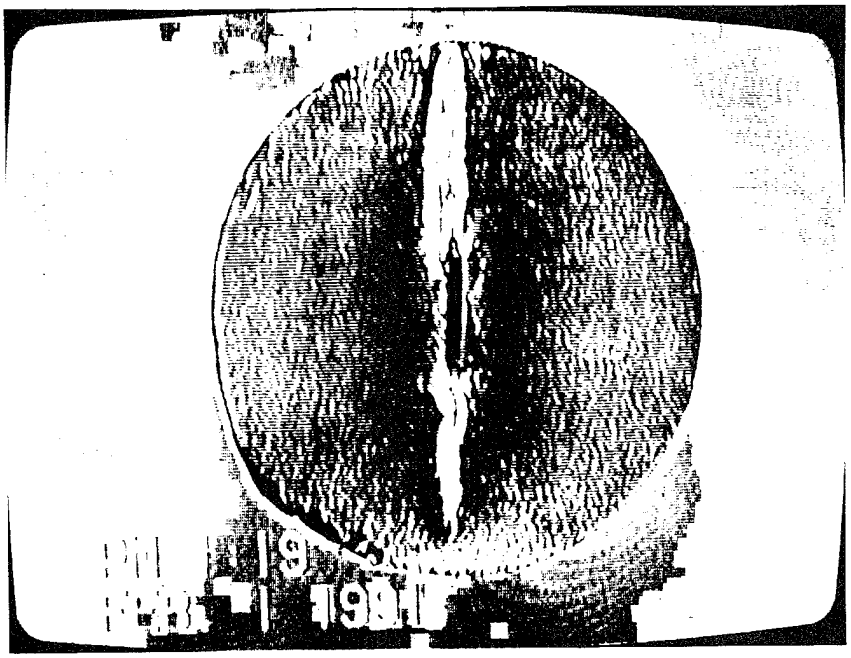

G

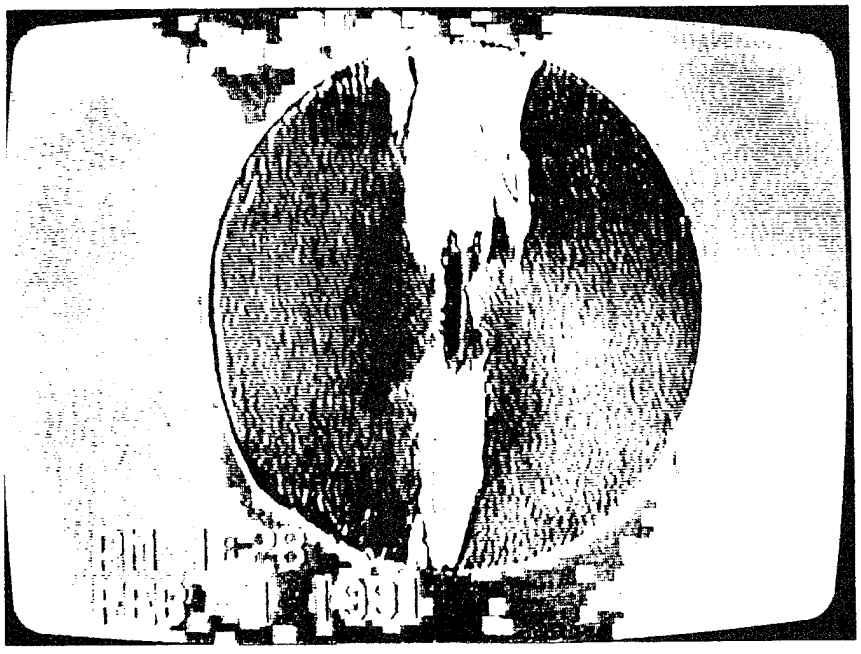

L

Figure 88 Isochromatic Fringes. β = 0°. Quasi-Static Loading. (Expossures G and L)

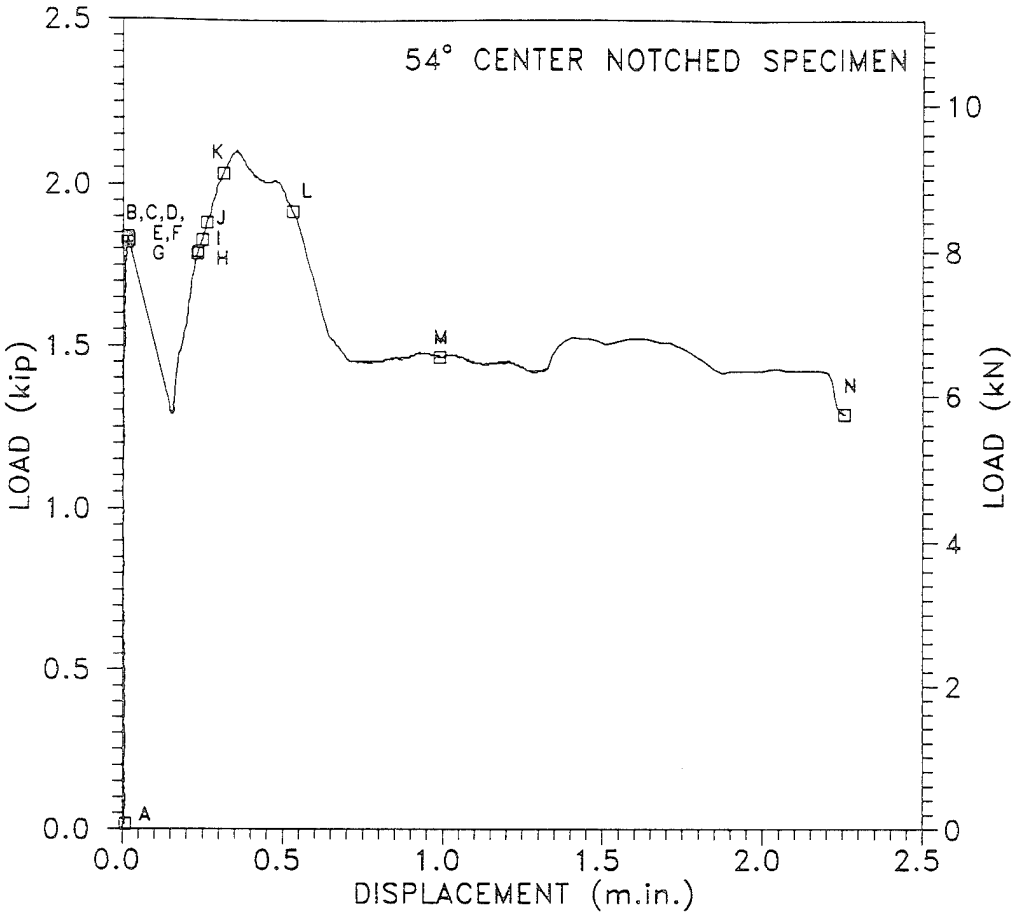

Figure 89 Load-Deformation Curve. β = 54°. Quasi-Static Loading.

effects can be related only to the rate effect on crack initiation and crack growth. Higher rates of loading usually result in fragmentation of the specimen and different failure mechanisms.

Figure 93 shows the load record for a specimen with notch inclination angle $\beta = 0°$. An isochromatic fringe pattern was recorded at constant intervals of 0.1 ms. however, the timing of the photographic exposures can only be determined within 0.05 ms (i.e. photographic exposures could be shifted forward or backward by 0.05 ms in Figure 93 but the interval between exposures remains 0.1 ms). Figures 94 and 95 show the

B

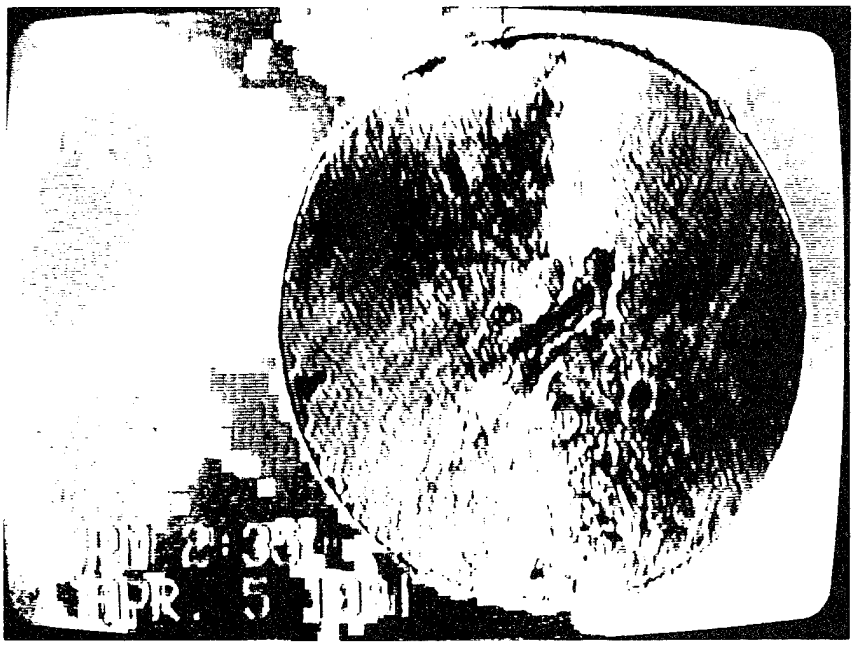

D

Figure 90 Isochromatic Fringes. β = 54°. Quasi-Static Loading. (Expossures B and D)

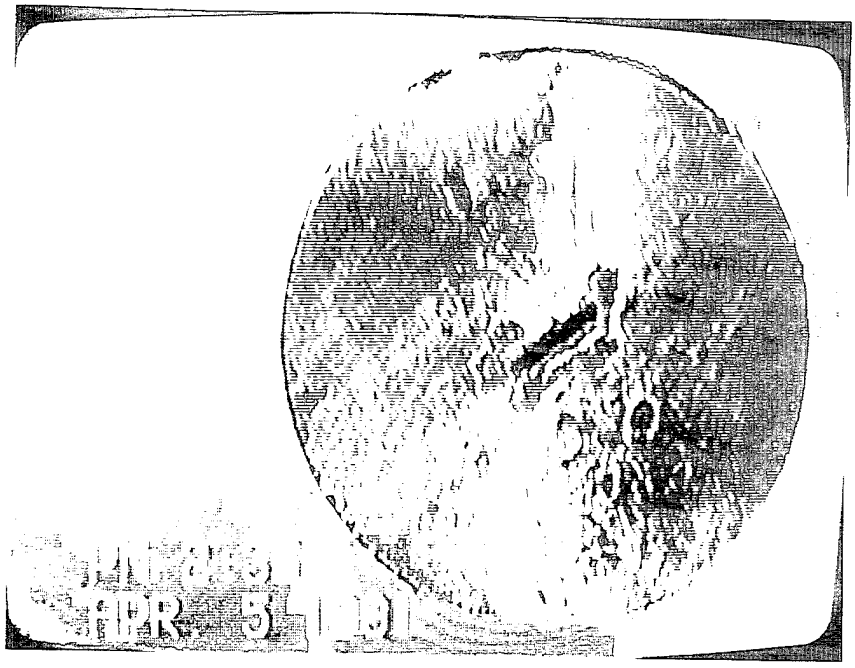

G

K

Figure 91 Isochromatic Fringes. β = 54°. Quasi-Static Loading. (Expossures G and K)

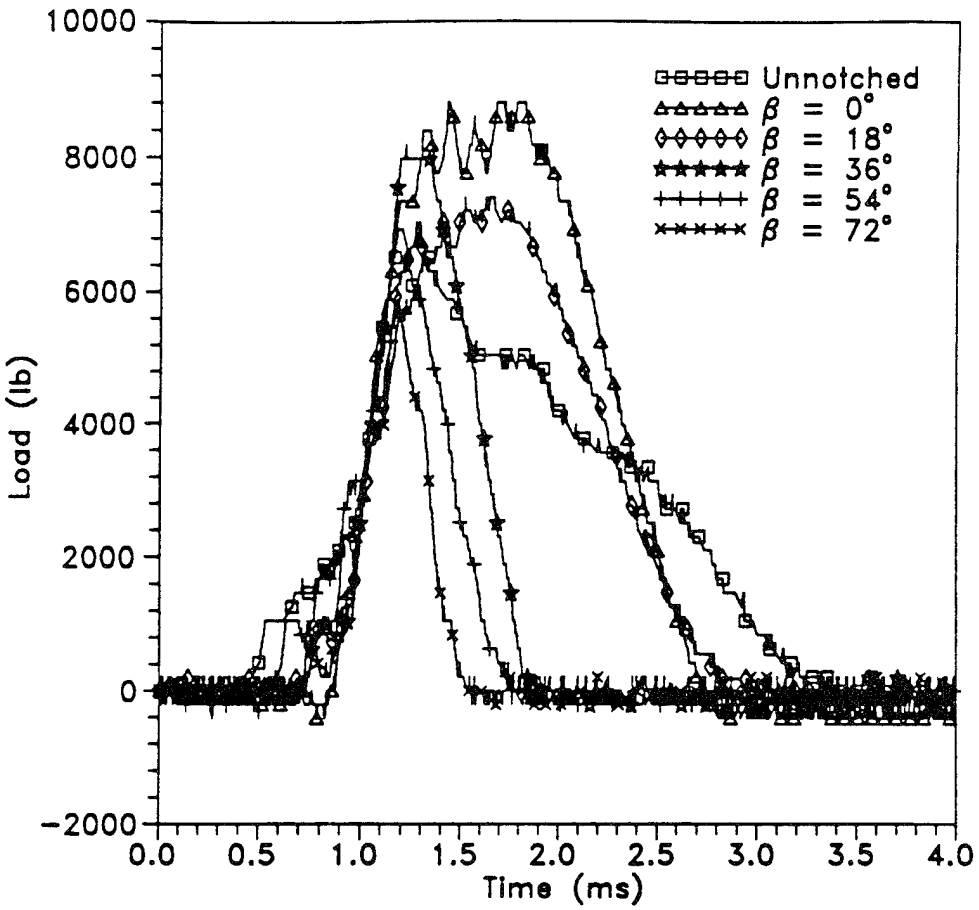

Figure 92 Load History Record for Various Notch Inclination Angles at Impact Loading.

sequence of isochromatic fringe pattern recordings corresponding for the same specimen. Unfortunately, the pictures shown in this dissertation are not as clear as the original film due to the reproduction process but some observation can still be made. The failure sequence agrees with both the holographic and photoelasticity observations at low rates of loading. Point C, shows a concentration of deformation along the crack path but it is unclear whether crack has initiated or not. At Point D there is a crack on each tip of the notch and started to propagate towards the points of application of the load and

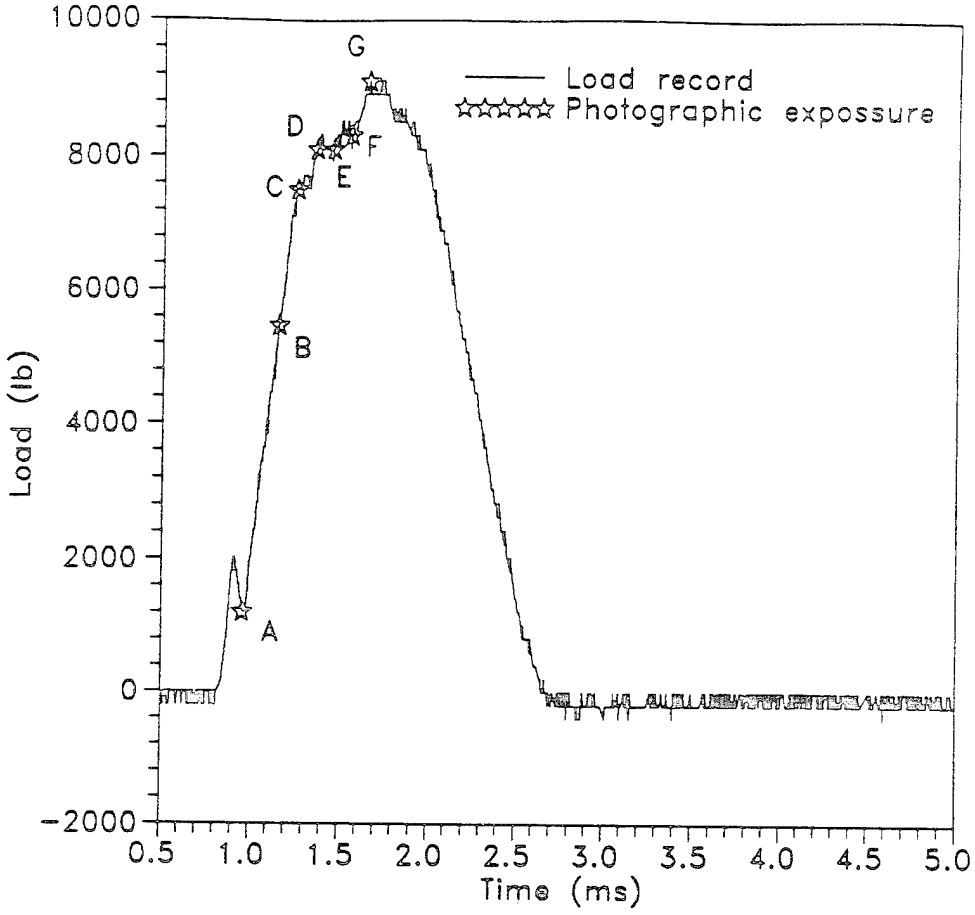

Figure 93 Load Record and Photographic Exposures. β = 0°. Impact Loading.

at Point E the crack has propagated through the specimen. At Point E there is what appears to be an unloading region in the load vs. time record. This corresponds to first peak observed at low rates of loading. A second peak is found at point G where the secondary crack initiates (Figure 95). Postfailure examination of the specimens showed that the crack patterns correspond to the isochromatic fringe patterns. Debonding of the photoelastic coating was observed. Further examination of the failed specimens showed that debonding occurred between the photoelastic coating and the reflecting paint on the

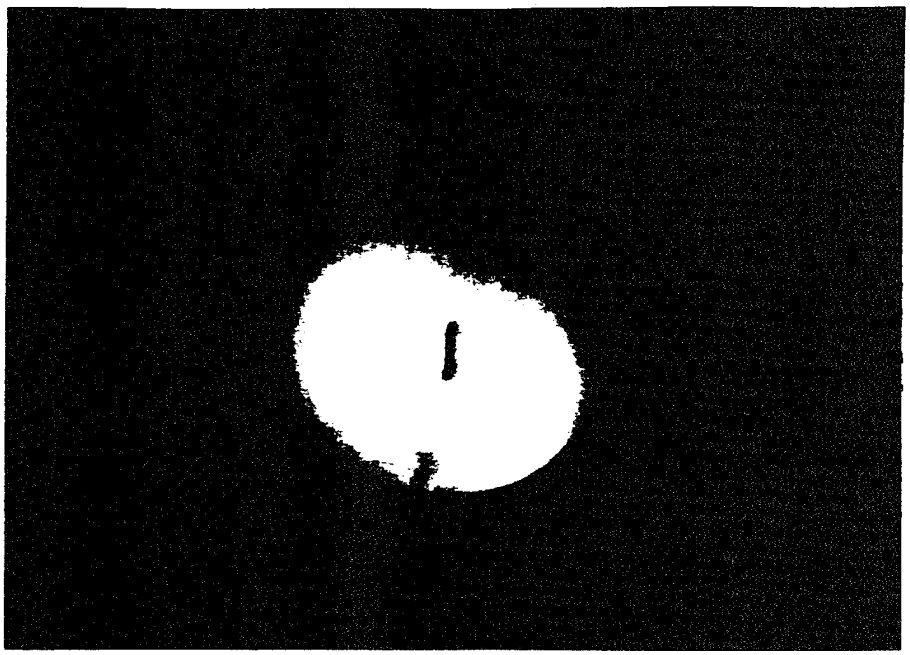

C

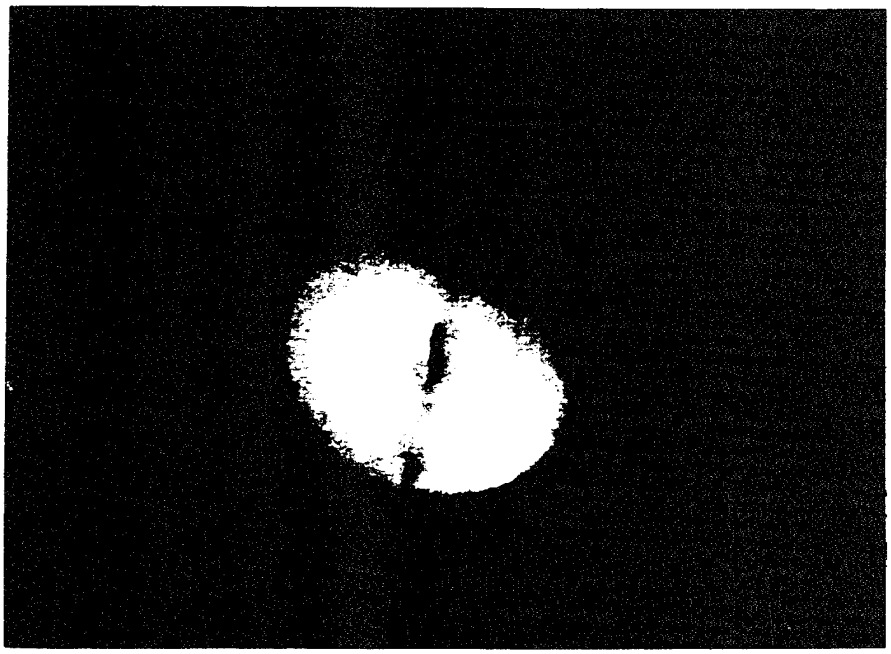

D

Figure 94 Isochromatic Fringe Patterns. $\beta = 0°$. Impact Loading. (Expossures C and D)

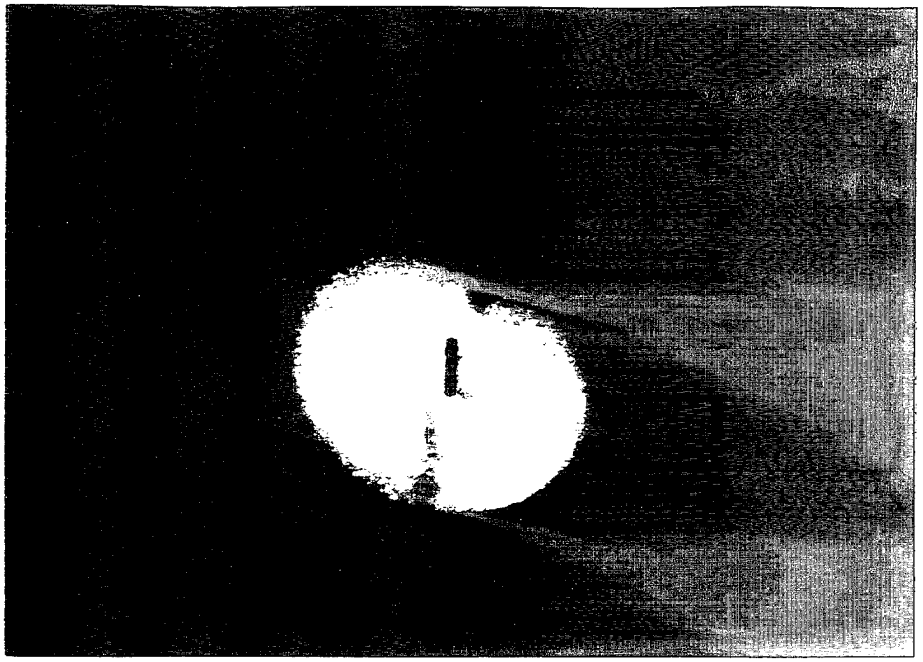

E

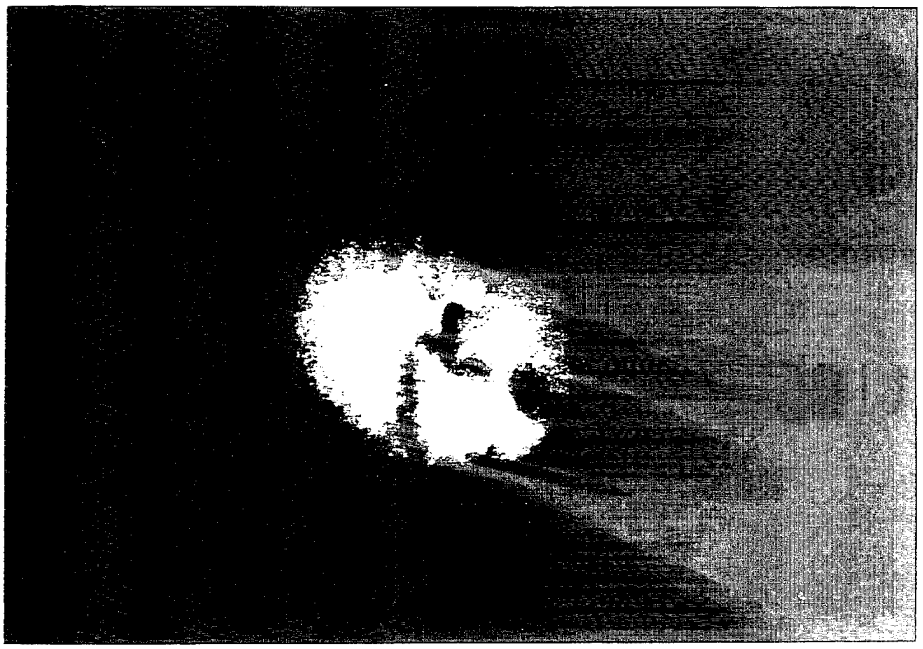

G

Figure 95 Isochromatic Fringe Patterns. β = 0°. Impact Loading. (Expossures E and G)

back face of the photoelastic medium.

The load history for a specimen with notch inclination angle β = 54° is shown in Figure 96. Figures 97 and 98 show the sequence of isochromatic fringe pattern

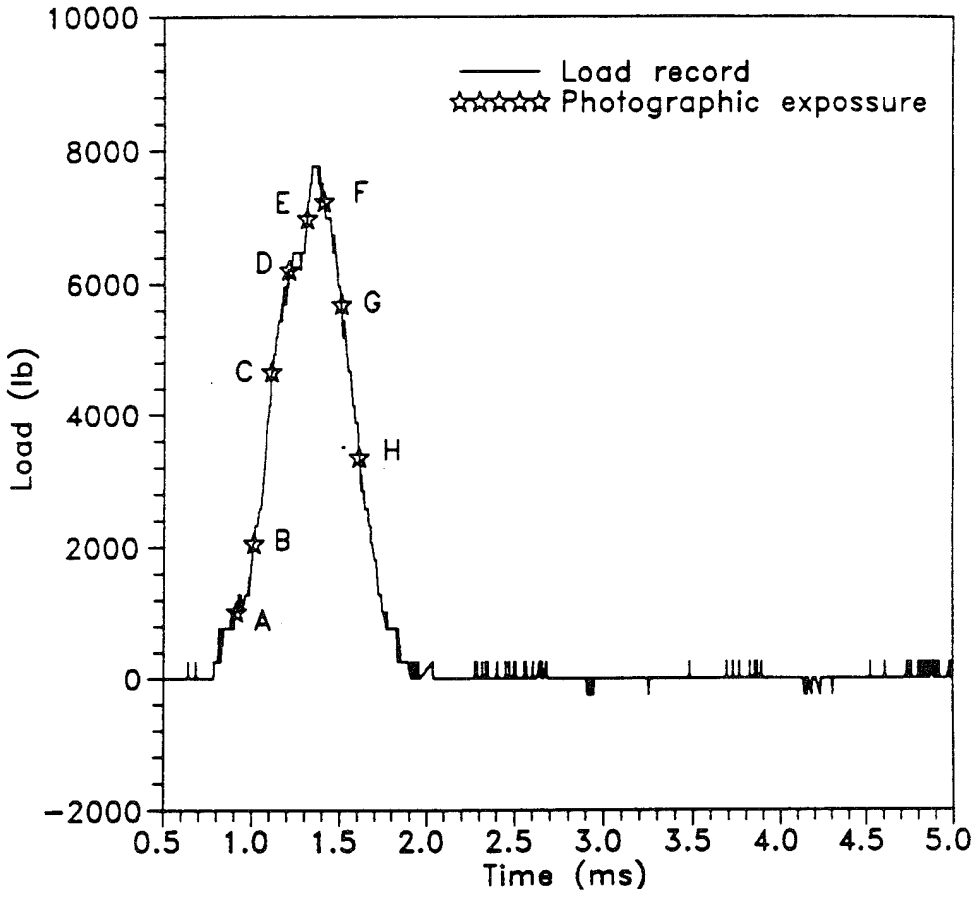

Figure 96 Load Record and Photographic Exposures. β = 54°. Impact Loading.

recordings corresponding to this specimen. The isochromatic fringe pattern at point B shows a concentration of strain around both notch tips and the first crack are detected at point C. At point D the crack has propagated to the perimeter of the specimen and final failure is accompanied by formation of secondary cracks and debonding of the photoelastic coating at point F.

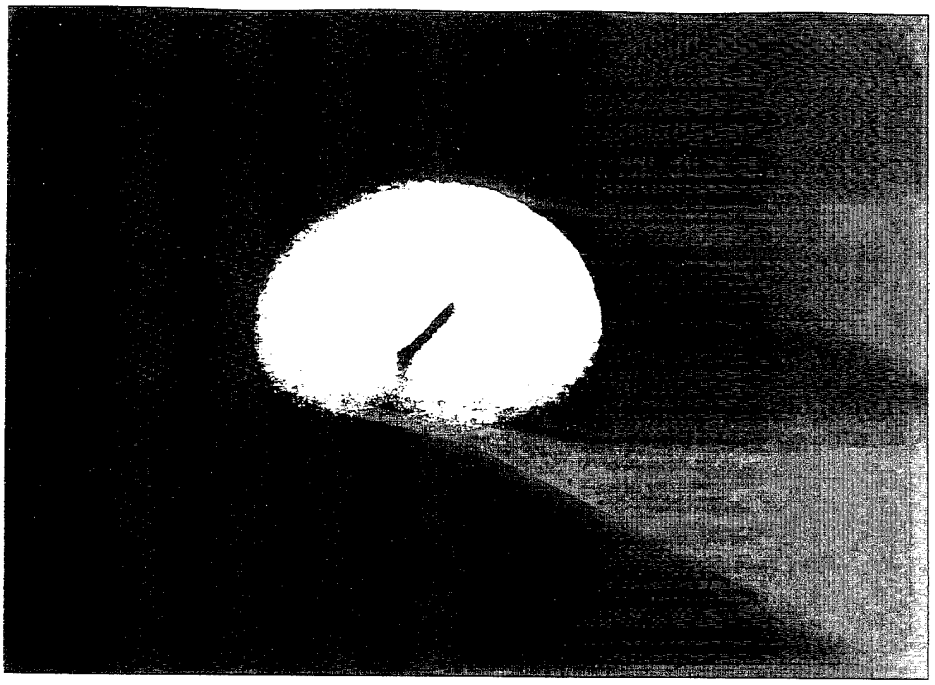

B

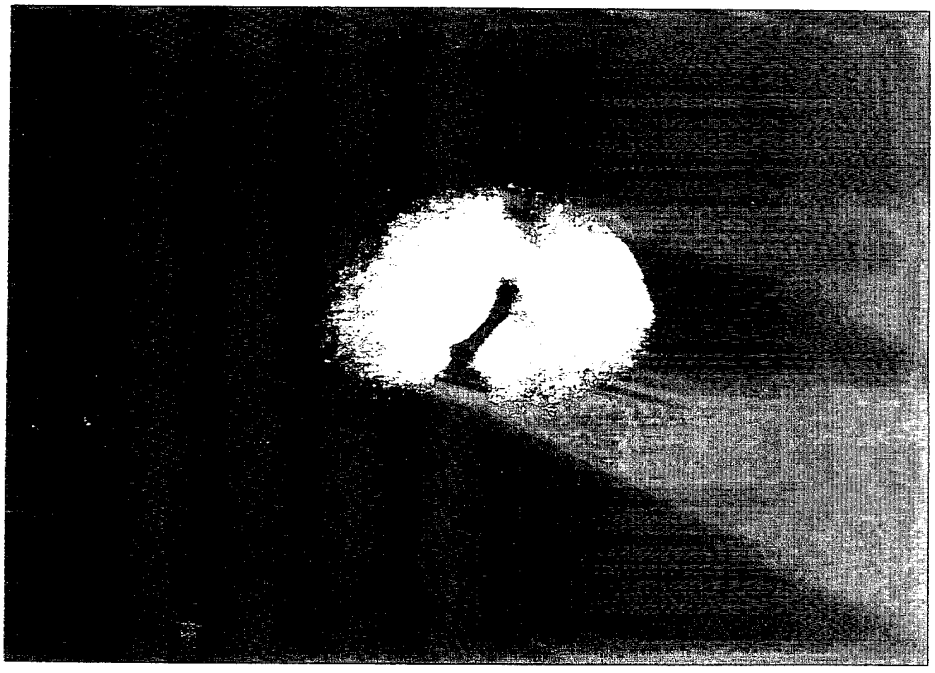

C

Figure 97 Isochromatic Fringe Patterns. β = 54°. Impact Loading. (Expossures B and C)

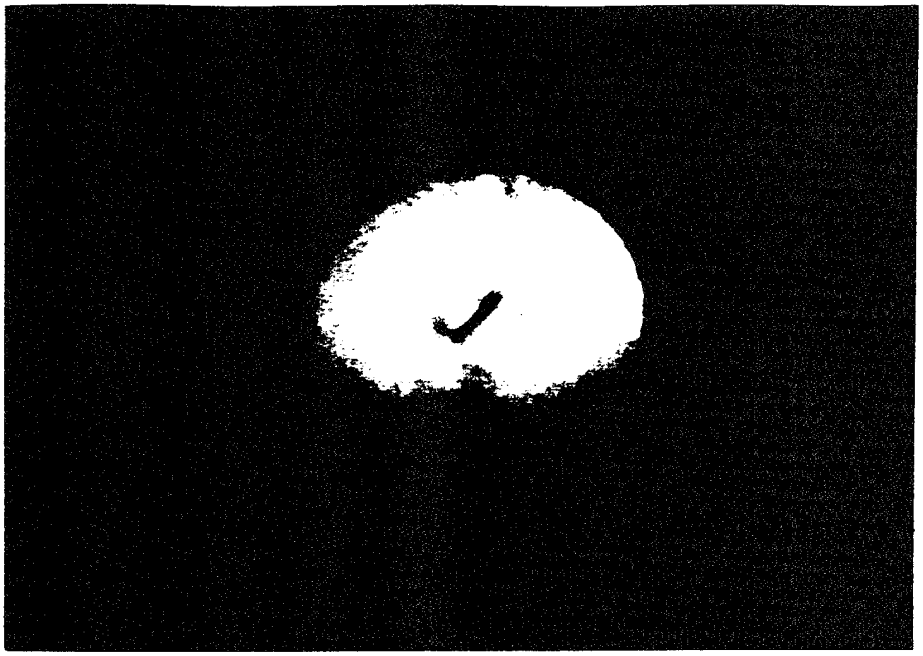

D

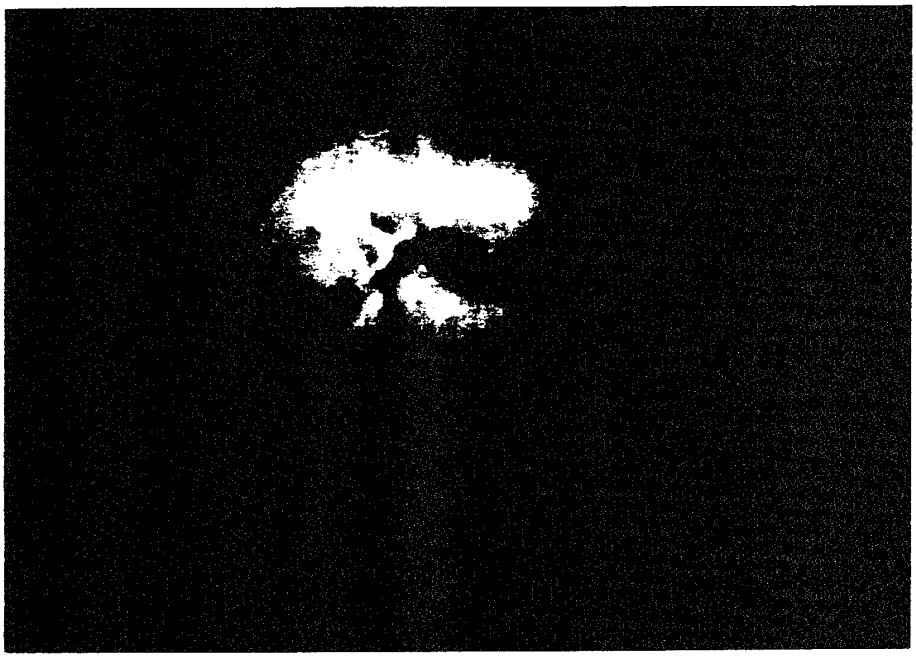

F

Figure 98 Isochromatic Fringe Patterns. β = 54°. Impact Loading. (Expossures D and F)

In general, for all the specimens studied it was found that crack initiation and growth can be correlated to the state of loading of the specimen. There is no apparent retardation of the crack growth compared to the loading sequence. Thus, it can be concluded that for the rates of loading used during this investigation failure is characterized by stable crack growth. Crack propagation velocity at this load rate appears to be more a function of the applied load than a material property.

Figure 99 shows the relative apparent stress intensity factor K_Q for different notch

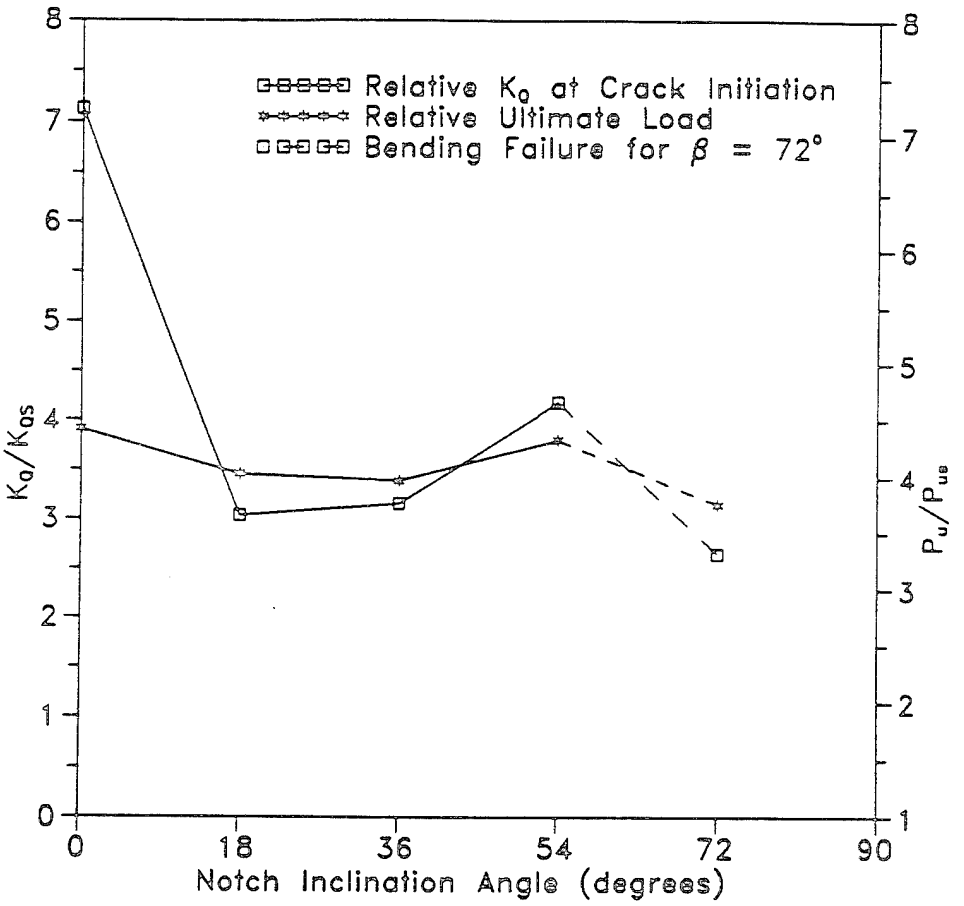

Figure 99 Relative Apparent Stress Intensity Factor ($K_Q/K_{Qstatic}$)

inclination angles. Note that the comparison should be made at crack initiation since after the crack propagates if becomes a tension crack for all notch inclinations. From this

figure it can be concluded that the increase in apparent fracture toughness for a tension crack ($\beta = 0°$) is higher than that for a shear crack ($\beta = 36°$). Also, note that between notch inclination angles $\beta = 18°$ and 36° the relative K_Q is minimum, which corresponds to the maximum shear component. In Figure 99 the values corresponding to $\beta = 72°$ should not be considered very reliable because the cracks did not start from the notch tips as expected. Also, note in Figure 100 that for the rates of loading used during this investigation the failure modes remain essentially the same. Thus, any variation in the macroscopic response should be related to change in fracture toughness.

D. CONCLUSIONS

1. Reflection photoelasticity can be used to determine crack initiation and crack growth at both quasi-static and impact rates of loading. However, the thicker, more sensitive coatings are not sensitive enough to provide information regarding the state of deformation away from the crack path.
2. The reinforcing effect of the photoelastic coating is evident in the post-peak region but it is not large enough to modify the failure mode.
3. There is good agreement between the observations made using holographic interferometry and reflection photoelasticity regarding crack initiation, crack growth and failure mechanisms at quasi-static loading.
4. At both quasi-static and impact loading, the state of cracking can be correlated to the loading stage of the specimen. For all notch inclination angles, there are three loading regions limited by crack growth, crack opening, and secondary cracking. At the rates of loading used during this investigation, failure appears to be characterized by stable crack growth.
5. The increase in fracture toughness at high rates of loading is affected by the mode of fracture. The increase of fracture toughness for tensile cracking is approximately double the corresponding to mode II cracking.

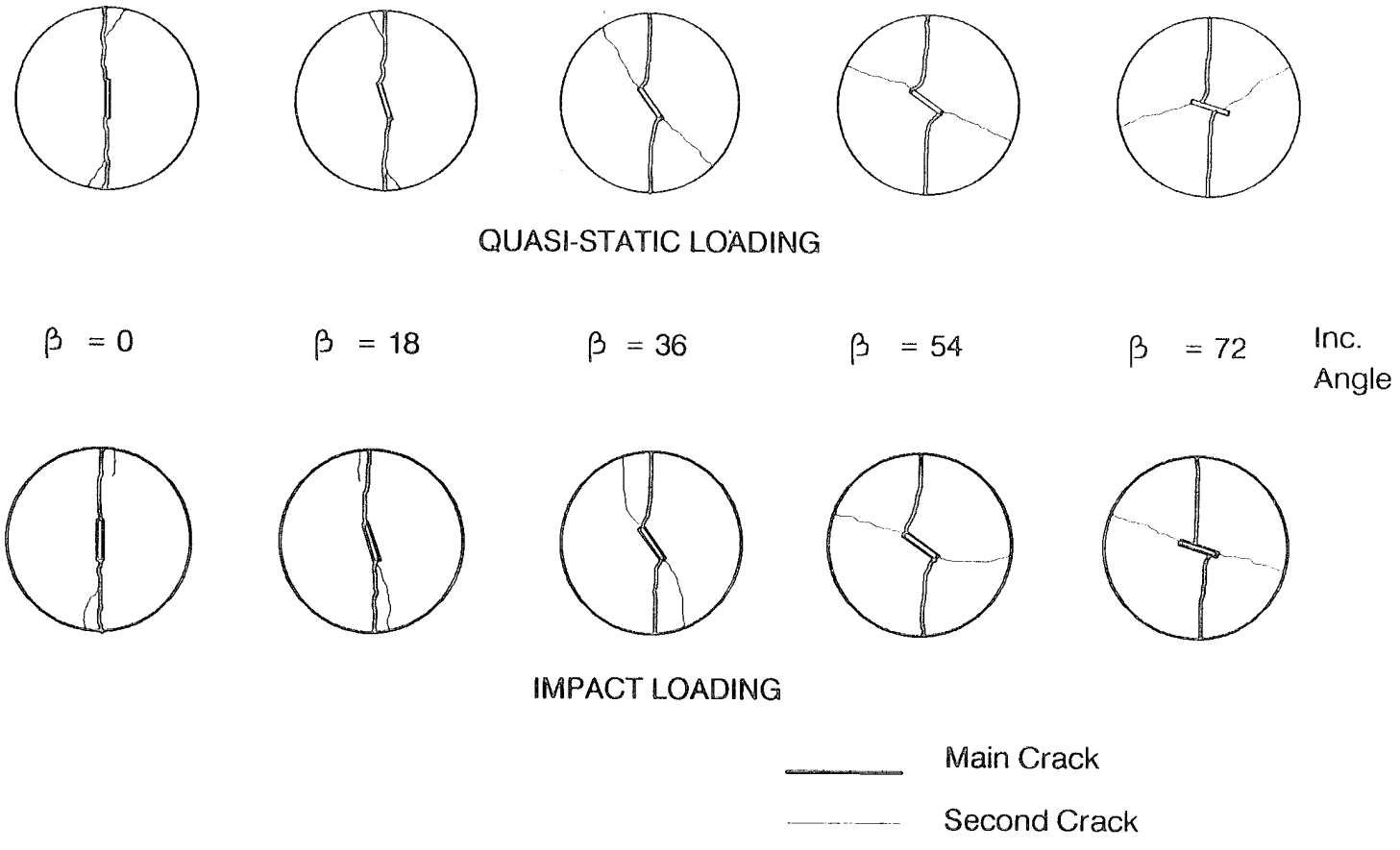

Figure 100 Failure Modes at Quasi-Static and Impact Loading.

SECTION VI

CONCLUSIONS

A. HOLOGRAPHIC INTERFEROMETRY

Sandwich hologram interferometry with multiple sensitivity vectors can be used to measure crack opening displacements and displacement fields in two and three dimensions under closed loop testing conditions. When holographic interferometry is used to measure Mode I crack opening displacements the effect of out of plane motion should be taken into account.

Digital image analysis facility provided a faster, more consistent and more accurate method of fringe count than the manual method. Image processing was essential for the elimination of rigid body motion without loss of fringe order accuracy.

B. REFLECTION PHOTOELASTICITY

Reflection photoelasticity can be used to determine crack initiation and crack growth at both quasi-static and impact rates of loading. Even the thicker, more sensitive coatings are not sensitive enough to provide information regarding the state of deformation away from the crack path. There is good agreement between the observations made using holographic interferometry and reflection photoelasticity regarding crack initiation, crack growth and failure mechanisms at quasi-static loading.

C. MODE I FRACTURE PROCESS ZONE

There is a region of high tensile strain that moves with the tip of the propagating crack. The material behind the crack tip experiences strain relaxation. However, the gradual nature of the strain relaxation demonstrates the existence of tensile force transmitted through the crack faces.

Zones of nonlinear behavior (FPZ) can be located by computing strain field deviations form the linear elastic solution. A bilinear closing pressure vs. COD cohesive crack model based on crack profile measurements has been proposed to predict both crack profiles and strain field in mode I cracking, fully characterizing the material behavior.

D. BRAZILIAN TEST

Examination of the strain distribution measured at early low stages can give indication of the crack initiation location. After crack initiation, the distribution of measured strains can give an indication of the crack growth sequence.

Although the Brazilian Test was developed and has been useful to determine the tensile strength in concrete, failure does not start in the region of uniform tensile stress. Tedesco, et al (Reference 24) made a similar observation under high rate of loading. Thus, the relationship between tensile strength and the applied load may differ from that proposed by Carneiro. From the experimental observations, it is clear that stable crack propagation has an important role in the determination of the structural response.

The reported wedge formation in the Brazilian Test configuration constitutes a secondary failure mode and occurs after a single crack has propagated through the diameter of the specimen and a significant loss of strength has taken place.

E. MIXED MODE FRACTURE PROCESS ZONE

The level of observed strains at crack initiation is considerably higher for the diametral compression disk specimen (biaxial state of stress) as compared to the compact tension specimen (uniaxial state of stress).

The size of the FPZ defined as a function of the tensile strain distribution can give an indication of the cracking mode. Both the FPZ and WFPZ are smaller for mixed mode cracking than they are for Mode I.

The mixed mode apparent stress intensity factor K_Q exhibits R-curve type of behavior.

F. RATE EFFECT

The observed mode of failure at both quasi-static and impact loading remained essentially the same which indicates that the variation in response due to change in the rate of loading depends on crack formation and growth.

For the specimen used during this investigation, after initial crack growth, the crack continued to propagate in Mode I regardless of the crack initiation mode. Collapse of the specimen was characterized by a secondary crack formation. The ultimate load for various inclination angles did not dependent on the mode of crack initiation alone. Thus, comparison of the ultimate load does not reflect mode of failure dependence. The use of high-speed photography allowed evaluation of the fracture toughness at crack initiation.

The increase in apparent fracture toughness at crack initiation for high rates of loading is affected by the mode of failure. The increase of apparent fracture toughness for tensile cracking is approximately double the corresponding value for mode II cracking.

REFERENCES

1. Mindess, S. and Shah, S.P.,Eds.,(1986) Cement Based Composites: Strain Rate Effect on Fracture, MRS Symposium Proceedings, Vol. 64.

2. John, R. and Shah, S.P., (1987) "Constitutive Modeling of Concrete under Impact Loading," Proceedings of SMIRT-9-Post Conference Seminar: Impact, Lausanne, Switzerland.

3. Chung, L. and Shah, S.P., (1987) "Strain Rate Effects on Bond Stress During Earthquake Loading," Pacific Conference on Earthquake Engineering, New Zealand National Society of Earthquake Engineering, Wairekei, New Zealand.

4. Ross, C.A., Thompson, P.Y. and Tedesco, J.W, (1988) "Split Hopkinson Pressure Bar Tests on Concrete and Mortar," Presented at the ASCE/EMD Speciality Conference, VPISU, Blacksburg, Virginia.

5. Malvern, L.E., Tang, T., Jenkins, D.A. and Gong, J.C. (1986) "In Cement Based Composites: Strain rate Effects on Fracture," S. Mindess and S.P.Shah, Ed. MRS Symposium Proceedings, Vol. 64, 119-128.

6. Reinhardt, H.W., Komerling, H.A. and Zielinski, A.J. (1986) "The Split Hopkinson Bar, A Versatile Tool for the Impact Testing of Concrete," Materials and Structures, RILEM, Vol. 19(109), 55-63.

7. Cedolin, L., Dei Poli, S., and Iori, I. (1987) "Tensile Behavior of Concrete," Journal of Engineering Mechanics, ASCE, Vol. 113(3), 431-449.

8. Du, J.J., Kobayashi, A.S., and Hawkins, N.M. (1987) "Fracture Process Zone of a Concrete Fracture Specimen," SEM/RILEM Int. Conference on Fracture of Concrete and Rock, Houston, Proceedings, edited by S.P. Shah and S.E. Swarts, 280-286.

9. Regnault, Ph., and Bruhwiler, E. (1988) "Holographic Interferometry for the Determination of Fracture Process Zone in Concrete," International Conference on Fracture and Damage of Concrete and Rock, Vienna.

10. Raiss, M.E., Dougill, J.W., and Newman, J.B. (1989) "Observation of the Development of Fracture Process zones in Concrete," Fracture of Concrete and Rock, Editors: Shah, Swartz and Barr, Elsevier Science Publishers, 243-253.

11. Miller, R.A., Shah, S.P., and Bjelkhagen, H. (1988) "Measurement of Crack Profiles in Mortar Using Laser Holographic Interferometry," Experimental Mechanics, Vol 28(4), 388-394.

12. Leith, E.N., and Upatnieks, J. (1964) "Wave Front Reconstruction with Diffused Illumination and Three Dimensional Objects," Journal of the Optical Society of America, Vol. 54, 1295-1301.

13. Abramson, N. (1981) The Making and Evaluation of Holograms, Academic Press.

14. Abramson, N. (1974) "Sandwich Hologram Interferometry: A New Dimension in Holographic Comparison," Applied Optics, Vol. 13, 1143-1147.

15. Abramson, N. (1969) "The Holodiagram: A Practical Device for Making and Evaluating Holograms," Applied Optics, Vol 8, 1235-1240.

16. Nelson, D.V. and McCrickerd, J.T. (1986) "Residual Stress Determination Through Combined use of Holographic Interferometry and Blind Hole Drilling," Experimental Mechanics, Vol. 26(4), 379-386.

17. Bazant, Z.P. and Guttu, R. (1991) "Identification of Nonlinear Fracture Properties of Size Effect Tests and Structural Analysis Based on Geometry-Dependent R-Curves," Journal of Rock Mech. and Min. Sci. & Geomech., Vol. 28(1), 43-51.

18. Miller, R. (1989) "Analysis of the Fracture Process Zone in Mortar Using Laser Holographic Interferometry," PhD. Dissertation, Northwestern University.

19. Carneiro, F.L.L and Barcellos, A. (1953) "Tensile Strength of Concrete," RILEM Bulletin No. 13, International Association of Testing and Research Laboratories for Materials and Structures, Paris, France, 97-123.

20. Wright, P.J.F. (1955) "Comments on an Indirect Tensile Test on Concrete Cylinders," Magazine of Concrete Research, Vol. 7(20), 87-96.

21. Hondors, G. (1959) "The Evaluation of Poisson Ratio and the Modulus of Materials of a Low Tensile Resistance by the Brazilian (Indirect Tensile) Test with Particular References to Concrete," Australian J. of Applied Science, Vol. 10(3), 243-268

22. Hannant, D.J., Buckley, K.J. and Croft, J. (1973) "The Effect of Aggregate Interlock Size on the Use of the Cylinder Splitting Test as a

Measure of Tensile Strength," Materials and Structures, RILEM, Vol. 6, 15-21.

23. Wawrzynek, P.A. 1987 "Interactive Finite Element Analysis of Fracture Process: An Integerated Approach," Structural Engineering Report No. 87-1 (Supervised by A. Ingrafea), Cornell University.

24. Tedesco, J.W., Ross, C.A. and Brunair, R.M. (1989) "Numerical Analysis of Dynamic Split Cylinder Tests," Computers and Structures Vol 32(3/4), 609-624.

25. Bazant, Z.P., Kazemi, M.T., Hasegawa, T., Mazars, J. and Saouridis, C. (1991) "Size Effect in Brazilian Split-Cylinder Tests: I. Measurements and Fracture Analysis," ACI Materials Journal, Vol. 88(3), 325-332.

26. Hu, X.Z. and Wittman, F.H. (1991) "An Experimental Method to Determine the Extenstion of the Fracture Process Zone," Journal of Materials in Civil Engineering, ASCE, VOL 2(1), pp 15-23.

27. Maji, A.K. and Shah, S.P. (1988) "Process Zone and Accoustic Emission Measurements in Concrete," Experimental Mechanics

28. Miller, R.A. Castro-Montero, A. and Shah, S.P., (1991) "Cohesive Crack Models for Cement Mortar Examined Using Finite-Element Analysis and Laser Holographic Measurements," Journal of the American Ceramic Society

29. Cook, R.F., Fairbanks, C.J., Lawn, B.R. and Mai, Y-W. (1987) "Crack Resistance by Interfacial Bridging: Its Role in Determining Strength Characteristics," Journal of Materials Research, Vol. 2(3), 345-356.

30. Roelfstra, P.E. and Wittman, F.H. (1986) "A numerical Method to Link Strain Softening to Failure of Concrete," Fracture Toughness and Fracture Energy of Concrete, F.H. Wittman, Ed. Elsevier Science Publishers, B.V., Amsterdam.

31. Bazant, Z.P. and Oh, B.H. (1983) "Crack Band Theory for Fracture of Concrete," Materials and Structures, Vol. 16(93), 155-177.

32. Hillerborg, A., Modeer, M. and Petersson, P.E. (1977) "Analysis of Crack Formation and Crack Growth in Concrete by Means of Fracture Mechanics and Finite Elements," Cement and Concrete Research, Vol. 6(6), 773-782.

33. Jenq. Y.S. and Shah, S.P. (1985) "A Two Parameter Fracture Model for Concrete," Journal of Engineering Mechanics, Vol. 11 (10), 1227-1241.

34. Atkinson, C., Smelser, R.E. and Sanchez, J. (1892) "Combined Mode Fracture Via the Cracked Brazilian Disk," International Journal of Fracture, Vol. 18(4), 279-291.

35. Ojdrovic, R.P. and Petroski, H.J. (1987) "Fracture Behavior of Notched Concrete Cylinder," Journal of Engineering Mechanics, Vol. 113(12), 1551-1564.

36. Jenq, Y.S. and Shah, S.P. (1988) "Mixed Mode Fracture of Concrete,"International Journal of Fracture Vol 38, 123-142.

37. Maji, A.K., Tasdemir, M.A. and Shah, S.P. (1991) "Mixed Mode Crack Propagation in Quasi-Brittle Materials," Engineering Fracture Mechanics, Vol 38(2/3), 129-145.

38. Hassanzadeh, M. Hillerborg, A. and Ping, Z. (1987) "Tests of Material Properties in Mixed Mode I and II," SEM-RILEM Int. Conf. Fracture of Concrete and Rock, Proc.

39. Bazant, Z.P. and Gambarova, P. (1984) "Crack Shear in Concrete: Crack Band Microplane Model," J. Structures Division, ASCE Vol. 110, 2015-2035.

40. Fenwick, R.C. and Pauly, T. (1968) "Mechanics of Shear Resistance of Concrete Beams," J. Structures Division, ASCE Vol. 94(ST10), 2325-2350.

41. Ramakrishnan, V., Brandshaug, I. Coyle, W.V. and Schrader, E.K., (1980) "A Comparative Evaluation of Concrete Reinforced with Straigth Steel Fibers Deformed Ends Glued Togather in Bundles," ACI Journal, Vol. 77(3), 135-143.

42. Bhargava, J. and Rehnstrom, A. (1975) "High Speed Photography for Fracture Studies of Concrete," Cement and Concrete Research Vol. 5, 239-248.

43. Gopalaratnam, V.S., Shah, S.P. and John, R. (1984) "A Modified Instrumented Charpy Test for Cement Based Composites," Journal of Experimental Mechanics, SEM Vol. 24(2), 102-111.

44. Gopalaratnam, V.S. and Shah, S.P. (1985) "Properties of Steel Fiber Reinforced Concrete Subjected to Impact Loading," ACI Journal, Vol. 83(8), 117-126.

45. Dally, J.W. and Riley, W.F. (1978) Experimental Stress Analysis, Mc. Graw Hill, Second Ed.